# NAVAL POSTGRADUATE SCHOOL

## MONTEREY, CALIFORNIA

# THESIS

**EXPERIMENTAL AND COMPUTATIONAL FLUID DYNAMIC ANALYSIS OF AXIAL-FLOW HYDRODYNAMIC POWER TURBINE**

by

Grant T. Bryan

March 2013

| | |
|---|---|
| Thesis Advisor: | Young W. Kwon |
| Co-Advisor: | Maximilian F. Platzer |

**Approved for public release; distribution is unlimited**

THIS PAGE INTENTIONALLY LEFT BLANK

| REPORT DOCUMENTATION PAGE | | *Form Approved OMB No. 0704-0188* |
|---|---|---|

Public reporting burden for this collection of information is estimated to average 1 hour per response, including the time for reviewing instruction, searching existing data sources, gathering and maintaining the data needed, and completing and reviewing the collection of information. Send comments regarding this burden estimate or any other aspect of this collection of information, including suggestions for reducing this burden, to Washington headquarters Services, Directorate for Information Operations and Reports, 1215 Jefferson Davis Highway, Suite 1204, Arlington, VA 22202-4302, and to the Office of Management and Budget, Paperwork Reduction Project (0704-0188) Washington DC 20503.

| 1. AGENCY USE ONLY *(Leave blank)* | 2. REPORT DATE<br>March 2013 | 3. REPORT TYPE AND DATES COVERED<br>Master's Thesis | |
|---|---|---|---|
| 4. TITLE AND SUBTITLE<br>EXPERIMENTAL AND COMPUTATIONAL FLUID DYNAMIC ANALYSIS OF AXIAL-FLOW HYDRODYNAMIC POWER TURBINE | | 5. FUNDING NUMBERS | |
| 6. AUTHOR(S) Grant T. Bryan | | | |
| 7. PERFORMING ORGANIZATION NAME(S) AND ADDRESS(ES)<br>Naval Postgraduate School<br>Monterey, CA 93943-5000 | | 8. PERFORMING ORGANIZATION REPORT NUMBER | |
| 9. SPONSORING /MONITORING AGENCY NAME(S) AND ADDRESS(ES)<br>N/A | | 10. SPONSORING/MONITORING AGENCY REPORT NUMBER | |

11. SUPPLEMENTARY NOTES The views expressed in this thesis are those of the author and do not reflect the official policy or position of the Department of Defense or the U.S. Government. IRB Protocol number ____N/A____.

| 12a. DISTRIBUTION / AVAILABILITY STATEMENT<br>Approved for public release; distribution is unlimited | 12b. DISTRIBUTION CODE |
|---|---|

13. ABSTRACT (maximum 200 words)

Thorough analysis of drag and power characteristics of hydrodynamic power turbines is necessary for the efficient extraction of energy available at sea. In an effort to obtain these characteristics for a three-bladed, axial-flow hydroturbine, used to provide electric power on small sailing vessels, a load cell and voltage measuring system was installed on a carriage in a towing tank for analysis across a speed range of 0.5 to 1.8 m/s. A high-speed camera was used to determine the precise carriage speed and the rotational speed of the turbine rotor. For validation of concept, two thin flat plates were analyzed using the same drag force measuring system in the tow tank to compare experimentally determined drag coefficients with known literature values.

Results are shown for the drag force experienced by the flat plates and both the non-rotating and the rotating turbine configurations. Additional results are shown for the turbine's power generation capabilities at rotational speeds between 90 and 500 RPMs. Using computational fluid dynamics for the rectangular flat plate and non-rotational turbine configuration, the experimental and computational results for the drag force characteristics were compared.

| 14. SUBJECT TERMS Hydropower Turbine, Hydrodynamic Power Generations, Experimental Towing Tank Analysis of Hydroturbine, Computational Fluid Dynamics of 3-bladed Rotor for Underwater Turbine. | 15. NUMBER OF PAGES<br>121 |
|---|---|
| | 16. PRICE CODE |

| 17. SECURITY CLASSIFICATION OF REPORT<br>Unclassified | 18. SECURITY CLASSIFICATION OF THIS PAGE<br>Unclassified | 19. SECURITY CLASSIFICATION OF ABSTRACT<br>Unclassified | 20. LIMITATION OF ABSTRACT<br>UU |
|---|---|---|---|

NSN 7540-01-280-5500

Standard Form 298 (Rev. 2-89)
Prescribed by ANSI Std. 239-18

THIS PAGE INTENTIONALLY LEFT BLANK

# EXPERIMENTAL AND COMPUTATIONAL FLUID DYNAMIC ANALYSIS OF AXIAL-FLOW HYDRODYNAMIC POWER TURBINE

Grant T. Bryan
Lieutenant, United States Navy
B.S., United States Naval Academy, 2005

Submitted in partial fulfillment of the
requirements for the degree of

**MASTER OF SCIENCE IN MECHANICAL ENGINEERING**

from the

**NAVAL POSTGRADUATE SCHOOL
March 2013**

Author:        Grant T. Bryan

Approved by:   Young W. Kwon
               Thesis Advisor

               Maximilian Platzer
               Thesis Co-Advisor

               Knox Millsaps
               Chair, Department of Mechanical and Aerospace Engineering

THIS PAGE INTENTIONALLY LEFT BLANK

# ABSTRACT

Thorough analysis of drag and power characteristics of hydrodynamic power turbines is necessary for the efficient extraction of energy available at sea.  In an effort to obtain these characteristics for a three-bladed, axial-flow hydroturbine, used to provide electric power on small sailing vessels, a load cell and voltage measuring system was installed on a carriage in a towing tank for analysis across a speed range of 0.5 to 1.8 m/s.  A high-speed camera was used to determine the precise carriage speed and the rotational speed of the turbine rotor.  For validation of concept, two thin flat plates were analyzed using the same drag force measuring system in the tow tank to compare experimentally determined drag coefficients with known literature values.

Results are shown for the drag force experienced by the flat plates and both the non-rotating and the rotating turbine configurations. Additional results are shown for the turbine's power generation capabilities at rotational speeds between 90 and 500 RPMs. Using computational fluid dynamics for the rectangular flat plate and non-rotational turbine configuration, the experimental and computational results for the drag force characteristics were compared.

THIS PAGE INTENTIONALLY LEFT BLANK

# TABLE OF CONTENTS

# LIST OF FIGURES

THIS PAGE INTENTIONALLY LEFT BLANK

# LIST OF TABLES

THIS PAGE INTENTIONALLY LEFT BLANK

# LIST OF ACRONYMS AND ABBREVIATIONS

2-D      Two Dimensional

3-D      Three Dimensional

AC      Alternating Current

AFHT      Axial-flow Hydroturbine

$C_D$      Dimensionless drag coefficient defined by: $C_D = \dfrac{F_D}{\frac{1}{2}\rho U_\infty{}^2 A}$

CFD      Computational Fluid Dynamic

$C_P$      Dimensionless power coefficient defined by: $C_P = \dfrac{P}{\frac{1}{2}\rho U_\infty{}^3 A}$

DC      Direct Current

FPS      Frames per second

N      Newton Force

NPS      Naval Postgraduate School

TSR      Tip speed ratio

Re      Reynolds Number

RPM      Revolutions per minute

WSN      Wireless Sensor Network

THIS PAGE INTENTIONALLY LEFT BLANK

# ACKNOWLEDGMENTS

THIS PAGE INTENTIONALLY LEFT BLANK

# I.    INTRODUCTION

## A.    OVERVIEW

The U.S. Navy is committed to fostering energy independence by reducing reliance on fossil fuels. The need for innovative and efficient renewable energy technologies to offset dependence on fossil fuels is key to energy independence and national security.    In the past, such initiatives have focused on identifying what renewable energy sources are available on or near government facilities to implement already existing renewable technologies in an attempt to offset the consumption of fossil fuels.  If, however, we had a way to bring additional renewable energy sources to our shores, we could add yet another layer to our energy production capabilities.

One possible way to bring off-shore wind energy to land is through the Energy Ship Concept (overview shown in Figure 1).  This concept was first described by Max F. Platzer in [1] (2009) to introduce the feasibility of transitioning to a renewable energy economy using hydrogen as the primary fuel source.   In an examination of the availability and accessibility of the various known energy sources, Platzer tried to draw attention to the fact that at the present time only a small portion of our planet's total wind energy is being exploited. The majority of the wind's energy density is located over an ocean area that covers 70 percent of the planet's surface [2].  Platzer proposed making the ocean surface wind-power accessible by the use of sailing ships equipped with hydropower generators to generate on-board electricity for the conversion of seawater into hydrogen and oxygen.  These gasses would then be compressed and delivered to a shore-based, hydrogen-oxygen power plant for re-conversion into electricity and potable water [3].
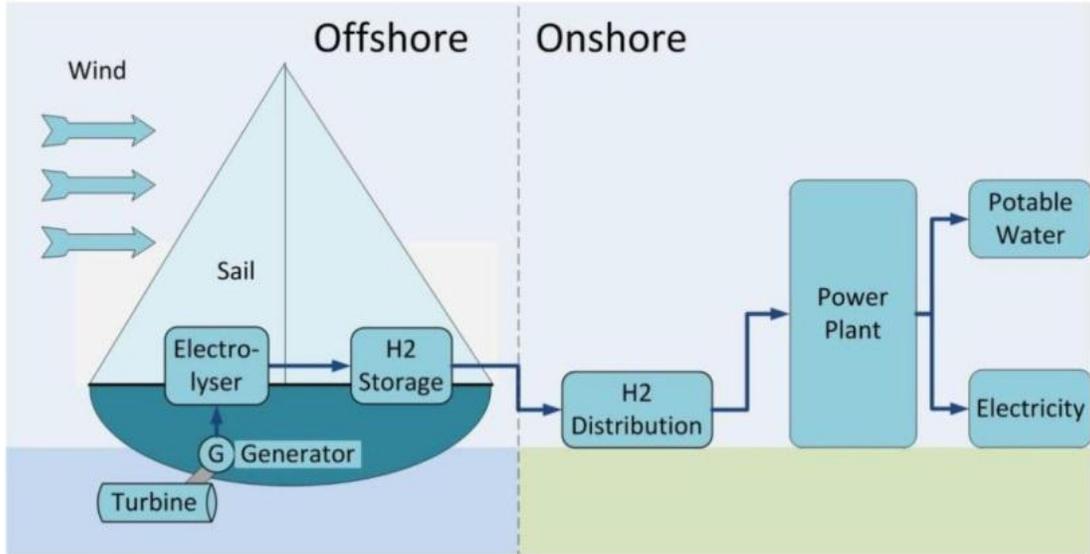
Figure 1.  Energy ship concept overview. From [4].

This paper examines a small part of the Energy Ship's power generation scheme by presenting an assessment of a commercially available axial-flow hydrodynamic power turbine.

## B.    BACKGROUND

The process of hydrokinetic energy conversion implies the extraction of the kinetic energy contained in the flow of water for the generation of electricity.  There are countless types of hydropower generators in use around the world today.  They are generally categorized into two classes: turbine and non-turbine.  For the purposes of this paper, only turbine system conversion schemes for an axial-flow hydrodynamic power turbine will be discussed.

An axial-flow (or horizontal flow) turbine refers to the directional flow of water in relation to the axis of turbine blade rotation [5].  The rotational axis of the turbine in this case is parallel to the incoming stream of water.  Considering the importance of lateral and transverse stability of sailing vessels, this type of turbine was selected due to the negligible lateral and transverse forces during operation.  With an axial-flow turbine, the primary mounting forces associated with dragging this turbine below a sailing vessel are primarily in the axial direction (direction of the sailing vessel's course through the water).

2

The need to find a highly efficient means of converting water flow into electricity is pivotal for the Energy Ship's success. If the drag translated to the ship's hull is not manageable, or the power produced not significant enough to perform the conversion of seawater into hydrogen and oxygen, then the overall concept will not work.

## C.  OBJECTIVE

The main objective of this thesis was to investigate the performance and drag characteristics of a commercially available axial-flow hydroturbine (AFHT). To do this, both experimental tests and computational fluid dynamic computations (non-rotational blade analysis only) were conducted for a fully submerged, 3-bladed rotor attached to a power generator. The results were then compared to the published values for this particular turbine's engineering specifications. Since equipment costs and open-water testing are cost-prohibitive, the objective was to determine if a tow tank, in combination with computational methods, could accurately predict performance characteristics of a hydrodynamic power generator.

## D.  SCOPE

The scope of the thesis is as follows:

- Install submersible water-driven generator with 3-bladed rotor onto the towing sled with requisite data collection devices for operation in 38 foot towing tank.

- At various speeds (measured with anemometer and high speed camera), tow two different flat plates of known dimensions through fresh water to determine strain output on towing sled (using calibrated load cell) and calculate their drag coefficients.

- At various speeds (measured with anemometer and high speed camera), tow full turbine configuration through fresh water to determine voltage output, strain on towing sled and blade's rotational speed.

- Using NextEngine's 3-D scanner with Scan Studio HD software, import 3-

D model of rotor blade into RapidWorks, then convert file to SolidWorks for CFD analysis.

- Construct similar control volume (tow tank) and generator/rotor assembly in SolidWorks and run CFX simulations in AnsysWorkbench at similar speeds to those used in the experimental phase to determine computational approximations for the non-rotational configuration of the turbine system.

- Capture and analyze the results using CFD-Post.

- Conclude with the findings and make necessary recommendations for future analysis.

## II. EXPERIMENTAL APPROACH

### A. EXPERIMENTAL FACILITY

#### 1. Towing Tank

In order to best simulate open-water trials for the AFHT at slow speeds (0-3 knots), a 38-foot towing tank was used with motor-pulley carriage system (dimensions shown in Figure 2). The AFHT was installed below the carriage using an aluminum pole and mounting clamps designed to withstand over 490 N of applied force. The carriage was pulled across the tank by a 5 horsepower, 1750 RPM motor controlled by a BALDOR motor control system with operating frequencies up to 30 Hz (equivalent to a carriage speed of about 9 m/s), though for this research 10 Hz was never exceeded (about 1.72 m/s). This configuration allowed for several seconds of steady state velocity measurements for the carriage and turbine assembly across a range of 4 to 20 feet depending on the motor speed.
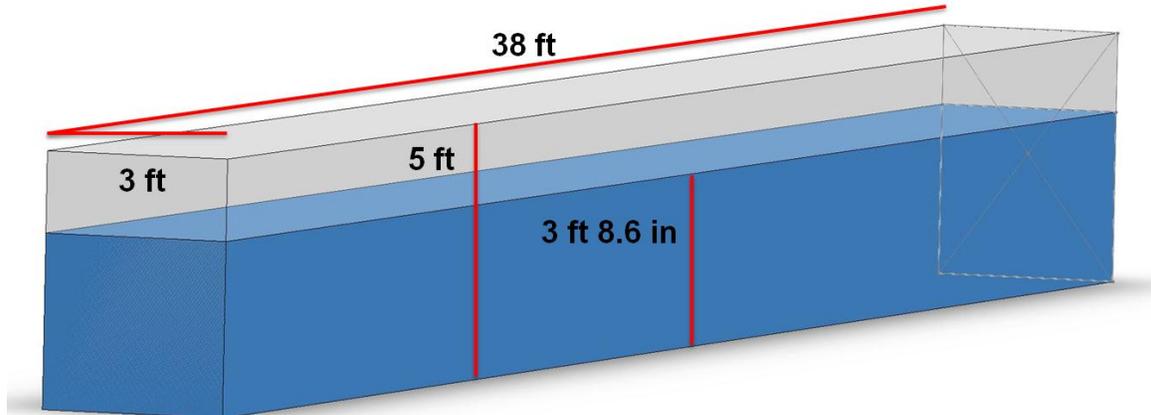


Figure 2. Tow tank dimensions for Naval Postgraduate School's Hydrodynamics Laboratory tow tank.

#### 2. Carriage Assembly

The carriage assembly consisted of four reticulating linear ball bearings installed around two circular rails along the length of the tank. The carriage was positioned on these bearings with close to equal weight distribution on each bearing allowing the

carriage to slide along the rails with minimal friction.  In order to measure the drag force experienced with nothing installed below the carriage, it was necessary to first measure the drag force experienced on the carriage alone (i.e., the drag force experienced due to the friction caused by the weight of carriage on the bearings).  Subsequent measurements would then have these measured drag forces subtracted from the total measured force to determine the actual drag force experienced due to fluid dynamics within the control volume.

### 3.    Instrumentation

An executable Labview program was written that required both National Instruments *Measurement & Automation Explorer* and the Labview 2010 *Runtime Engine* software packages. A Cole Parmer data acquisition module (18200-20 module) came with *Instacal*, a program which was used to correlate data streams on the same timeframe base from both the voltage output as well as the strain data.  With this configuration, the total software footprint was small and CPU/memory overhead was minimal. All data processes ran in the background and remained dormant until the executable file called them for graphical display within the Labview acquisition program (visual interface shown in Figure 3).  This allowed for long run-times without CPU overload.
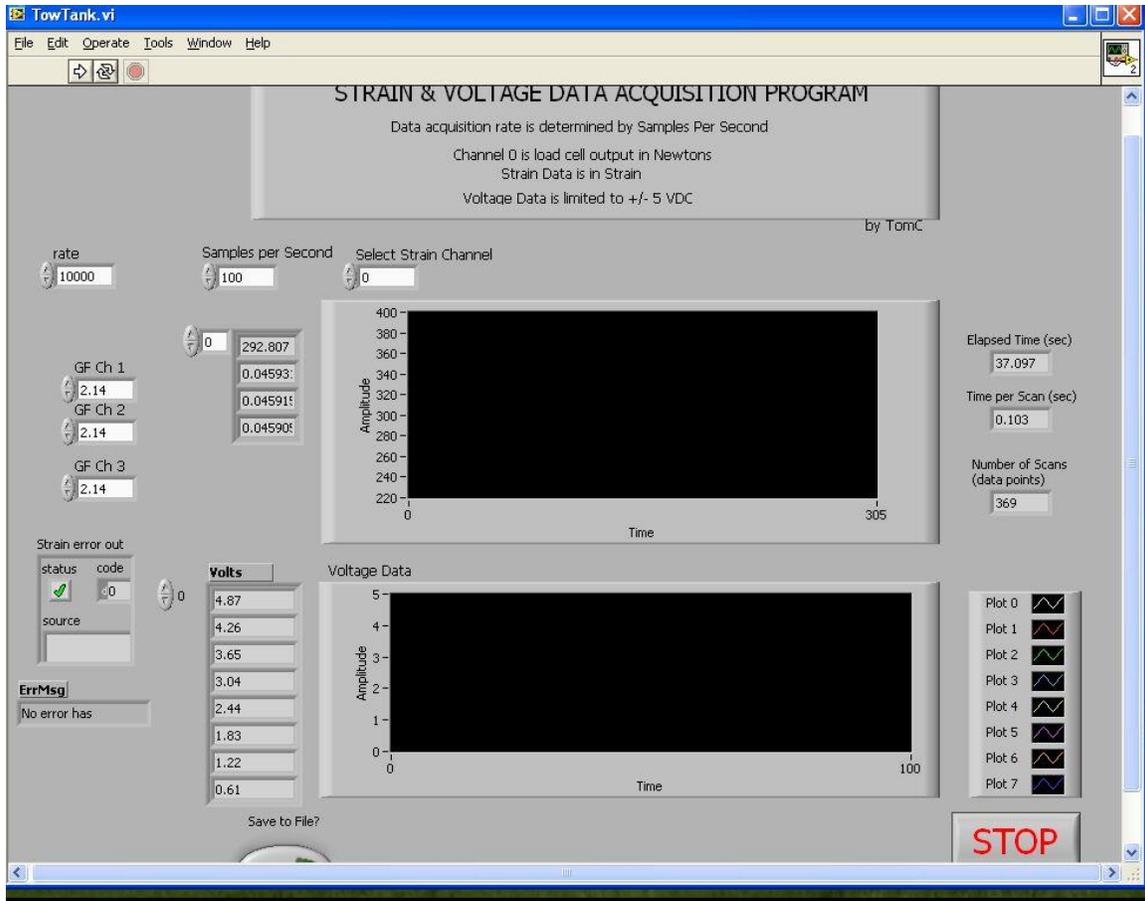
Figure 3.  Labview strain and voltage data acquisition program screenshot. From [6].

## 4.     Data Acquisition

The data acquisition setup allowed the user to select sample rate (digitizer speed), number of samples per second, gauge factors, displayable channels, and the option to save to a file or export data to reduction software (Matlab or Excel). The following data were collected for each of the full turbine runs:

### a.     Load Cell Configuration for Strain Measurement

A Honeywell Model 41 low profile "pancake" type load cell (Figure 4) was installed at the leading edge of the carriage platform and was connected to the motor's pulley system.  This particular load cell was designed for precision utilizing a double diaphragm design for added stability.

7

Figure 4. Honeywell Model 41 load cell.

The Model 41 had a capacity ranging from 0 lb. to 50 lbs. and implemented a foil strain gauge technology which had an output voltage normalized from 0 to 3.0087 mV/V which corresponded to measured loads from 0.00 lb. to 50.00 lbs. [7]. By combining the Honeywell Model 41 load cell with a National Instruments Wireless Sensor Network (WSN) device, strain data could be sent to Labview acquisition software during a run across the tank.

Four channels were scanned into a multi-element array consisting of a fixed number of samples. These samples were collected at a rate of ten data points per collected sample. The value of each data point saved was the average of the number of these ten samples in each of the array elements. The data acquisition rate was determined by the 'samples per second' setting selected prior to each run. Though this parameter varied throughout the experimental phase, a minimum of 1,000 samples per run was typically set as the minimum requirement for acceptable data. With a value of ten points per collected data sample, each run then had at least 10,000 actual data points collected.

The graphically displayed digital values include the averaged values of the data points for each channel (strain and voltage), the elapsed time for the run, and the time interval for each scan which included the total number of data points. It was determined that sample rates below 1,000 samples per second (digitizer speed) were unreliable due to the unsteady nature of the carriage's initial acceleration and deceleration during a typical run.

Within the Labview program, a strip chart graphic displayed the analog representation of a single selected channel, thus allowing us to visualize the outputted strain data in real-time during a run.

### b.    *Circuit Configuration for Voltage Measurement*
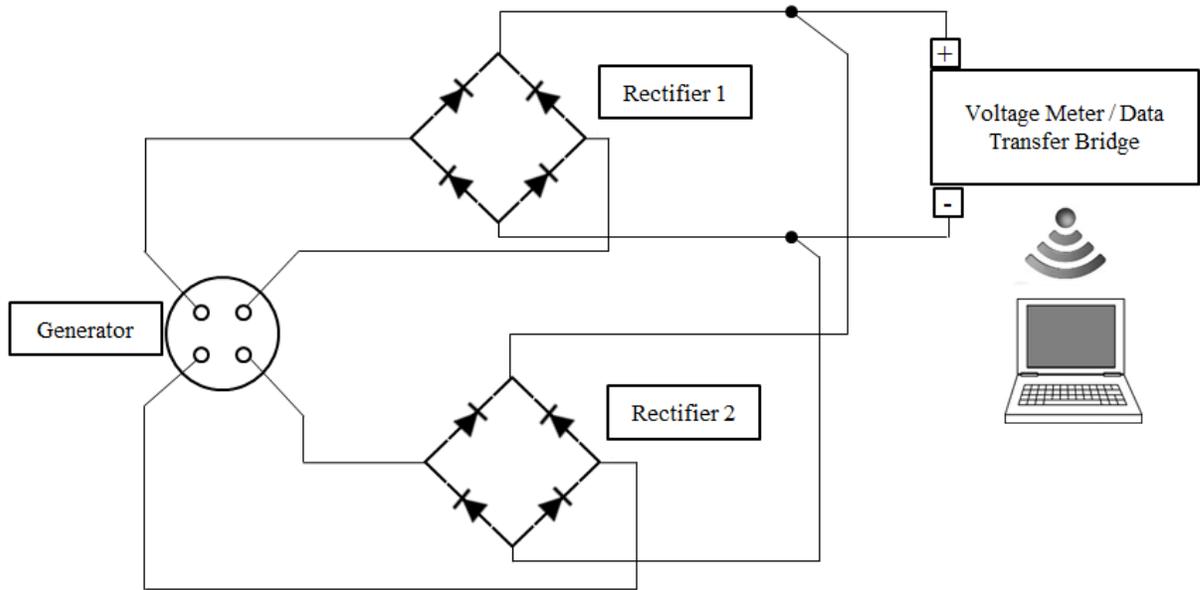


Figure 5.  Circuit diagram for generator output and data collection.

As shown in Figure 5, connected to the output of the rectifiers were the positive and negative leads connected to a voltage metering device with a data transfer module.  The voltage range was +/- 5 volts DC and the digitizer rate was fixed.  A single data point was saved for each channel and was then synchronized with the strain data and controlled by the "samples per second" setting.

### c.    *Strain Data Reduction and Analysis*

At the conclusion of each run, the data file was brought into Microsoft Excel for reduction and analysis.  Data reduction was required as only the steady state movement of the towing carriage was of interest.  The data acquisition software was programmed to collect data throughout the entirety of the carriage's movement, which include the carriage's acceleration and deceleration.  For any given run, a steady state portion could last anywhere from two to ten seconds depending on the velocity of the carriage.  Steady state was determined visually by examining the resulting graphical display of strain vs. time.

Strain measurements were converted to units of force (Newton) by applying the calibration algorithm described in the calibration certificate and also verified by experimental calibration tabulated by hanging weights of known mass at the end of the load cell pull system (up to a force of approximately 180 N). The calibration data was fit to a linear trendline shown in Figure 6.

**Load Cell Calibration Curve**
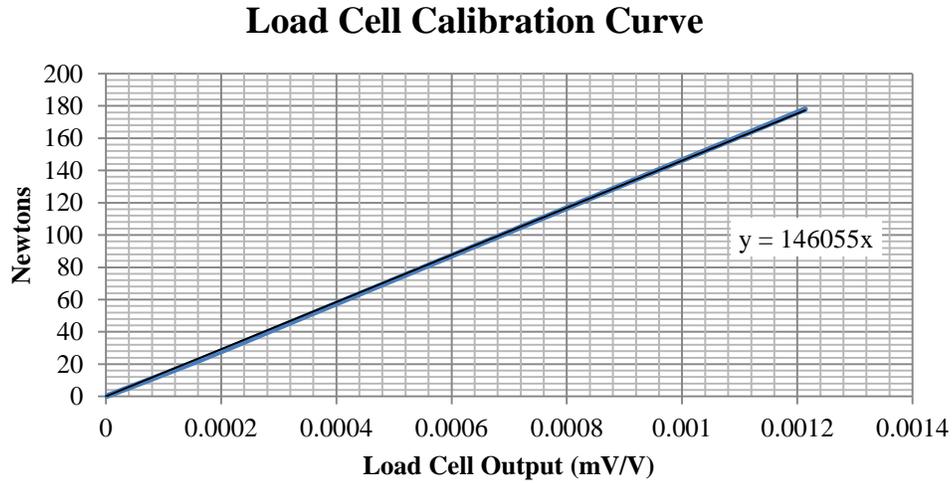


Figure 6. Load cell experimentally determined calibration curve.

The portion of the graph that was determined to be the flattest was pulled into a separate file for further analysis. An example of the reduction process is shown in Figure 7.
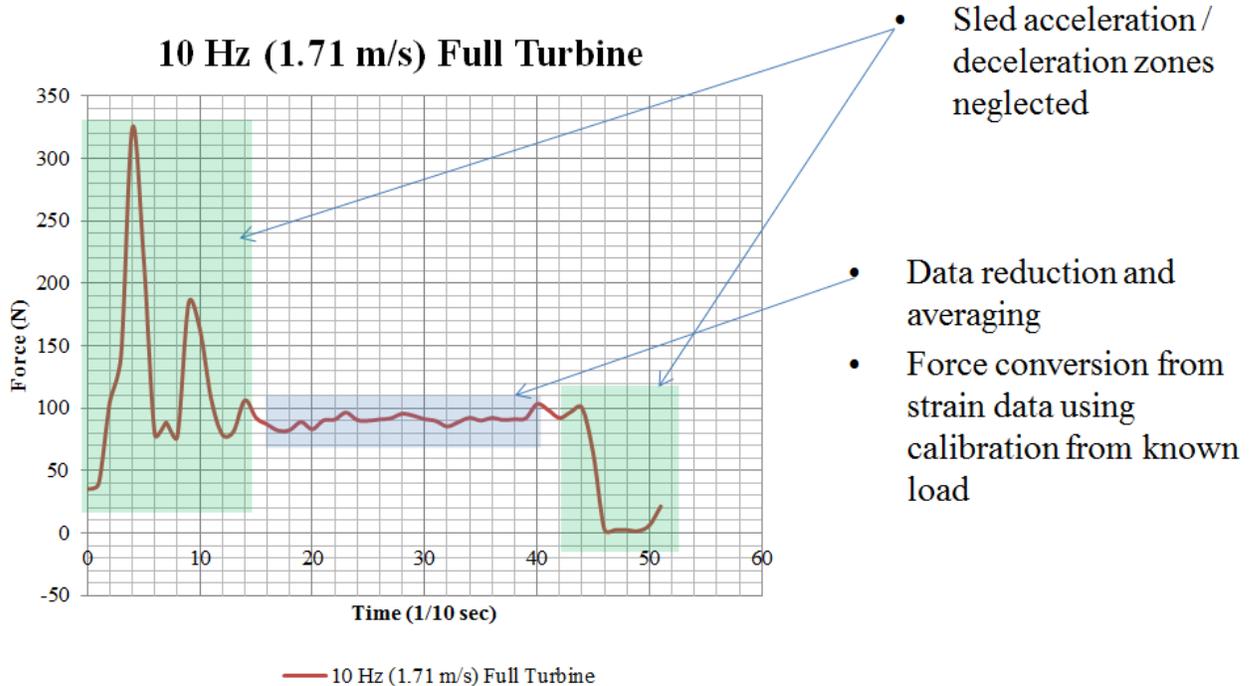
Figure 7. Strain data reduction processing.

In order to better justify the selection of the "steady state" used from these graphs, several different methods were used to determine the starting point and end point for the data to be reduced. One method involved using approximately 20% more data than that which is displayed in the figure above. This initial data included the last peak of the acceleration zone and the first peak of the deceleration zone before the force values began their decent. The variations in the location of those peaks were more significant at lower speeds, and depending on the model being analyzed in the tow tank (plates vs. rotor and turbine), the consistency of data tabulated for the subsequent steady state forces varied +/- 6 N, or approximately 10% across the full range of carriage speeds. For this reason, we chose data within the bounds of these acceleration and deceleration peaks visually. There are obvious errors associated with visually determining the start and stop points of any data being collected, however, the total difference in measured force between the two methods of reduction was less than 3% and the visual determination of steady state ultimately provided for more agreeable and consistent data as the number of trials increased for each model.

11

### d.        *Anemometer*

An anemometer was installed on the carriage to determine the model's speed through the water.  The MiniWater6 Mini probe with the SQ2010 portable data logger was configured to acquire a measurement of water flow in the Tow Tank with advertised 0.02 - 5 m/s range and a limited sampling rate of 10 Hz [8].  It was difficult to get precise water velocities to correlate exactly with the strain and voltage data acquired on the same time scale as the MiniWater6 was not compatible with the data acquisition module described above.   Additionally, though the velocity measurements were consistent, they did not correlate with a visual measuring technique utilizing a high-speed camera as described below.

### e.        **High-Speed Camera**

A high-speed camera was utilized to capture the RPM count of the turbine's rotor (if rotating), as well as the carriage velocity as a means to check the accuracy of the water probe anemometer.  An Olympus i-SPEED 3 high-speed video camera was set up to provide high resolution, extreme low-light sensitive recording at 1000 frames per second.  At approximately 1.83 meters from the side of the towing tank's center viewing glass, the camera could record the precise time (to within 0.01 milliseconds) required for the model to travel a distance of 0.992 meters through the water.  Due to the camera's optical angle in relation to the tow tank's center viewing glass, an optical correction was applied to the values recorded in the video to arrive at a distance of 0.992 meters.  With a camera frame rate set to either 500 fps or 1,000 fps, it was possible to mark the beginning and end frames for a specific carriage position. These positions were used to determine the total elapsed time required for the carriage to travel 0.992 meters, allowing for a precise velocity to be calculated within the uncertainty range of 0.0001 m/s (+/- 0.00005 m/s) [9].

### f.        *Anemometer vs. High-Speed Camera*

Upon completion of a carriage run, both velocity values were compared. The anemometer data and the high-speed camera velocity calculations were consistent in

and of themselves, however, their outputted values were different by a factor of almost 0.1 (approximately .099 m/s) across a speed range of 0.4 to 1.8 m/s. A comparison of the results is shown below.

**Comparison Between Anemometer and High-Speed Camera Velocity Measurements**
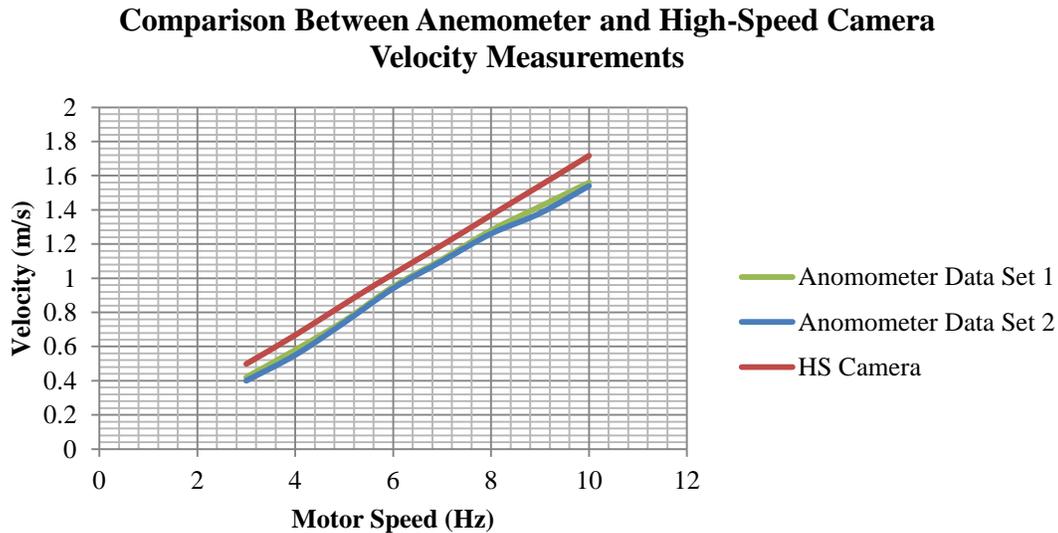


Figure 8. Graphical representation of velocity measurement comparison.

Since the velocity measurements differed consistently across the given speed range, one possible explanation is that the calibration of the anemometer's voltage metering used in the MiniWater 6 Probe's data measuring software is off merely by a factor of 10 %, or 20 mV, which is within the reported range of accuracy provided by the manufacturer. Additionally, the anemometer used was designed for a speed range of 0.5 - 20 m/s, which means that at a motor speed of 3 Hz, our data lied at the lower end of this device's measuring range.

As the force and drag coefficient calculations are highly dependent on accurate velocity inputs (force proportional to velocity squared), it was determined that the high-speed camera method would be the primary source for acquiring velocity data for each run.

Prior to each run, a motor speed was inputted into the control unit with values from 3.0 to 10.0 Hz. Each of these inputted values were correlated with the

13

expected speeds plotted in Figure 8). Depending on what was being pulled through the tow tank, a 3 Hz command resulted in tank velocities from 0.48 m/s to 0.55 m/s. There was also some variability when the carriage configuration did not change (approx. 1.7 % deviation recorded for trials with no change in configuration).

**B.    MODELS**

As discussed previously, in order to determine the resultant drag force experienced by a particular model attached to the towing carriage, several tests were required with the carriage alone traveling across the tow tank. These tests were correlated with the associated carriage velocities (represented by motor speeds in Hz) and strain values acquired were subtracted from the values measured for the models placed in the tow tank.

A graph of the measured data for the sled alone configuration is shown in Figure 9.
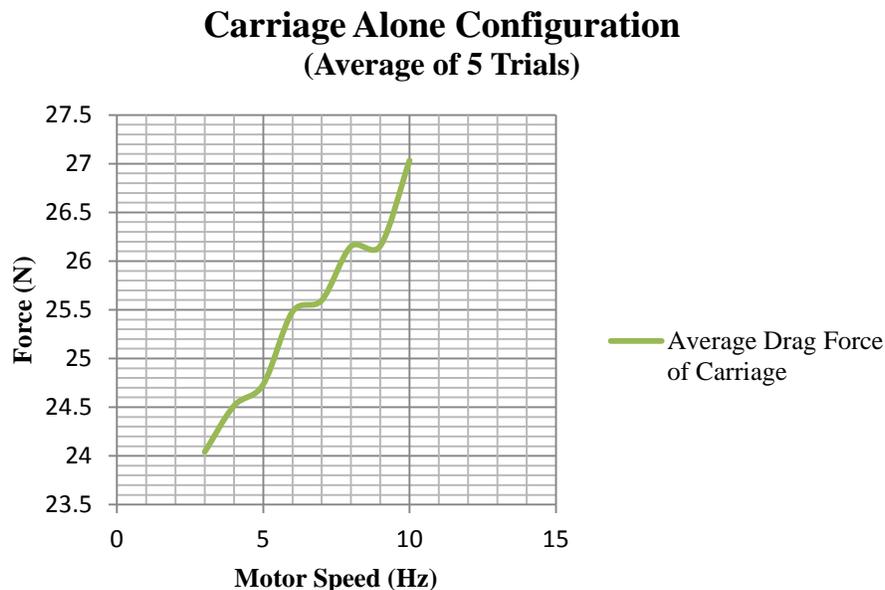


Figure 9. Drag force due to friction caused by weight of carriage alone.

### 1. Flat Plate Models

In order to validate the methodology used in determining the experimental drag forces, it was determined that additional experiments should be completed on objects with known fluid flow properties. Flat plates have been analyzed in fluid flow schemes for centuries in order to evaluate the flow properties of a fluid on simple structures. Professor Frank M. White wrote several textbooks on fluid mechanics and heat transfer which are often used as primary source documents for various models' drag coefficients [10].

#### a. Drag Coefficient for Thin Flat Plates

The drag coefficient is a dimensionless quantity that is used to quantify the drag or resistance of an object in a fluid environment such as air or water. It is used in the drag equation (Eqn. 1), where a lower drag coefficient indicates the object will have less aerodynamic or hydrodynamic drag. The drag coefficient is always associated with a particular surface area [7].

$$F_D = \frac{1}{2}\rho U_\infty^2 A C_D$$

(1)

For a thin flat plate, the recognized drag coefficient, $C_D$, is 1.18 for a rectangular plate (aspect ratio of approx. 2), and 1.17 for a disk according to [11], table 7.3 . In order to calculate this value from experimentally acquired data, several variables are required from the data sets. First, an accurate value for the fluid velocity approaching the model, $U_\infty$, is required (or the stream velocity of the fluid in the case of a stationary object). Second, the density of the fluid, $\rho$, within the control volume is required. Third, a model's reference area, or projected area, $A$, is required. This may not be the same as the model's surface area (e.g. the projected area for a sphere is simply the area of a circle: $A = \pi r^2$, rather than the surface area of a sphere: $A = 4\pi r^2$). In the case of a rotating turbine blade, we will use the swept area.

The drag coefficients were calculated by conducting tow tank experiments for the following plates (shown in Figure 10):

15

Plate A (Rectangular):

- Dimensions: 173 mm x 78 mm x 5mm

- Projected Area: 0.05822 m$^2$

- Sting dimensions:  25 mm x 110 mm (0.00275 m$^2$)

Plate B (circular disk):

- Dimensions: radius = 114 mm, thickness: 5 mm

- Projected Area: 0.040828 m$^2$

- Sting dimensions: 25 mm x 110 mm (0.00275 m$^2$)
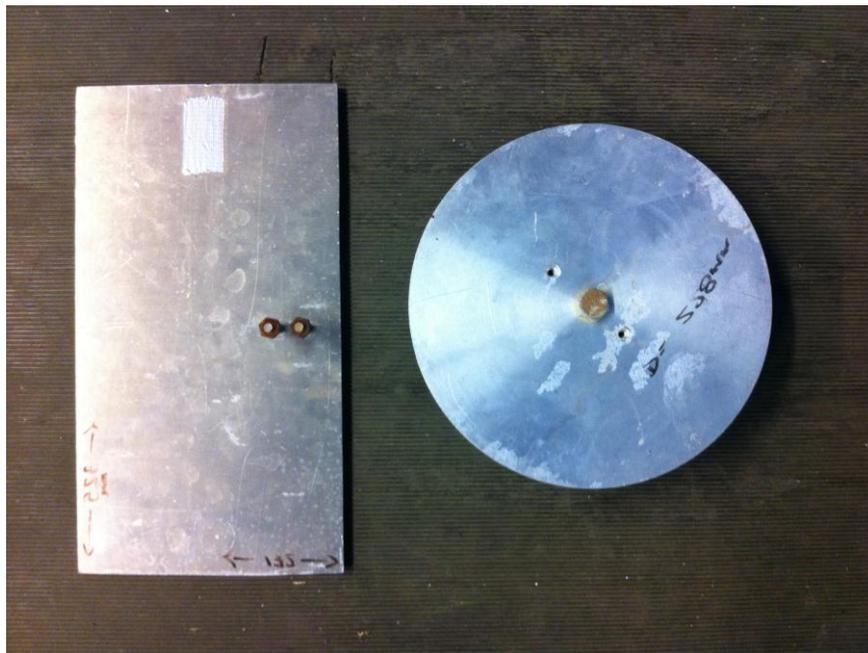


Figure 10.    Plate A (rectangular) and Plate B (circular disk).

The photo in Figure 11 was taken during a 0.86 m/s tow tank run with Plate A installed below the carriage (the small red probe located in front of the plate is the installed anemometer).
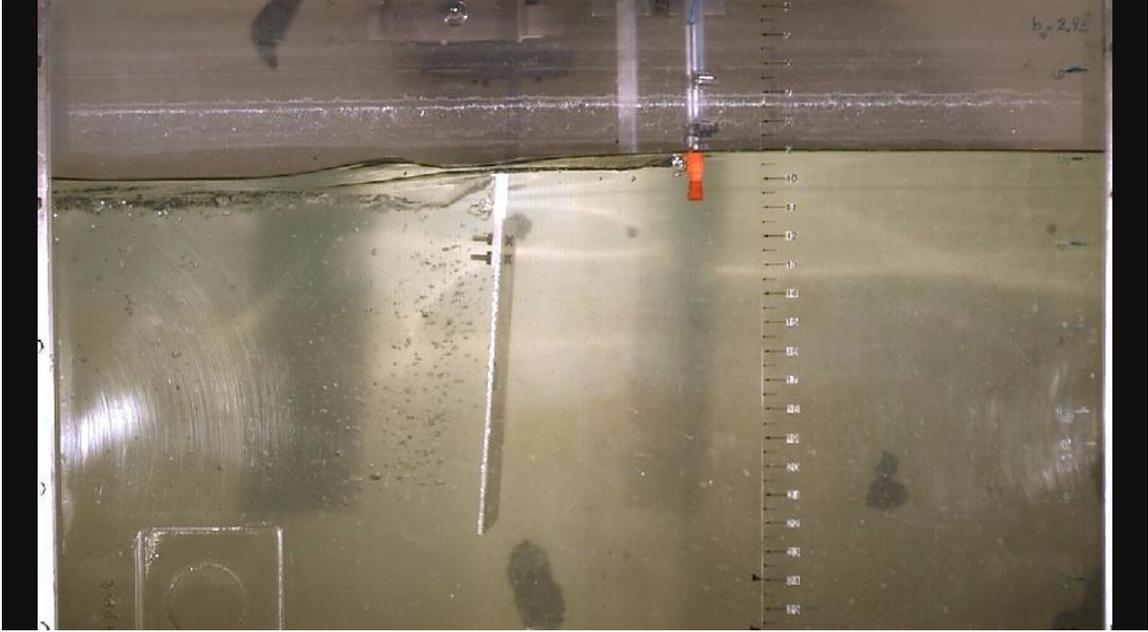
Figure 11.    Plate A traveling through tow tank at 0.86 m/s.

### b.    *Flat Plate Raw Data*

Three trials were conducted for each plate in the tow tank.  A single trial consisted of eight carriage runs from 0.5 m/s to 1.8 m/s.  During each run, the velocity was measured by the high-speed camera, and the resultant drag force was measured using the load cell attached onto the front of the carriage.  Subtracted from that data was the carriage alone values, which allowed for a more accurate look at just the forces experienced by the plate traveling through the water.

Table 1.    Drag force data for flat plate trials.

| 3-Trial Average – Plate A | | 3-Trial Average – Plate B | |
|---|---|---|---|
| $U_\infty$ (m/s) | Drag Force* (N) | $U_\infty$ (m/s) | Drag Force* (N) |
| 0.496 | 3.90 | 0.504 | 4.46 |
| 0.676 | 11.55 | 0.687 | 9.66 |
| 0.848 | 23.51 | 0.861 | 16.85 |
| 1.012 | 39.71 | 1.035 | 27.01 |
| 1.178 | 57.72 | 1.204 | 37.13 |
| 1.337 | 75.61 | 1.370 | 50.82 |
| 1.494 | 98.67 | 1.545 | 60.36 |
| 1.632 | 115.04 | 1.716 | 68.23 |
| * Total drag for model minus carriage drag | | | |
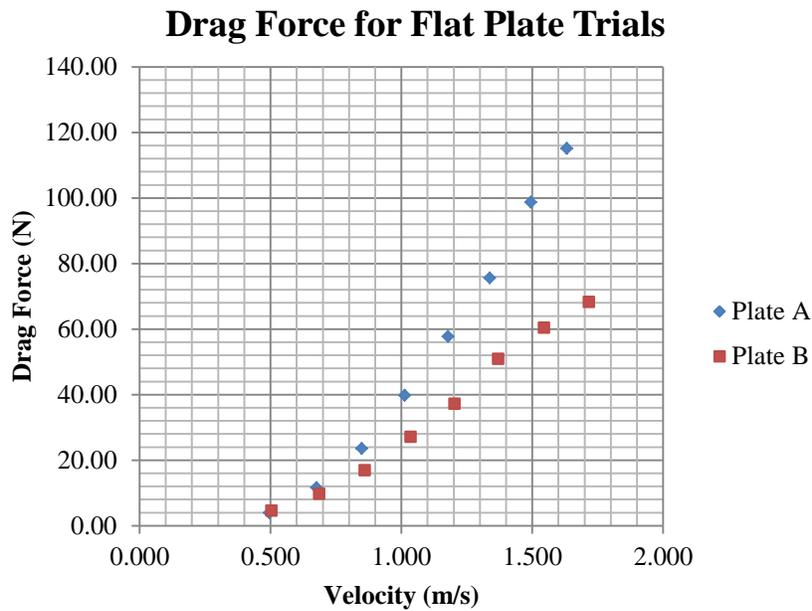


Figure 12.    Average drag force data for plates A & B, 3 trials each.

Using Eqn. (1) and velocity and drag force measurements listed in Table 1, the drag coefficient, $C_D$, for each plate was calculated. The average values for the drag coefficient across all the trials are listed in Table 2.

Table 2.    Drag coefficients from raw data and literature values. From [11].

| Model | C_D | |
| --- | --- | --- |
| | Exp. Average | Literature Value |
| Plate A | 1.24 | 1.18 |
| Plate B | 1.27 | 1.17 |

These values represent the raw, uncorrected values for the experimental data collected for the flat plate trials. Considering the published values listed in Table 2, our data would seem to indicate an error of about 6% higher than those referenced values.

### 2.    Axial-Flow Hydroturbine (AFHT) Model

The AFHT selected for this analysis was a submersible UW 100 water-driven generator, capable of supplying up to 100 watts of 12-volt electrical power for battery charging. This design was introduced into service in 1988 as a variant of a hybrid wind power generator developed by AmpAir Energy Ltd out of the United Kingdom. The two-phase alternator incorporates two stator windings and two permanent magnet rotors on a common shaft. The rotors are staggered at 30 degrees to each other to minimize starting torque due to magnetic "cogging". The alternator produces alternating current (AC), which has to be rectified to direct current (DC) externally which requires two bridge rectifiers, one for each phase, with the rectifier outputs in parallel [12].

The *full turbine configuration* referenced in this paper refers to the 3-bladed rotor connected to the generator casing as shown in Figure 13. The full turbine was installed to the tow carriage using a 4.8 cm diameter aluminum pole, referred to as a sting, with a depth of approximately 20 cm, placing the rotational axis of the turbine at approximately 27.5 cm below the tank's water line. By removing the rotor from the full turbine configuration, we were able to analyze the drag characteristics the generator alone. Although it is unlikely that the drag force values acquired in this *generator alone configuration* could be added directly to a *rotor alone configuration* to come up with

19

accurate values for a *full turbine configuration*, the generator alone configuration was analyzed to further validate our data acquisition scheme and drag coefficient calculations for various models in the tank.
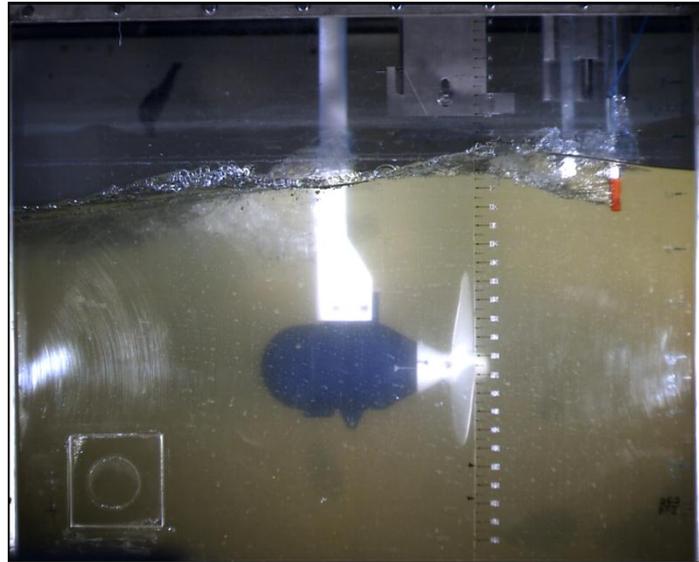


Figure 13.    Photo of full turbine configuration traveling through tow tank at 1.72 m/s.

### a.        *Generator Alone*

The generator body casting is made of powder coated aluminum and weighed approximately 20 lbs.  A hemispherical casting was installed behind the generator to provide some degree of hydrodynamic protection from cavitation and fluid separation.  The alternator's shaft exits the casing at the front of the generator.  The resulting shape is very similar to a bullet or submarine (Figure 14).

Figure 14.    Photo of generator and sting.

Like all other models, the generator was towed through the tank at speeds from 0.5 m/s to 1.8 m/s.  For each speed, the values for drag force and carriage velocity were tabulated (Table 3).  Drag force plotted as a function of velocity and the calculated drag coefficients at those speeds are shown in Figures 15 and 16 respectively.

(1)     Generator Alone Raw Data

Table 3.     Raw data for generator alone configuration.

| Generator Alone | | |
|---|---|---|
| $U_\infty$ (m/s) | Drag Force*(N) | $C_D$ |
| 0.496 | 3.9 | 1.716 |
| 0.676 | 11.55 | 0.979 |
| 0.848 | 23.51 | 0.965 |
| 1.012 | 39.71 | 0.764 |
| 1.178 | 57.72 | 0.765 |
| 1.337 | 75.61 | 0.600 |
| 1.494 | 98.67 | 0.593 |
| 1.632 | 115.04 | 0.578 |
| * Total drag for model minus carriage drag | | |

## Drag Force vs Velocity
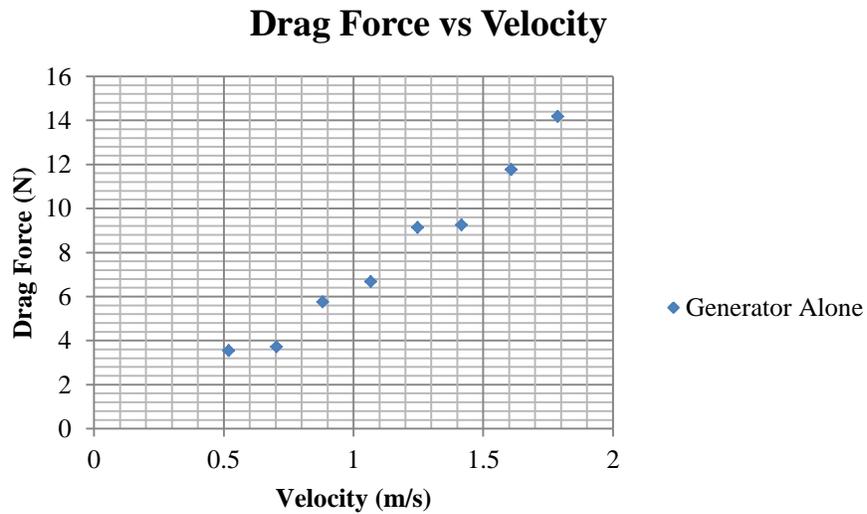


Figure 15.     Drag force and velocity measurements for generator alone configuration.

**Drag Coefficient vs Velocity**
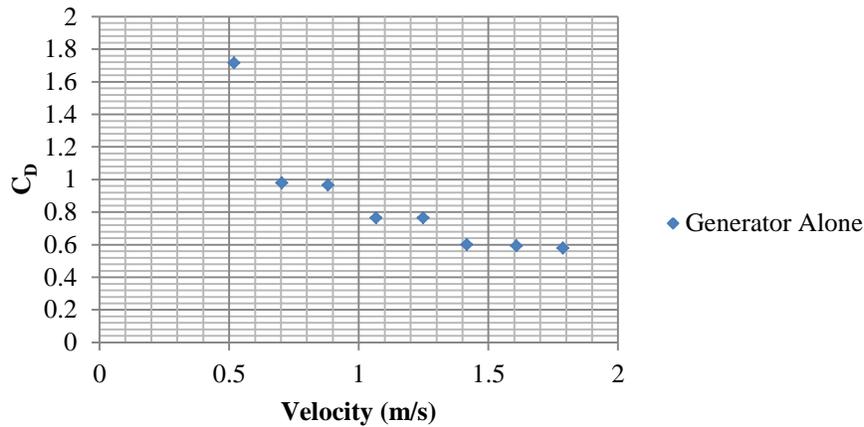


Figure 16.    Calculated drag coefficients for generator alone configuration.

### b.    *Non-Rotational Rotor*

To better estimate the characteristics of the turbine, we examined both the rotational and non-rotational configurations of the rotor provided with the turbine. The rotor, referred to as a propeller in the technical manual, is a three-bladed, aluminum cast, 312 mm diameter, $43^{\circ}$ raked, fixed pitch (5.8 inch average pitch) rotor [13]. The projected area of the rotor is approximately 0.03645 m$^2$. This area was used in calculating the drag coefficient for the non-rotational trials rather than the swept area, which is primarily used for rotational rotors. A photo of the rotor is shown in Figure 17.
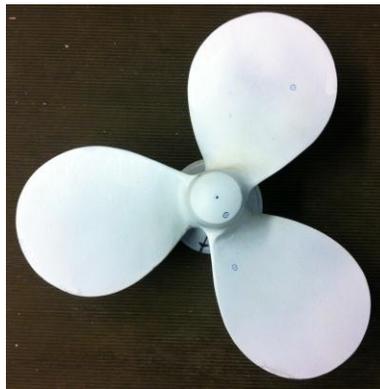


Figure 17.    Photo of 3-bladed AFHT rotor.

Since we would ultimately compare the experimental data collected during these non-rotational trials, we performed several runs in an attempt to improve the precision of our data. The turbine was towed through the tank at speeds from 0.5 m/s to 1.8 m/s. For each speed, the values for drag force and carriage velocity were tabulated in Table 4 with drag force and the calculated drag coefficients graphed as a function of velocity shown in Figures 18 and 19 respectively.

(1)     Non-Rotational Rotor Raw Data

Table 4.     Raw data for non-rotational turbine configuration.

| Non-rotational, Full Turbine Data (3 trial averaged) | | |
|---|---|---|
| Velocity (m/s) | Drag Force*(N) | $C_D$ |
| 0.508 | 4.322 | 0.920 |
| 0.693 | 8.546 | 0.979 |
| 0.869 | 14.596 | 1.064 |
| 1.042 | 22.530 | 1.141 |
| 1.210 | 32.825 | 1.233 |
| 1.372 | 42.846 | 1.251 |
| 1.550 | 53.680 | 1.228 |
| 1.716 | 63.590 | 1.187 |
| * Total drag for model minus carriage drag | | |

**Drag Force vs Velocity**
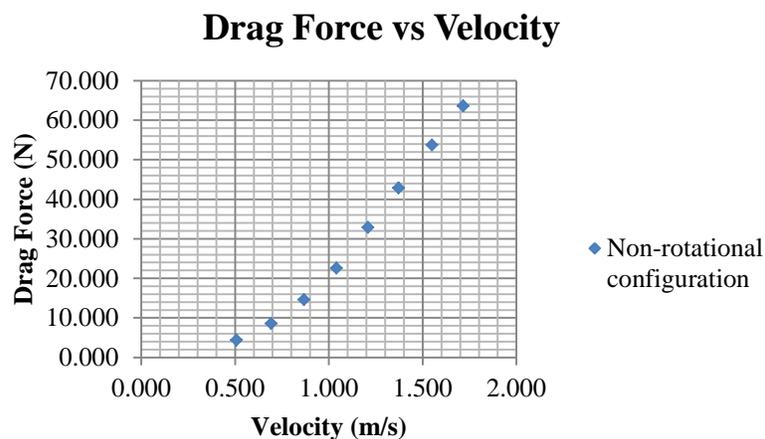


Figure 18.     Drag force at various speeds for non-rotational full turbine configuration.

**Drag Coefficient vs Velocity**
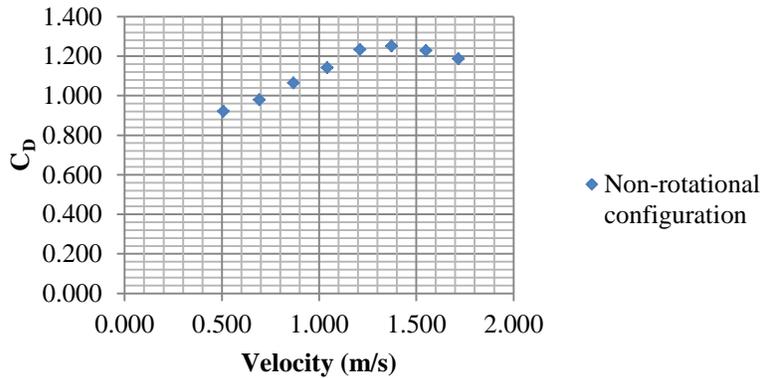


Figure 19.    Drag coefficients at various speeds for non-rotational full turbine configuration.

### c.    *Rotational Rotor*

With the rotor now free to spin, the full turbine configured model was analyzed under the same tank conditions as before.  For these trials, it was important to connect the generator outputs to the data acquisition bridge with known resistances for the safety of the alternator and internal electrical components of the generator.  In addition to connecting the generator outputs into circuit, the high speed camera also needed to be used for both velocity measurements and the rotational speed of the turbine. To do this, the rotor was marked with a line that matched up with another line on the generator casing.  When these two marks were in alignment, a counter was started that was used to keep track of the number of revolutions per second.  From this data acquisition scheme, we were able to determine the rotations per minute (RPM) of the rotor, the speed of the carriage (and subsequent speed through the water), voltage output and drag force for each run.  Using the recorded voltage outputs and the known resistances added to the circuit, it was then possible to calculate the turbine's power output over a range of resistances, velocities and rotational speeds.

The generator already had a certain observed resistance due to the magnetic cogging associated with the two stator windings and two permanent magnetic rotors inside the alternator.  Though this resistance was not known to us, we made the

assumption that once rotation began, the torque due to cogging was negligible and all subsequent resistance experienced by the rotor during rotation was due to the production of current.

The output voltage was then either reduced or increased by adding or removing resistors into the output circuit of the turbine. By placing 10 ohm resistors in either series or parallel configurations, we introduced the following circuit resistances: 5, 10, 20, 30 and 40 ohms. For each of these resistances, or applied turbine loads, we were able to determine the effects of the loading on the rotational speed of the rotor at various velocities through the tank. The photo in Figure 20 shows a 20 ohm resistive load applied to the output of the turbine before a run through the tow tank.
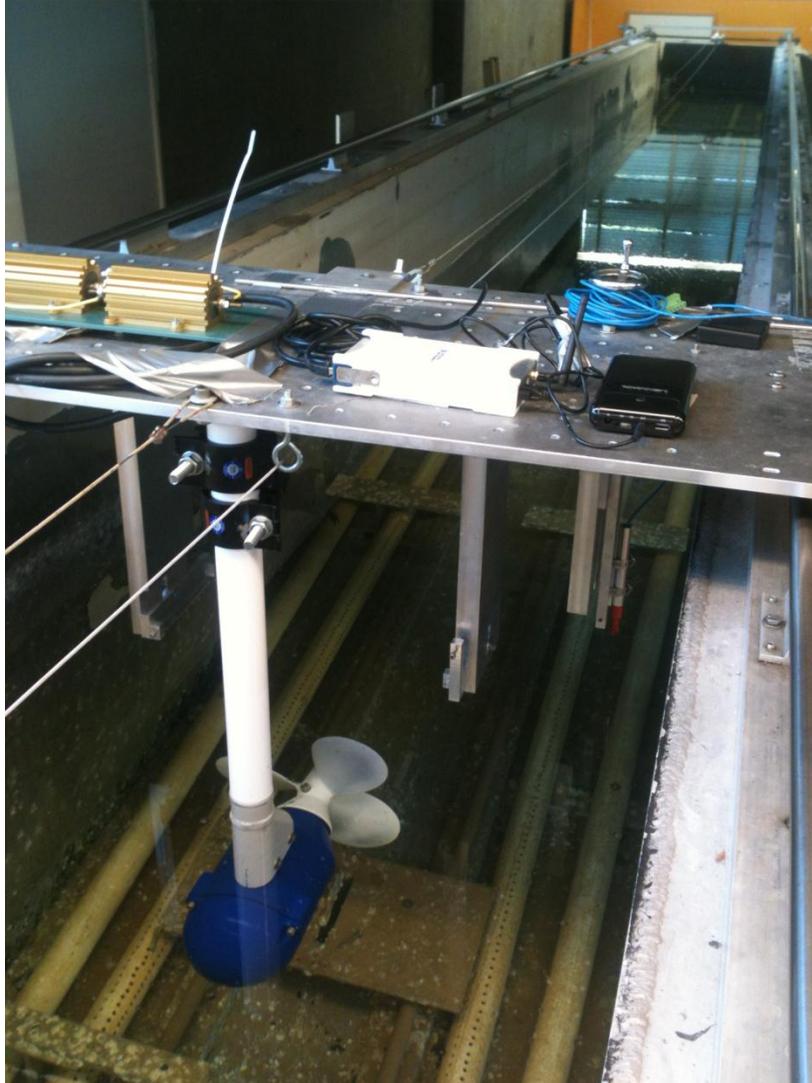
Figure 20.    Photo of towing carriage with full turbine configuration and
a 20 ohm resistive load in circuit.


It was expected that the voltage output of the turbine would vary at different carriage speeds, however what was still unknown was the effect of the rotational speeds of the rotor and the subsequent drag forces experienced by the carriage and how they would compare to the non-rotational configuration.

(1) Rotational Rotor Raw Data

| 5 Ohm Full Turbine Data Averages | | | | | | |
|---|---|---|---|---|---|---|
| $U_\infty$ (m/s) | Drag Force (N) | Power (W) | Voltage (V) | Current (Amps) | RPM | $C_D$ |
| 0.68 | 11.70 | 1.31 | 2.48 | 0.50 | 99.26 | 0.66 |
| 0.86 | 18.42 | 3.57 | 4.12 | 0.82 | 142.90 | 0.66 |
| 1.03 | 27.72 | 7.70 | 6.17 | 1.23 | 190.82 | 0.69 |
| 1.21 | 37.97 | 9.34 | 6.75 | 1.35 | 247.63 | 0.69 |
| 1.37 | 48.45 | 14.42 | 8.33 | 1.67 | 297.03 | 0.67 |
| 1.55 | 61.02 | 20.97 | 10.15 | 2.03 | 353.29 | 0.67 |
| 1.70 | 74.08 | 25.33 | 11.16 | 2.23 | 404.08 | 0.67 |

Table 5.    Raw data for rotating full turbine with 5 Ohm resistive load.

| 10 Ohm Full Turbine Data Averages | | | | | | |
|---|---|---|---|---|---|---|
| $U_\infty$ (m/s) | Drag Force (N) | Power (W) | Voltage (V) | Current (Amps) | RPM | $C_D$ |
| 0.68 | 10.19 | 1.60 | 4.00 | 0.40 | 121.65 | 0.58 |
| 0.86 | 19.37 | 3.80 | 5.99 | 0.60 | 171.92 | 0.68 |
| 1.04 | 25.71 | 6.70 | 8.18 | 0.82 | 227.85 | 0.62 |
| 1.22 | 34.89 | 12.02 | 10.95 | 1.09 | 284.81 | 0.62 |
| 1.38 | 45.56 | 14.51 | 12.04 | 1.20 | 341.45 | 0.63 |
| 1.56 | 58.20 | 18.64 | 13.65 | 1.36 | 392.17 | 0.63 |
| 1.72 | 70.31 | 26.80 | 16.37 | 1.64 | 437.96 | 0.63 |

Table 6.    Raw data for rotating full turbine with 10 Ohm resistive load.

| 20 Ohm Full Turbine Data Averages | | | | | | |
|---|---|---|---|---|---|---|
| $U_\infty$ (m/s) | Drag Force (N) | Power (W) | Voltage (V) | Current (Amps) | RPM | $C_D$ |
| 0.68 | 8.72 | 1.54 | 5.54 | 0.28 | 142.18 | 0.49 |
| 0.86 | 15.10 | 2.90 | 7.61 | 0.38 | 202.70 | 0.53 |
| 1.03 | 23.33 | 6.44 | 11.35 | 0.57 | 263.74 | 0.57 |
| 1.21 | 32.86 | 9.47 | 13.76 | 0.69 | 326.98 | 0.59 |
| 1.37 | 42.56 | 11.34 | 15.06 | 0.75 | 384.62 | 0.59 |
| 1.56 | 53.57 | 21.00 | 20.49 | 1.02 | 436.36 | 0.58 |
| 1.74 | 65.97 | 23.87 | 21.85 | 1.09 | 497.93 | 0.57 |

Table 7.    Raw data for rotating full turbine with 20 Ohm resistive load.

| 30 Ohm Full Turbine Data Averages | | | | | | |
|---|---|---|---|---|---|---|
| $U_\infty$ (m/s) | Drag Force (N) | Power (W) | Voltage (V) | Current (Amps) | RPM | $C_D$ |
| 0.68 | 8.44 | 1.27 | 6.17 | 0.15 | 151.26 | 0.47 |
| 0.86 | 15.78 | 2.27 | 8.26 | 0.21 | 225.56 | 0.56 |
| 1.04 | 22.54 | 4.52 | 11.64 | 0.29 | 279.07 | 0.55 |
| 1.21 | 31.01 | 7.21 | 14.71 | 0.37 | 338.03 | 0.56 |
| 1.39 | 43.38 | 9.40 | 16.79 | 0.42 | 408.16 | 0.59 |
| 1.56 | 52.26 | 13.41 | 20.06 | 0.50 | 454.55 | 0.56 |
| 1.73 | 62.05 | 19.69 | 24.30 | 0.61 | 505.05 | 0.54 |

Table 8.    Raw data for rotating full turbine with 30 Ohm resistive load.

| 40 Ohm Full Turbine Data Averages | | | | | | |
|---|---|---|---|---|---|---|
| $U_\infty$ (m/s) | Drag Force (N) | Power (W) | Voltage (V) | Current (Amps) | RPM | $C_D$ |
| 0.69 | 8.31 | 1.04 | 6.44 | 0.16 | 168.07 | 0.46 |
| 0.87 | 14.43 | 2.56 | 10.12 | 0.25 | 231.66 | 0.50 |
| 1.05 | 21.38 | 3.50 | 11.83 | 0.30 | 289.86 | 0.51 |
| 1.22 | 30.28 | 5.66 | 15.04 | 0.38 | 351.91 | 0.53 |
| 1.39 | 39.47 | 8.21 | 18.12 | 0.45 | 406.78 | 0.54 |
| 1.55 | 51.31 | 9.84 | 19.84 | 0.50 | 459.77 | 0.56 |
| 1.72 | 63.35 | 14.43 | 24.02 | 0.60 | 508.47 | 0.56 |

Table 9.    Raw data for rotating full turbine with 40 Ohm resistive load.

The values for drag coefficients increase as both the carriage velocity increases and the rotational speed of the rotor increases. Also, as resistance in the generator output circuit increases, the rotational speed of the rotor also increases due to the drop in output current generated by the turbine (less work done by the generator translates directly to a decrease in torque required to turn the rotor). Although the overall drag force experienced by the load cell also decreases as the drag coefficient decreases, the power produced by the turbine also decreases. This key observation will be discussed later in greater detail in the results section of the experimental analysis.
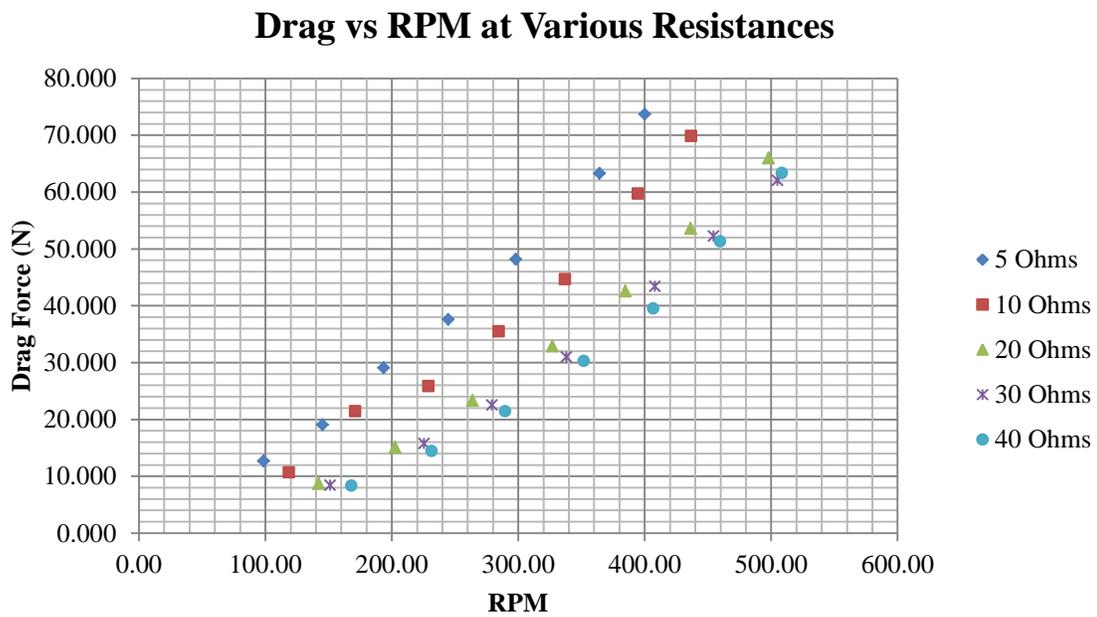


Figure 21.   Drag force and RPM correlation at various resistances in the circuit for full turbine configuration.

**Power vs RPM for Various Resistances**
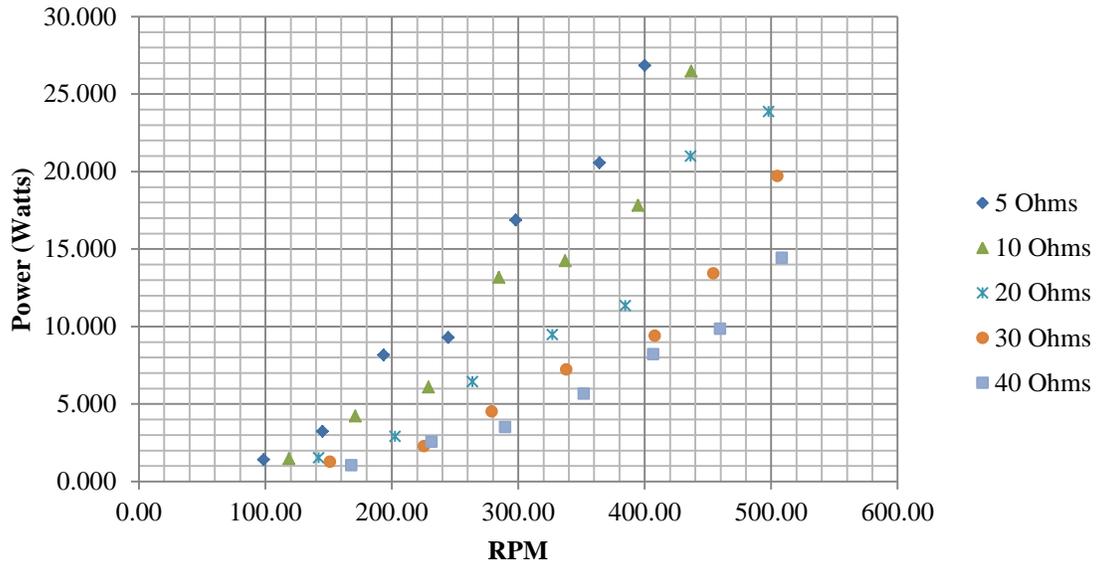


Figure 22.    Power and RPM correlation at various resistances in the circuit for full turbine configuration.

In calculating the various drag coefficients for the rotating full turbine configuration, it is important to note that the rotational forces of the rotor are a function of both the electrical power generation and the fluid dynamic forces that produce rotation.    As expected, power generation increases as the experienced drag force increases in all cases, though the Power is primarily a function of the turbine's measured rotational speed as shown in Figure 22.  The calculated drag coefficients for the rotational configuration of the turbine are significantly lower than those of the non-rotational configuration primarily due to the increase in projected area (non-rotational area = 0.03645 m$^2$, rotational/swept area = 0.07645 m$^2$), though it is also noteworthy that the rotational trials with higher electric resistance experienced a higher drag force compared to the non-rotational configuration, and trials with lower electric resistance experienced a slightly lower drag force (shown in Figure 21).  Figure 23 shows the non-rotational configuration as it compares to the highest and lowest resistances for the rotational trials.

**Drag Force Summary**
**(Rotational and Non-rotational comparison)**
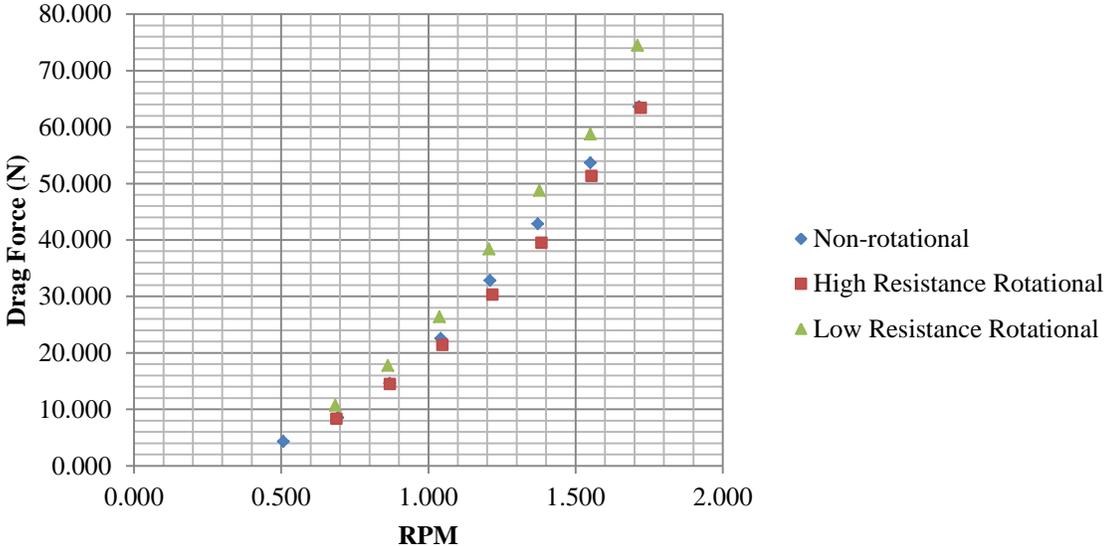
Figure 23.    Drag force comparison between non-rotational trials to both high and low electrically resisted rotational trials.

A summary of the experimentally acquired raw data with calculated drag force coefficients is listed in Table 10.  For the rotating, full turbine configurations, the report includes both the low and the high value for calculated drag coefficient (low value corresponds with low RPM rotation with 40 Ohms resistance in circuit at the output of the generator, and high value with high RPM at 5 Ohm resistance).

Table 10.     Summary of models' projected area and their calculated drag coefficients
from the raw data.

| Model | Projected Area | Calculated Drag Coefficients |
|---|---|---|
| Plate A | $0.05822 \text{ m}^2$ | 1.24 |
| Plate B | $0.040828 \text{ m}^2$ | 1.27 |
| Generator Alone | $0.015394 \text{ m}^2$ | 0.87 |
| Full Turbine Non-rotational | $0.03645 \text{ m}^2$ | 1.125 |
| Full Turbine Rotational* (Low RPM, 40 Ohm) | $0.07645 \text{ m}^2$ | 0.46 |
| Full Turbine Rotational* (High RPM, 5 Ohm) | $0.07645 \text{ m}^2$ | 0.67 |
| * area calculated is the rotor's swept area | | |

### 3.     Blockage Correction

#### a.     *Discussion*

As a model travels through a fluid in a finite control volume, the width of that control volume, or tank, causes a blockage effect, whereby the fluid is channeled around the model as it passes through the control volume.  The effect of this fluid channeling is the increase in relative speed between the model and the surrounding fluid.  To counter this relative increase in velocity, a small correction is made to the measured velocity that is proportional to the ratio of model cross-sectional area and control volume cross-sectional area.

According to the International Towing Tank Conference (ITTC), when looking at the ratio of the model-to-tank cross-sectional area, if the ratio is less than one-half percent, blockage effects are negligible.  If, however the ratio is larger than one percent, a correction to the measured velocity speed should be implemented [6].  Since the calculated drag is a function of the velocity squared, any change to the measured velocity input to that function is significant and requires a high degree of accuracy.  In the case of our towing tank and the cross sections areas of our models, a blockage correction was included with our data, thus changing our raw data to corrected data

33

primarily for calculations involving the drag coefficient.

### b. *Application*

The cross sectional area of the tank was measured at 0.7835 m$^2$. This value was used to determine the ratio of cross sections for both plates as well as for the turbine (using the swept area value for corrections to rotor trials). The cross sectional areas are shown in Figure 24.

Table 11.    Blockage correction summary.

| Model | Tank | Cross-sectional Area | Blockage Correction | |
|---|---|---|---|---|
| | | 0.7835 | Ratio | % added to velocity |
| Flat Plate | Plate A | 0.05882 | 0.07507 | 7.5 |
| | Plate B | 0.04083 | 0.05211 | 5.2 |
| Gen Only | Generator | 0.01539 | 0.01964 | 2.0 |
| Rotor | Non-rotational | 0.03645 | 0.04652 | 4.7 |
| | Rotational | 0.07645 | 0.09758 | 9.8 |
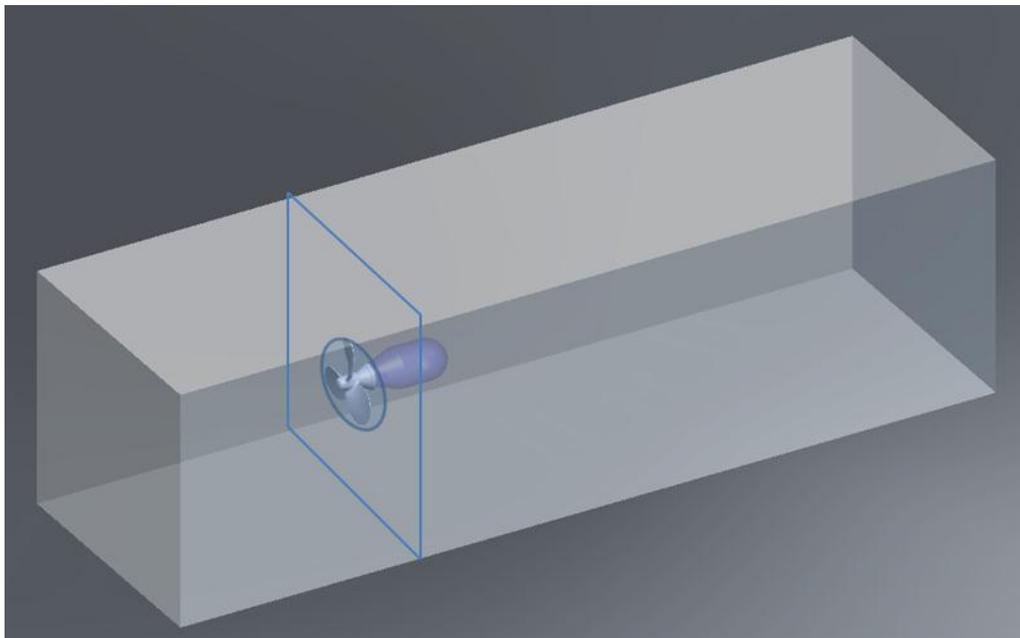
Figure 24.    Visual display of cross-sectional areas used for blockage correction on rotational configuration.

Applying the blockage correction, $U_\infty(BC\%)$, to the velocity values inputted into Eqn. (1) results in the following equation (with tabulated results in Table 12):

$$F_D = \frac{1}{2}\rho\left(U_\infty + \left(U_\infty BC\%\right)\right)^2 AC_D \tag{2}$$

$F_D$     the measured drag force

$U_\infty$     the fluid flow velocity approaching the plate

$\rho$     the density of the fluid

$BC\%$   calculated blockage correction factor

$A$     the swept area, or projected area of model

$C_D$     the drag coefficient

Table 12.     Results for flat plate analysis with blockage correction applied.

| 3-Trial Average - Plate A | | | | 3-Trial Average - Plate B | | | |
|---|---|---|---|---|---|---|---|
| $U_\infty$ (m/s) | Drag Force* (N) | $C_D$ (uncorrected) | $C_D$ (corrected) | $U_\infty$ (m/s) | Drag Force* (N) | $C_D$ (uncorrected) | $C_D$ (corrected) |
| 0.50 | 3.90 | 0.545 | 0.472 | 0.50 | 4.46 | 0.862 | 0.779 |
| 0.68 | 11.55 | 0.870 | 0.753 | 0.69 | 9.66 | 1.005 | 0.908 |
| 0.85 | 23.51 | 1.126 | 0.974 | 0.86 | 16.85 | 1.115 | 1.008 |
| 1.01 | 39.71 | 1.334 | 1.154 | 1.04 | 27.01 | 1.236 | 1.117 |
| 1.18 | 57.72 | 1.431 | 1.239 | 1.20 | 37.13 | 1.257 | 1.136 |
| 1.34 | 75.61 | 1.456 | 1.260 | 1.37 | 50.82 | 1.329 | 1.201 |
| 1.49 | 98.67 | 1.522 | 1.317 | 1.55 | 60.36 | 1.241 | 1.121 |
| 1.63 | 115.04 | 1.488 | 1.287 | 1.72 | 68.23 | 1.137 | 1.027 |

When compared to the literature value of 1.17 for the $C_D$ of a flat plate, it would seem as though the blockage correction dropped our calculated values too low (uncorrected average $C_D$ = 1.147 and corrected average $C_D$ = 1.037), however, as will be discussed later, there exists a region of reduced measuring uncertainty between 0.8 and 1.3 m/s in which our measuring accuracy and consistency improves. This region would suggest an average $C_D$ value of 1.115 for the corrected data versus 1.234 for the uncorrected data.

**Drag Coefficient vs Velocity for Flat Plates**
**(with Blockage Correction)**
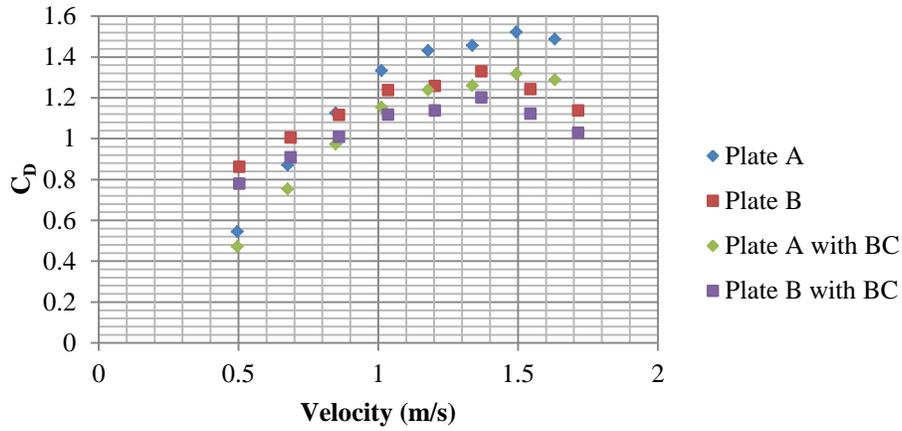
Figure 25.    Results for flat plate analysis with blockage correction applied.

As seen in Figure 25, the overall effect of applying the blockage correction to the experimental data reduces the calculated drag coefficients.  Similarly with the results from the non-rotational trials (Table 13 and Figure 26):

Table 13.    Results for non-rotational rotor configuration with blockage correction applied.

| Experimental Data (Non-rotational Rotor) | | | |
|---|---|---|---|
| $U_\infty$ (m/s) | Drag Force (N) | $C_D$ (uncorrected) | $C_D$ (corrected) |
| 0.508 | 4.322 | 0.920 | 0.839 |
| 0.693 | 8.546 | 0.979 | 0.893 |
| 0.869 | 14.596 | 1.064 | 0.970 |
| 1.042 | 22.530 | 1.141 | 1.041 |
| 1.210 | 32.825 | 1.233 | 1.125 |
| 1.372 | 42.846 | 1.251 | 1.141 |
| 1.550 | 53.680 | 1.228 | 1.121 |
| 1.716 | 63.590 | 1.187 | 1.083 |

**Drag Coefficient vs Velocity for non-rotational Configuration**
**(with Blockage Correction)**
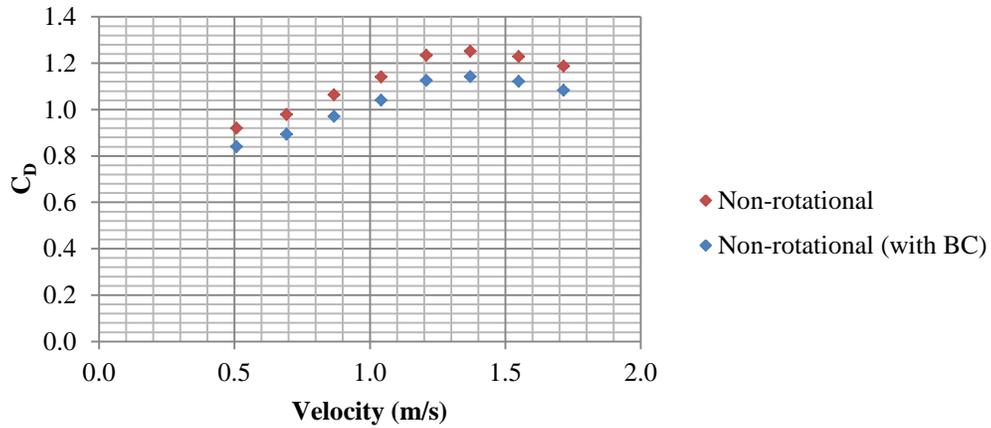


Figure 26.   Results for non-rotational rotor configuration with blockage correction applied.

And finally the data for the rotational turbine configurations at various electrical resistances are shown below with the applied blockage correction to the calculated drag coefficients:

| 5 Ohm Full Turbine Data Averages with applied blockage correction | | | |
|---|---|---|---|
| $U_\infty$ (m/s) | Drag Force (N) | $C_D$ (uncorrected) | $C_D$ (corrected) |
| 0.68 | 11.70 | 0.66 | 0.55 |
| 0.86 | 18.42 | 0.66 | 0.55 |
| 1.03 | 27.72 | 0.69 | 0.57 |
| 1.21 | 37.97 | 0.69 | 0.57 |
| 1.37 | 48.45 | 0.67 | 0.56 |
| 1.55 | 61.02 | 0.67 | 0.55 |
| 1.70 | 74.08 | 0.67 | 0.56 |

Table 14.   Blockage correction data for rotating full turbine with 5 Ohm resistive load.

| 10 Ohm Full Turbine Data Averages with applied blockage correction | | | |
|---|---|---|---|
| $U_\infty$ (m/s) | Drag Force (N) | $C_D$ (uncorrected) | $C_D$ (corrected) |
| 0.68 | 10.19 | 0.58 | 0.48 |
| 0.86 | 19.37 | 0.68 | 0.56 |
| 1.04 | 25.71 | 0.62 | 0.51 |
| 1.22 | 34.89 | 0.62 | 0.51 |
| 1.38 | 45.56 | 0.63 | 0.52 |
| 1.56 | 58.20 | 0.63 | 0.52 |
| 1.72 | 70.31 | 0.63 | 0.52 |

Table 15.    Blockage correction data for rotating full turbine with 10 Ohm resistive load.

| 20 Ohm Full Turbine Data Averages with applied blockage correction | | | |
|---|---|---|---|
| $U_\infty$ (m/s) | Drag Force (N) | $C_D$ (uncorrected) | $C_D$ (corrected) |
| 0.68 | 8.72 | 0.49 | 0.41 |
| 0.86 | 15.10 | 0.53 | 0.44 |
| 1.03 | 23.33 | 0.57 | 0.48 |
| 1.21 | 32.86 | 0.59 | 0.49 |
| 1.37 | 42.56 | 0.59 | 0.49 |
| 1.56 | 53.57 | 0.58 | 0.48 |
| 1.74 | 65.97 | 0.57 | 0.47 |

Table 16.    Blockage correction data for rotating full turbine with 20 Ohm resistive load.

| 30 Ohm Full Turbine Data Averages with applied blockage correction | | | |
|---|---|---|---|
| $U_\infty$ (m/s) | Drag Force (N) | $C_D$ (uncorrected) | $C_D$ (corrected) |
| 0.68 | 8.44 | 0.47 | 0.39 |
| 0.86 | 15.78 | 0.56 | 0.46 |
| 1.04 | 22.54 | 0.55 | 0.46 |
| 1.21 | 31.01 | 0.56 | 0.46 |
| 1.39 | 43.38 | 0.59 | 0.49 |
| 1.56 | 52.26 | 0.56 | 0.46 |
| 1.73 | 62.05 | 0.54 | 0.45 |

Table 17.    Blockage correction data for rotating full turbine with 30 Ohm resistive load.

| 40 Ohm Full Turbine Data Averages with applied blockage correction | | | |
|---|---|---|---|
| $U_\infty$ (m/s) | Drag Force (N) | $C_D$ (uncorrected) | $C_D$ (corrected) |
| 0.69 | 8.31 | 0.46 | 0.38 |
| 0.87 | 14.43 | 0.50 | 0.41 |
| 1.05 | 21.38 | 0.51 | 0.42 |
| 1.22 | 30.28 | 0.53 | 0.44 |
| 1.39 | 39.47 | 0.54 | 0.45 |
| 1.55 | 51.31 | 0.56 | 0.46 |
| 1.72 | 63.35 | 0.56 | 0.46 |

Table 18.    Blockage correction data for rotating full turbine with 40 Ohm resistive load.

**Drag Coefficient vs Velocity for Rotational Turbine
at Various Applied Resistances
(with Blockage Correction)**
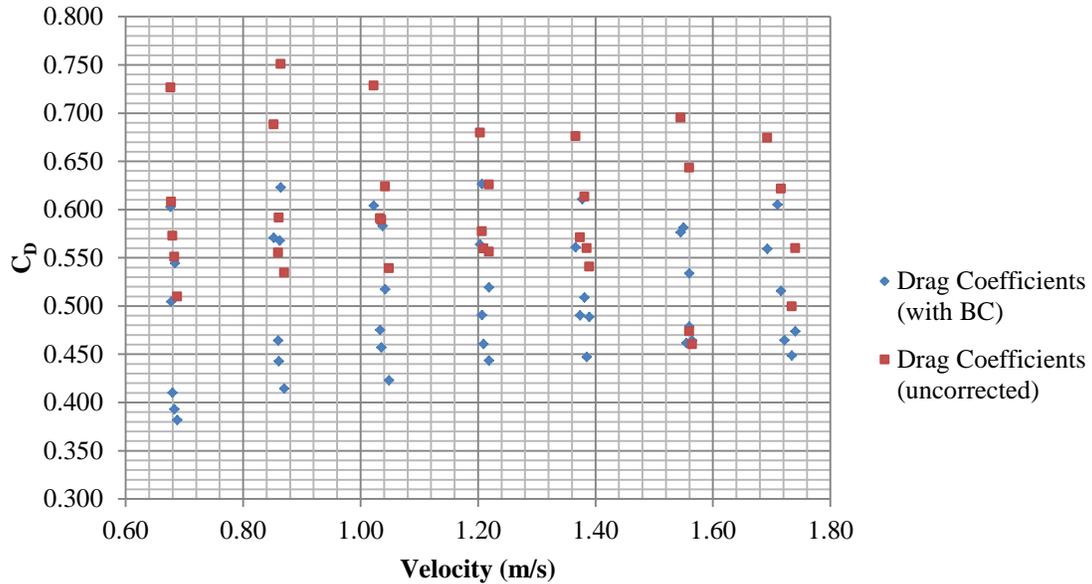


Figure 27. Calculated drag coefficients for full turbine at various loads with blockage correction applied to data.

## C. DISCUSSION OF RESULTS

For the following sections, only data with applied blockage correction will be analyzed and discussed. There is little justification within the arena of experimental tow tank procedures that do not incorporate these corrections, especially when the ratio of cross-sectional areas exceeds 1% for all of our models (generator alone cross-sectional ratio is 2.0%).

To better understand the meaning of our data with regards to the calculated drag coefficients, consider the flat plates traveling perpendicular to the fluid flow (Figure 28). If a fluid flow comes to a complete stop upon making contact with the object, a stagnation flow has developed and the drag coefficient would be equal to 1.0. The pressure distribution on the plate would be constant across the object and equal to the stagnation pressure.
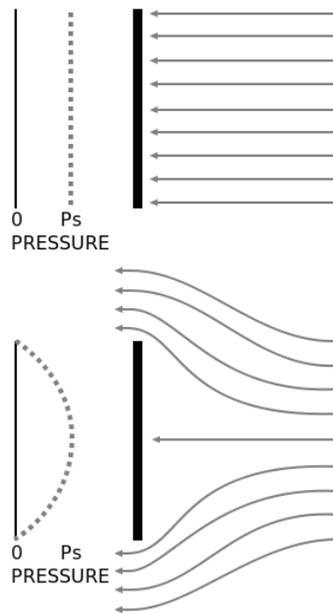
Figure 28.    Graphical representation of 2-D fluid flow about flat plates. From [14].

Conversely, if the fluid flow travels around the plate with variable pressure distribution and flow velocities, then the drag coefficient would be less than 1.0.  This would result in a negative pressure gradient relative to the surrounding pressure on the reverse side of the plate.  To put this into perspective, consider the drag coefficients for average automobiles is anywhere from $0.3 - 0.5$, and for aircraft anywhere from 0.02 to 0.09 [15].  For lower drag coefficients, resultant drag forces experienced by an object are also lower.  For this reason, we would expect the drag coefficients for our flat plates to be higher than our rotor, which would in turn be higher than our generator alone configuration.

Most fluids textbooks report a drag coefficient for a thin flat plate to be anywhere from 1.1 to 2.0, with most texts narrowing in on 1.18 for 3-D, fully turbulent flows [11]. Through experimentation, it has been observed that a cylinder traveling length-wise into a fluid flow, as the length decreases, the drag coefficient approaches 1.17 (with  Reynolds number greater than 1,000) - precisely what we would expect for a thin flat disk (cylinder with very small length).  Also, depending on the variability of the Reynolds number (a

function of the fluid's kinematic viscosity, and the object's velocity), the drag coefficient for an object may change slightly [14].

For these experiments, it was important to account for the flow characteristics of the fluid as well as the surface roughness and flexibility of the models observed. However we found that the values for flat plate drag coefficients were mostly affected by the variability of velocity and partial fluid separation visually observed during the higher speed trials. Conversely, for the trials involving the rotating blades, a more thorough analysis of the rotational effects on the boundary layer separation was required due to the wider range of drag coefficient values observed for various velocity and electric loading conditions.

### 1.     Flat Plate Results and Discussion

The drag coefficient calculated for a flat plate is a function of the pressure difference between the front and rear sides of the plate and the dynamic properties of the fluid flow. The pressure difference causes the plate to drag. Because our plate is less than 5 mm thin, skin friction experienced by the plate along these thin edges is assumed to be negligible. Therefore, the denominator of the coefficient is the product of the dynamic pressure of the undisturbed flow, $\frac{1}{2}\rho U_\infty^2$, and the projected area, $A$. Being independent of the size of the body (but not its shape), $C_D$ is generally a function of the Reynolds number. However, for our flat plate and disk, flow separation is insensitive to Reynolds number because of the sharp edges (see Frank White's remarks preceding table 7.3 in [11]). For this reason, variability in the calculated values for drag coefficient is likely due to the experimental uncertainty.

In order to analyze the values of our drag coefficients as a function of their respective Reynolds number, it is important to note that for most of our tow tank trials, the degree of accuracy expected with data acquired at low carriage speeds (0.5 – 0.8 m/s), varied. The measured drag force for a model pulled through the tank was at times only

slightly greater than those values recorded for the sled alone configuration. Any data pulled from our low-speed trials is at best just outside the margin of error (+/- 20%) and at worst, regarded as unusable data.

Additionally, when our flat plate models traveled through the tank at speeds greater than 1.3 m/s, a noticeable increase in wave formation was observed. Though this observation does not negate the usability of our data, it is worth including in our discussion as wave formation obfuscates the reliability of our drag coefficient calculations. As shown in Figure 7, the process for reducing the data from our load cell measurements at higher speeds required an analysis within a much tighter range of data. For our max speed of 1.8 m/s, the usable data within the steady state region was sometimes as small as one or two seconds only.

With that in mind, our critical analysis was focused on data acquired between 0.8 m/s and 1.3 m/s (this region is highlighted in Figure 29 for our flat plate trials).
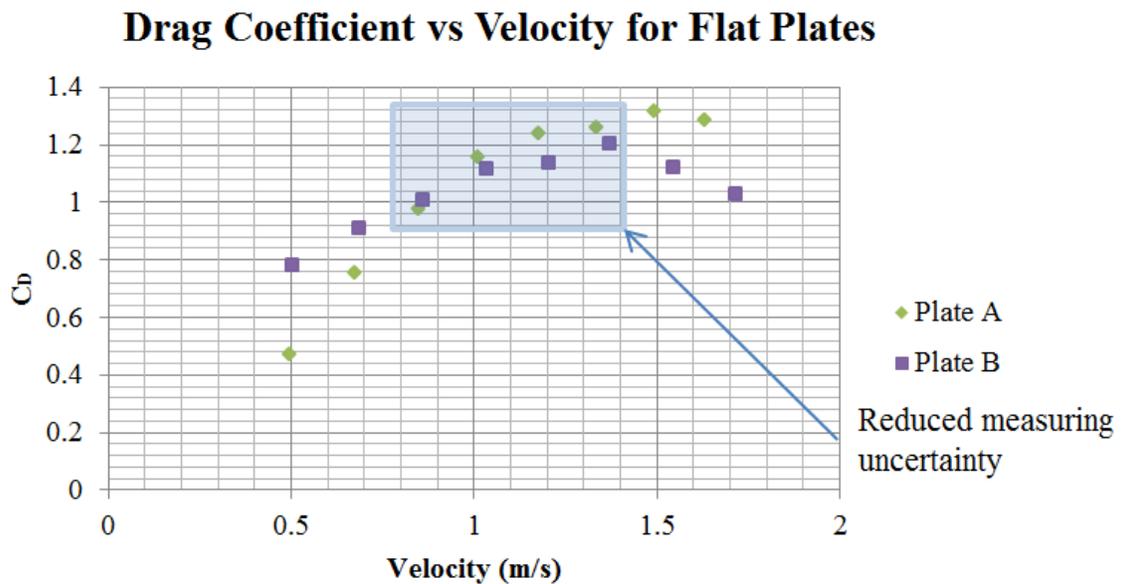


Figure 29.    Drag coefficient data vs. velocity for flat plate trials.

As carriage velocity increased the measured drag force also increased. To determine if the trend of our data was in fact quadratic, as was expected with the velocity

measurements squared, we then analyzed the $R^2$ value, or the coefficient of determination, for our drag forces data as a function of velocity. An $R^2$ near 1.0 indicates that a regression line fits the data well. It provides a measure of how well future outcomes are likely to be predicted by the model [16]. Trendlines with $R^2$ values for the flat plate trial is shown in Figure 30.
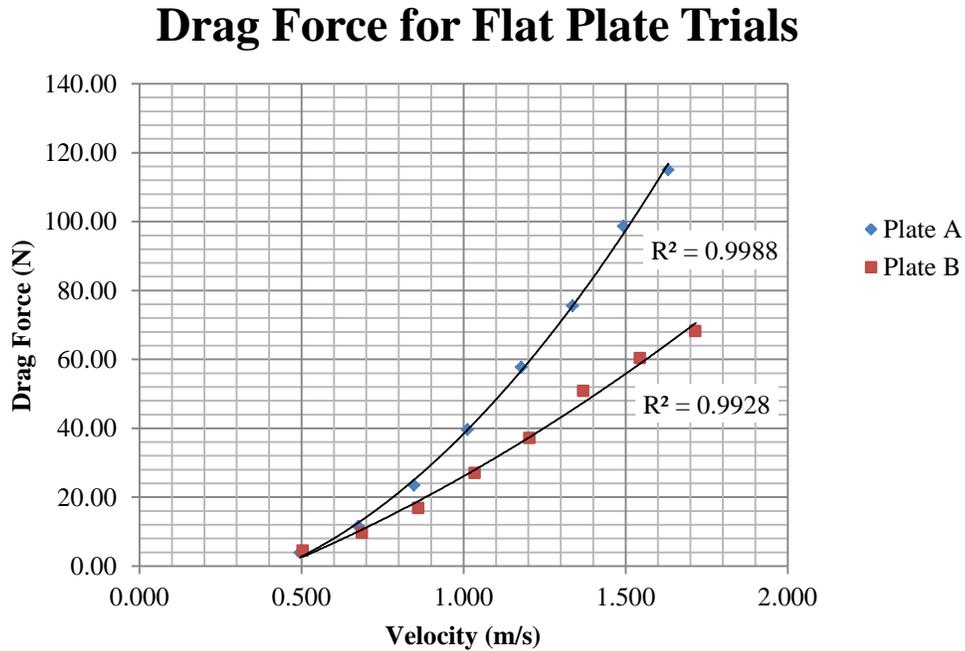


Figure 30.    Trendline data for flat plate trials, drag force vs. velocity.

## 2.    Generator Alone Results and Discussion

The calculated drag coefficients for the generator alone configuration fell between 0.56 and 0.92 (within the region of reduced measuring uncertainty). This data, though not defined specifically with any published data for this particular generator, can still be analyzed based on similar shapes and dimensions.

Frank White discussed the drag on 3-D bodies at $Re > 10^4$ with turbulent flow characteristics in [11] (all of our Reynolds number data falls into this category). For an ellipsoid-shaped object with a length-to-diameter ratio of 2 (the L/d ratio for our generator 2.04) the turbulent value for $C_D$ is listed as 0.13. For a cone-shaped frontal

area, the reported C$_D$ incident angle, $\theta$, of approx. $75^o$ is 1.05 (approximate incident angle for our generator).
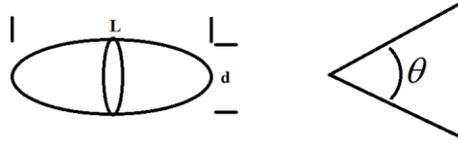


Figure 31.   Visual representation of geometric shapes with known drag coefficients.

With these general geometric outliers, we would expect our generator's C$_D$ to fall somewhere in between 0.13 and 1.05.   Additional data can be found for 3-D objects of similar shape and size.   However, these values typically fall between the values identified above, and none are quite precise in their geometric similarities to our generator.

Unlike for the flat plate analyses, the Reynolds number dependence cannot be ignored for the generator or full turbine configurations.   To calculate the Reynolds numbers for our generator, we used the following equation:

$$\mathrm{Re} = \frac{U_\infty D}{v}$$

(3)

$\mathrm{Re}$    is the Reynolds number

$U_\infty$    is the fluid flow velocity approaching the model

$D$    is the diameter of the generator's body

$v$    is the kinematic viscosity of water at $20^o$C

46

| *Re* | $U_\infty$ (m/s) | Drag Force (N) | $C_D$ |
|---|---|---|---|
| 7.24E+04 | 0.52 | 3.56 | 1.716 |
| 9.81E+04 | 0.70 | 3.72 | 0.979 |
| 1.23E+05 | 0.88 | 5.76 | 0.965 |
| 1.49E+05 | 1.07 | 6.68 | 0.764 |
| 1.74E+05 | 1.25 | 9.15 | 0.765 |
| 1.98E+05 | 1.42 | 9.26 | 0.600 |
| 2.24E+05 | 1.61 | 11.77 | 0.593 |
| 2.49E+05 | 1.79 | 14.19 | 0.578 |
| $D = 0.14$ m | | | |
| $\nu = 1.004 \times 10^{-6}$ | | | |

Table 19.    Data summary for generator alone configuration.

After neglecting the data points that lie outside the area of reduced uncertainty, the average drag coefficient for the generator alone was determined to be approximately 0.68. This value falls within the expected data range for this shape. Figures 32 and 33 show the calculated drag coefficients as a function of velocity and Reynolds number respectively.
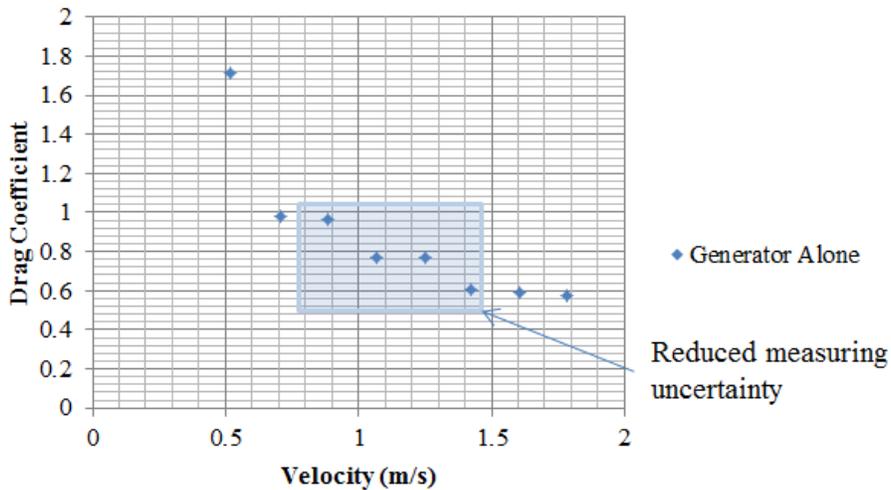


Figure 32.    Drag coefficient vs. velocity for generator alone trials.

**Drag Coefficient vs. Reynolds Number for Generator Alone**
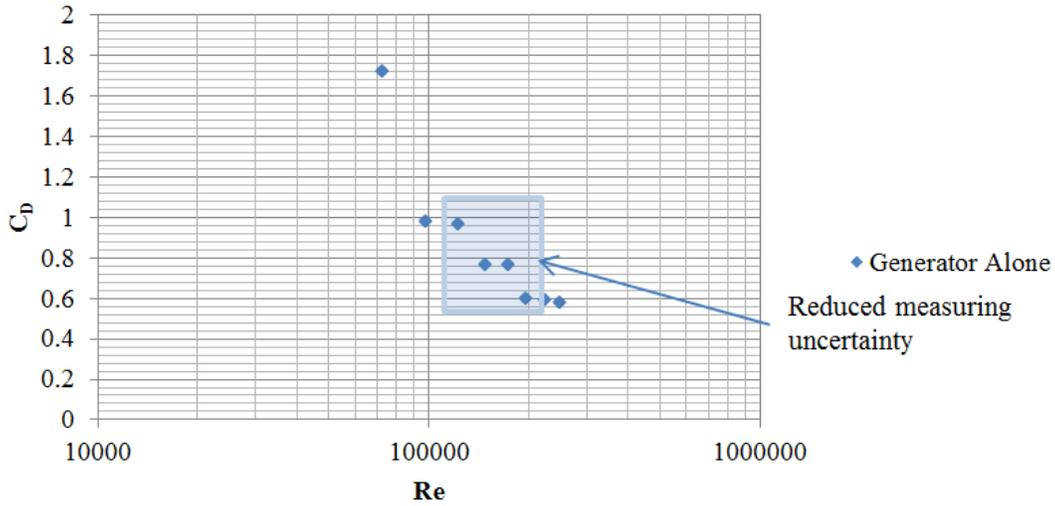
Figure 33.    Drag coefficient vs. Reynolds number for generator alone trials.

Finally, the $R^2$ value for the data fit to a quadratic trendline was 0.9831 indicating a fairly good fit to the expected quadratic relationship between drag force and velocity (Figure 34).

**Drag Force vs Velocity**

$R^2 = 0.9831$
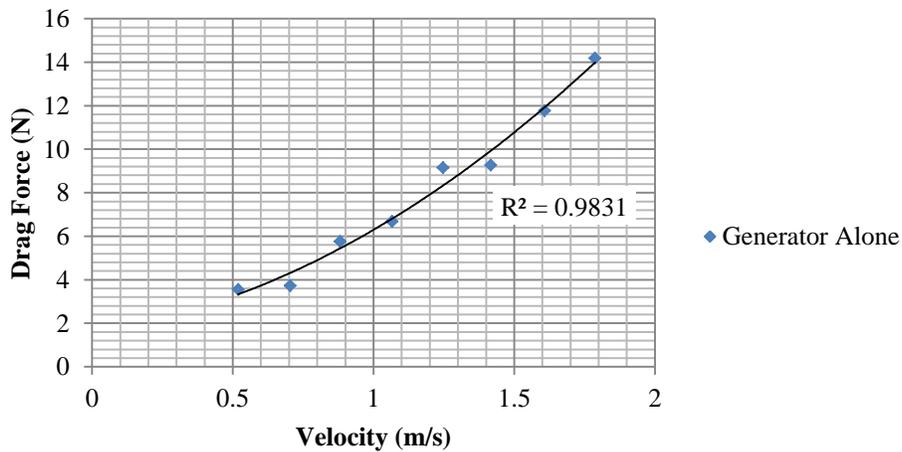
Figure 34.    Trendline data for generator alone configuration, drag force vs. velocity.

### 3. Non-rotational AFHT Results and Discussion

Each of the rotor blades was designed with hydrodynamic considerations in mind. The initial design was taken from an outboard motor propeller which was intended to convert motor-generated torque into axial force. When used in the opposite direction, propellers can be converted into turbine rotors by transferring axial-flow hydrodynamic forces into generator torque for power generation, which was the case for our particular rotor. With this in mind, the assumption was that this rotor would not be an ideally optimized rotor for use on hydrodynamic power turbines, but rather would merely get the job done.

Despite the geometric differences between the non-rotational rotor and a flat disk, one would expect to see values for drag coefficients in the range of $1.0 - 1.3$ based solely on the perpendicular orientation to the fluid flow (rather than in the range of elliptic or cone shaped geometries). Using the same methods we used to determine the drag coefficients for the flat plates and the generator, we were able to determine the calculated drag coefficients within the region of reduced measuring uncertainty ($0.8 - 1.3$ m/s).
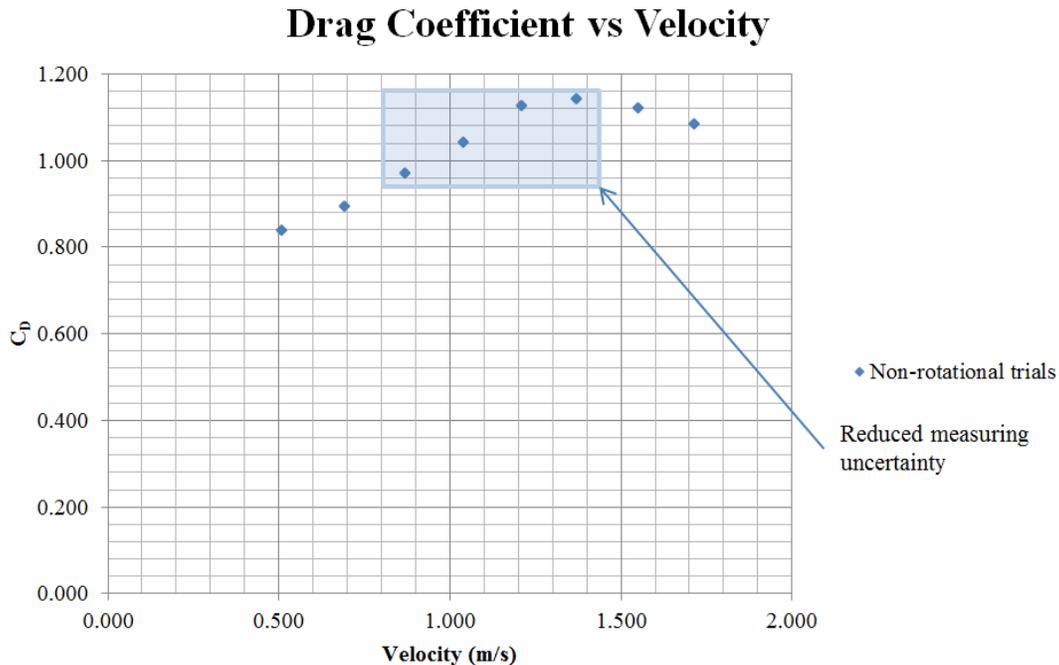


Figure 35. Drag coefficient vs. velocity for non-rotational full turbine configuration trials.

49

Averaging the data points from the region of reduced measuring uncertainty resulted in a drag coefficient for the non-rotational full turbine configuration of 1.069 (shown in Figure 35). Since the rotor's blades are not entirely perpendicular to the fluid flow like a flat plate, a value less than 1.17 is agreeable. Values in the range of 0.3 to 0.7 would bring into question the rotor's ability to capture the greatest amount of hydrodynamic power available in the fluid flow. Such values might be more appropriate for automobiles where minimizing drag is an important design aspect. Conversely, drag coefficients for wind turbine rotors are significantly smaller (0.04 – 0.05 range) due to their requirement to capture power from lower density fluid flows much like an aircraft wing, thus requiring a far greater rotor swept area for efficient operations [11].

When the drag force data was fit with a trendline, an $R^2$ value of 0.9976 resulted, which would imply reasonable data output from the load cell as shown in Figure 36.
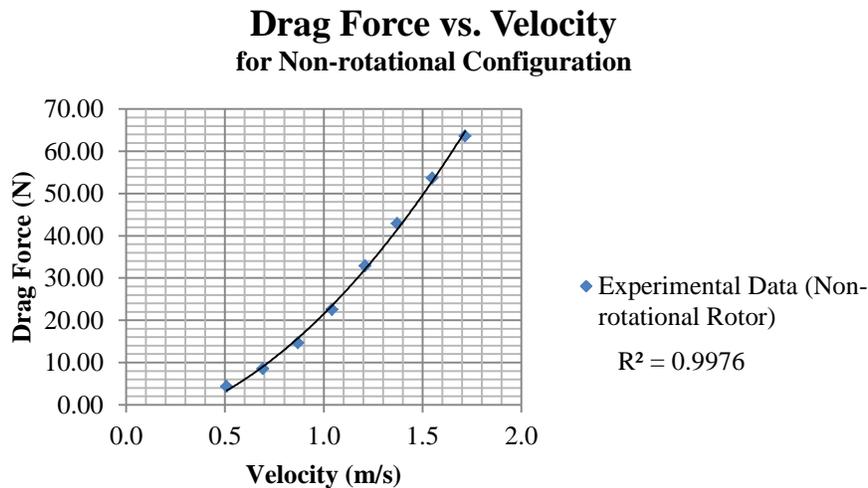


Figure 36.    Trendline data for non-rotational full turbine configuration, drag force vs. velocity.

With reasonably consistent drag force data acquired in the tow tank, the likely explanation for variability in drag coefficient values over the same range of Reynolds number is likely due to the location of the laminar to turbulent boundary layer transition for our rotor. For a flat plate, this transitional value was not important because the Reynolds number dependency was assumed insignificant.
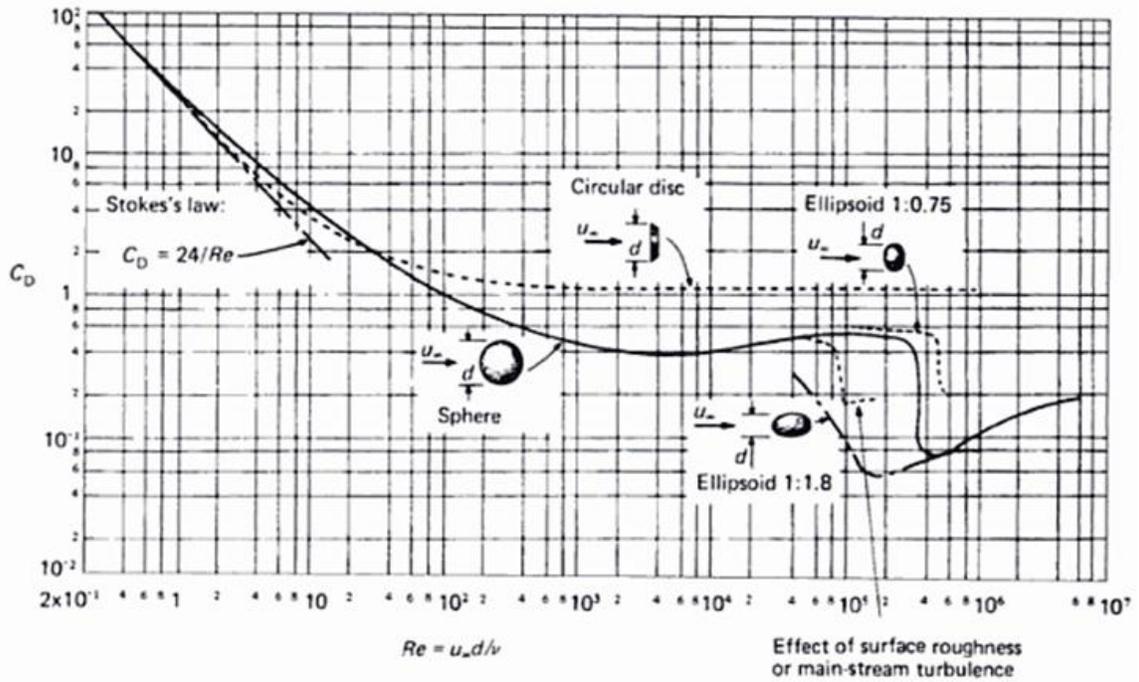
**Fig. 8.14** Drag coefficients of smooth, axially symmetric bodies.

Figure 37.    Drag coefficients of smooth, axially symmetric bodies at varying Reynolds numbers. From [17].

Based on transitional data for known 3-D axially symmetric bodies (reference Figure 8.14 from [17] reproduced as Figure 37), the transitional region for a rotor would likely occur at Reynolds number between $10^4$ and $10^7$ (the range in which our computed Reynolds numbers fall is between 2.1 to 5.4 x $10^5$ as shown in the figure below).
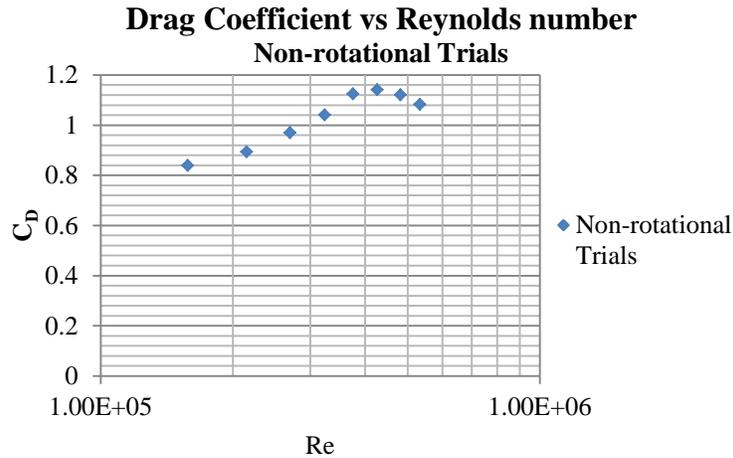


Figure 38.    Drag coefficient data vs. Reynolds number for non-rotational full turbine configuration.

Performing drag calculations within the transitional boundary layer region can result in inconsistencies.   Approximations made with fully turbulent boundary layer assumptions typically result in lower values for drag force and higher values for the calculated drag coefficients.   Conversely, erring on the side of laminar flow boundary layer approximations would result in calculated drag forces much higher than experimentation would suggest.  For this reason, drag coefficients with a variability of +/- 40% within such a narrow velocity range is not unusual for transitional boundary layer approximations [11].

It is likely that the transitional region would not settle out into a purely turbulent boundary layer regime until reaching a Reynolds number of at least $10^6$ (which for our rotor would require a water velocity greater than 3.25 m/s).

## 4.    Rotational AFHT Configuration

The fully rotational configuration of the AFHT is different from the previously discussed experiments in that there are other forces acting on the turbine rotor besides just the hydrodynamic pressure forces and forces due to the friction of the moving carriage over the rails. These are still the predominant forces in the AFHT's overall drag analysis, though additional electromotive forces must also be taken into account.

Generators produce a current by converting mechanical energy into electrical energy. The rotation of the generator's shaft turns a coil of wire through a magnetic field that flows from the stator part of the generator to the rotor. This change in the magnetic field due to the rotation of the coils induces a current. As the angular speed increases, the generator's electric current production also increases.

The magnitude of the electric current production is a function of the generator's electric load (or electric resistance in our case). The increase of our generator's circuit resistance resulted in less current production. This drop in current production resulted in a drop in electromotive forces acting against the rotation of the rotor. At lower electric resistances, more torque was needed to keep the generator turning at the speed required to produce current and the rotation of the turbine worked against the rotational forces supplied by the flow of water (recall Figure 21). A similar trend can be seen when comparing the drag forces of the turbine at different speeds across the same variation in electric loading (Figure 39).

# Drag Force vs Velocity for Full Turbine
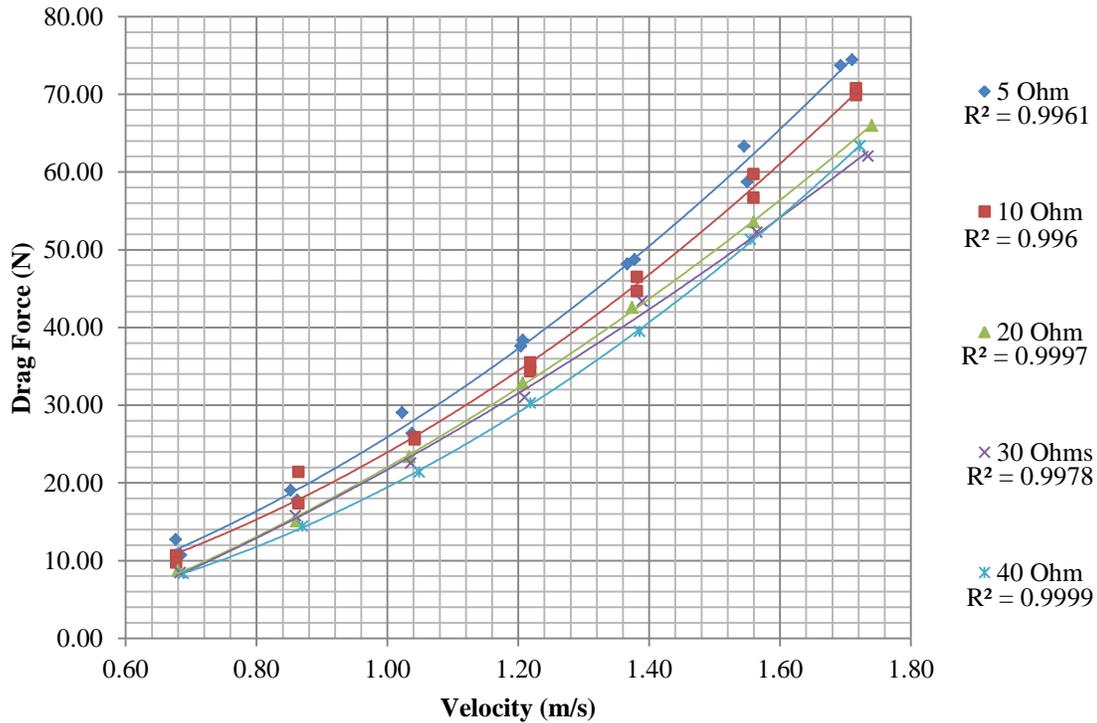


Figure 39.    Trendline data for rotational configuration of full turbine at various resistances, drag force vs. velocity.

The data in Figures 21 and 39 show clearly that the drag forces experienced by the turbine as it travels through the water are not merely a function of the hydrodynamic pressure forces, as was the case with the previous configurations (*flat plates, generator alone,* and the *non-rotational turbine* configurations), but also a function of the circuit's electrical load.  As the generator's electric output encountered greater resistance, the amount of current produced dropped which decreased the amount of electromotive force required to produce that current (less current production, less rotational opposition).  With less electromotive force opposing the rotation of the turbine, the rotor's predominant source of torque (the hydrodynamic forces) could then be assessed more as a function of fluid dynamics.  Notwithstanding, this turbine was designed for the purpose of power production, and the interest lies in determining its drag characteristics while performing the task of producing electricity.

The power production capability of the AFHT is a function of the rotational speed of the turbine (typically converted from axial flow velocities) as well as the resistance in the electric circuit (for a known current and voltage) as noted in the equations below.

$$P = \tau \omega \tag{4}$$

$$P = IV = \frac{V^2}{R} \tag{5}$$

| | |
|---|---|
| $P$ | Power |
| $\tau$ | the torque |
| $\omega$ | the angular velocity |
| $I$ | the electric current |
| $V$ | the measured voltage potential |
| $R$ | the electric resistance |

Since we were able to measure the voltage output for our turbine during the rotational trials, we could easily calculate the resultant power using Eqn. 5 above (with known resistances in the electric circuit). As expected, the power output increased as the rotational speed of the turbine increased. At the same time, the following graph shows the relationship between the power outputs for each of the resistances applied in the electric circuit. Though the resultant drag force decreased as the electric resistance increased the power output dropped, thus lowering the overall productivity of the power generator (Figure 40).

## Electric Power vs Rotational Speed
### for Various Resistances
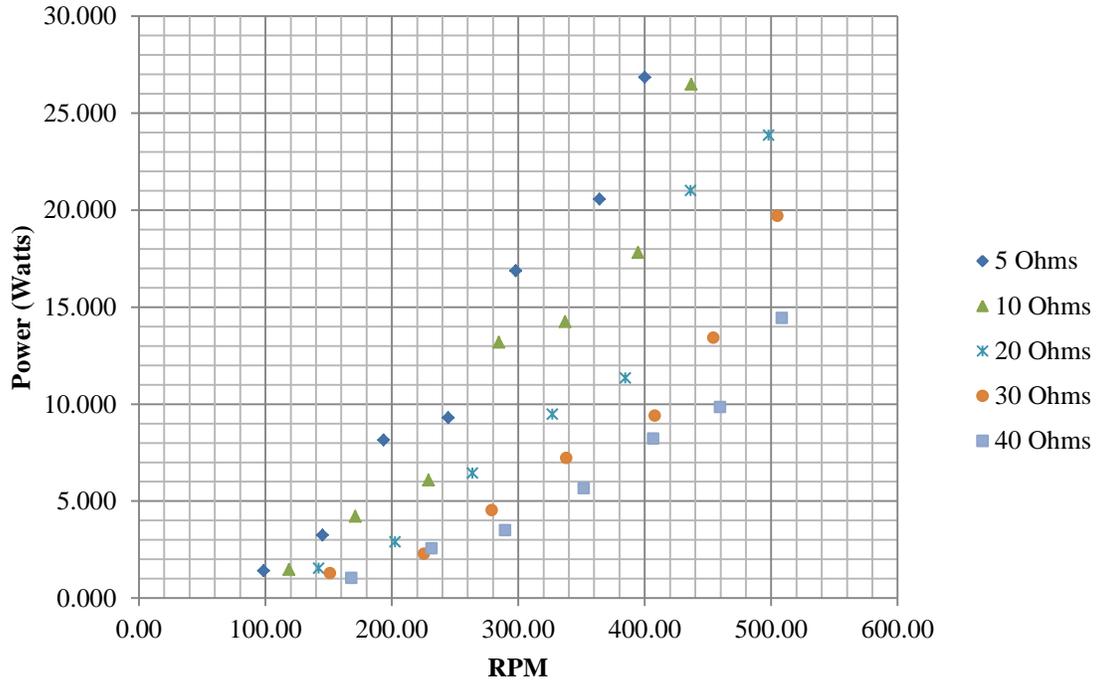


Figure 40.    Power production for rotating full turbine configuration at various resistances.

An additional equation necessary for a thorough analysis of a turbine's power production and drag characteristics is below:

$$P = \frac{1}{2}\rho U_\infty^{3} A C_P \tag{6}$$

| | |
|---|---|
| $P$ | Power |
| $\rho$ | the density of the fluid |
| $U_\infty$ | the velocity of the fluid flow |
| $A$ | the swept area, or projected area of model |
| $C_P$ | the power coefficient |

This equation shows the relationship between fluid flow velocities and a turbine's

swept area. Power output in a fluid flow is thus proportional to the third power of the fluid's speed (the available power increases eightfold when the water speed doubles). This equation is the same regardless if the fluid is water or wind by taking into account the fluid's density, $\rho$. The power coefficient is the most important variable in turbine dynamics. $C_P$ in Eqn. 6 is the turbine efficiency, where the maximum efficiency is given by the Betz limit of 0.593.

With two coefficients offered as tools for the evaluation of turbine characteristics, a more complete analysis can be completed.

### a.    *Drag Coefficient for Rotational AFHT*

As discussed in previous sections, the drag coefficient is not only a function of a model's geometry (shape and orientation to a fluid flow), but also the velocity of the fluid. Figure 41 is a general comparison between the rotational and non-rotational configurations of the full turbine.

**Drag coefficients vs Reynolds number**
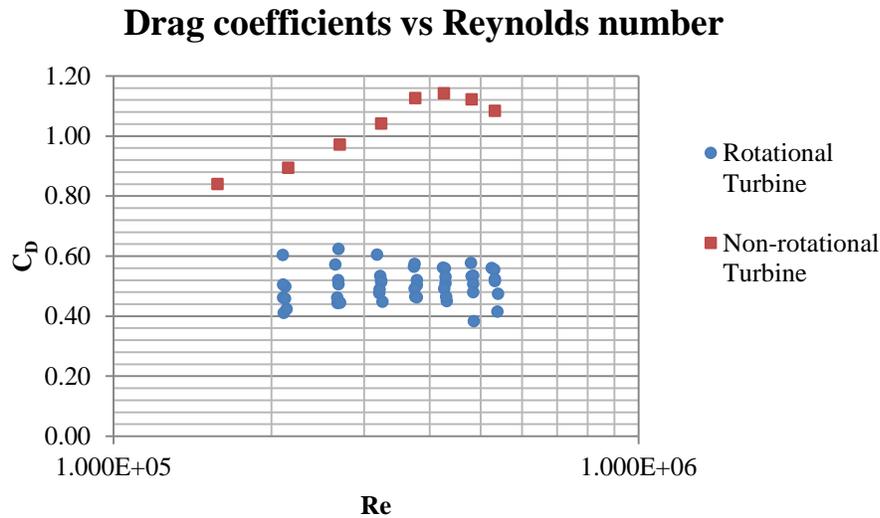


Figure 41.    Drag coefficient comparison between rotational and non-rotational configurations.

Though the values for non-rotational drag coefficients appear to be significantly higher than those of the rotational configuration, it is worth noting that the

values for $A$ used in Eqn. 1 are different by approximately 47.7% (refer to Table 11). If rotor swept area is used for the non-rotational turbine configuration (rather than the projected area), the results would match up more closely (as represented in the Figure 42).
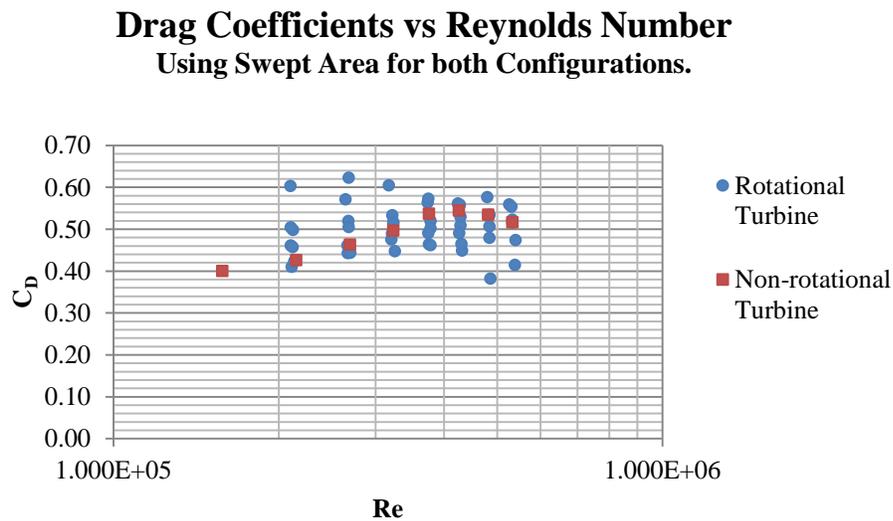
**Drag Coefficients vs Reynolds Number**
**Using Swept Area for both Configurations.**



Figure 42.    Drag coefficient comparison between rotational and non-rotational configurations (using swept area to calculate drag coefficients).

Though Figures 41 and 42 are not typical ways to represent data for power turbines, this visual representation is helpful for the purpose of seeing the scaled effect of a model's reference area when calculating drag coefficients.

### b.    *Power Generation Analysis*

The trendlines in Figure 43 show a steady increase in power output as velocity increases. Additionally, as the resistance increases the power drops.

**Power Output vs Velocity**
**(at Various Resistances)**
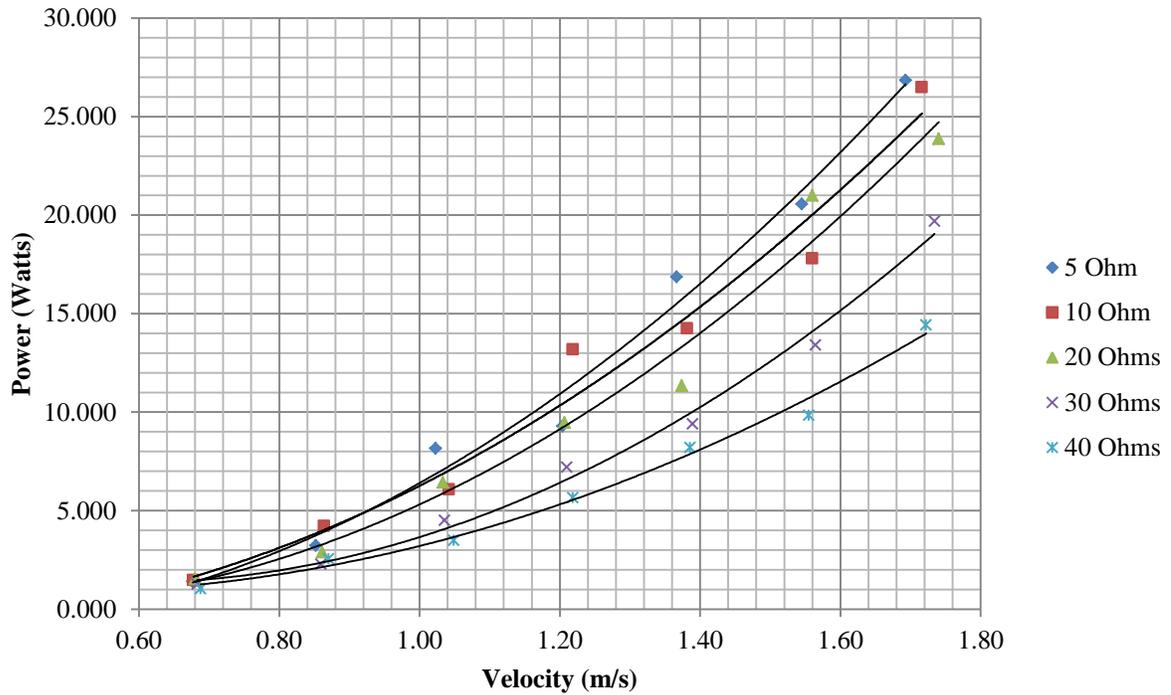


Figure 43.  Power as a function of velocity for various resistances for full turbine configuration.

This information, together with the power output trendlines shown as a function of rotational speed (recall Figure 22), can be put into non-dimensional terms as power coefficient versus tip speed ratio discussed below.  A typical way to represent data for power turbines (wind and hydro) is with a comparison between a turbine's Tip Speed Ratio (TSR) and the turbine's $C_P$.

The TSR is the ratio between the rotational speed of the tip of a blade and the actual velocity of the fluid.  It is an important non-dimensional characteristic of all turbine generators. If the rotor of the turbine turns too slowly, most of the fluid will pass undisturbed through the gap between the rotor blades.  If, however, the rotor turns too quickly, the blurring blades will appear like a solid wall to the fluid. Therefore, power turbines are designed with optimal tip speed ratios to extract as much power out of the fluid medium as possible [18].

In Figure 44, quadratic trendlines have been drawn to show the existence of optimal efficiencies at specific tip speed ratios for each electric loading for the turbine. Due to our limited range of fluid velocities available in our tow tank, inconsistencies were expected. Of note, $C_P$ values vary due to changes in the generator characteristics (electric loading or output resistance) much like $C_D$ values vary due to changes in model geometries and surface roughness. This trend is consistent with published wind turbine trends.

Similar to the region of reduced measuring uncertainty for our $C_D$ values, our experimental results for $C_P$ show a slight decrease in variability as the tip speed ratio increased (Figure 44). In other words, the error associated with measuring the power output of the turbine has decreased as the rotational speed of the turbine increased.

**Power Coefficient vs. Tip Speed Ratio**
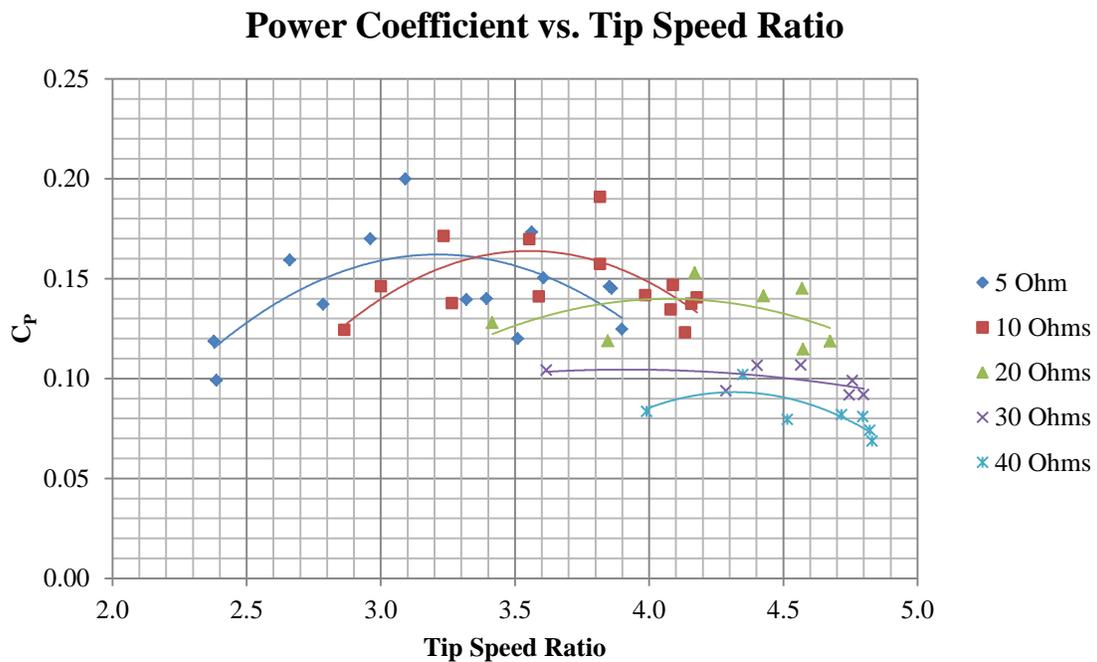


Figure 44. Power coefficient vs. tip speed ratio for full turbine configuration.

One possible explanation for this trend lies in the data reduction method used for recording power output values (an example of a typical power output signal for

our generator is shown in Figure 45). From this set of data points, an average power value was determined from the same range used in the drag force data reduction (steady state). At higher rotational speeds, the frequency of the power output increased which ultimately allowed for more data points to be averaged in our $C_P$ calculations. For this reason, the data points shown in Figure 44 appear to converge more as the rotational speed of the turbine increases.

**Power Output Signal for Turbine at 0.68 m/s**
**with 10 Ohms Resistor in Circuit**
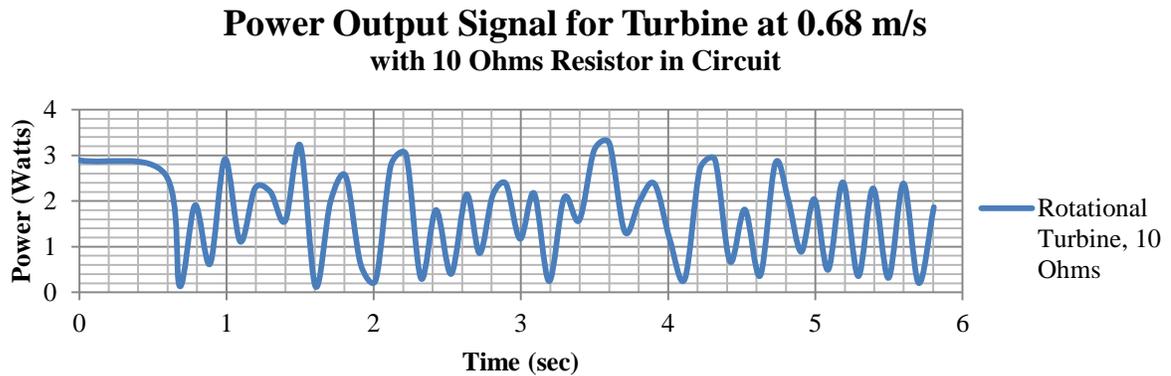


Figure 45. Power output signal from full turbine trial at 0.68 m/s.

Furthermore, when a rotor blade passes through a fluid medium, it leaves turbulence in its wake. If the next blade on the spinning rotor arrives at this point while the fluid is still turbulent, it will not be able to extract power efficiently from the fluid. The tip speed ratio is typically chosen so that the blades do not pass through turbulent fluid [18]. This becomes important when designing a generator's characteristic electromotive force across a wide range of loading conditions. Should the generator require a significant amount of torsion to overcome the electromotive force present in the generator's magnetic field, the unrestricted rotational characteristic of the rotor would become more hindered resulting in an increase in the drag the moment the rotor did not rotate freely as if would completely unloaded. At the same time, any hindrance in rotational speed experienced by the turbine might also translate into a gain in power production capabilities if that hindrance was the result of an increase in electric current production.

61

The effects of adding electrical resistance to the generator output and the resultant drop in power are observed by both the measured drop in voltages as well as the measured decrease in drag within the system. When looking at the turbine's power output as a function of the resultant drag force, although the data varies greatly (still within experimental uncertainty), it is possible to fit a series of linear trendlines within the data cluster that result in at least three near parallel lines (for the 5, 10 and 20-ohm resisted circuits). It would seem that there is indeed a linear relationship between the drag force of the turbine and its power output. The pursuit of a higher power output for this particular turbine will ultimately cost a vessel speed (losses due to drag) regardless what kind of loading is in the electrical circuit.
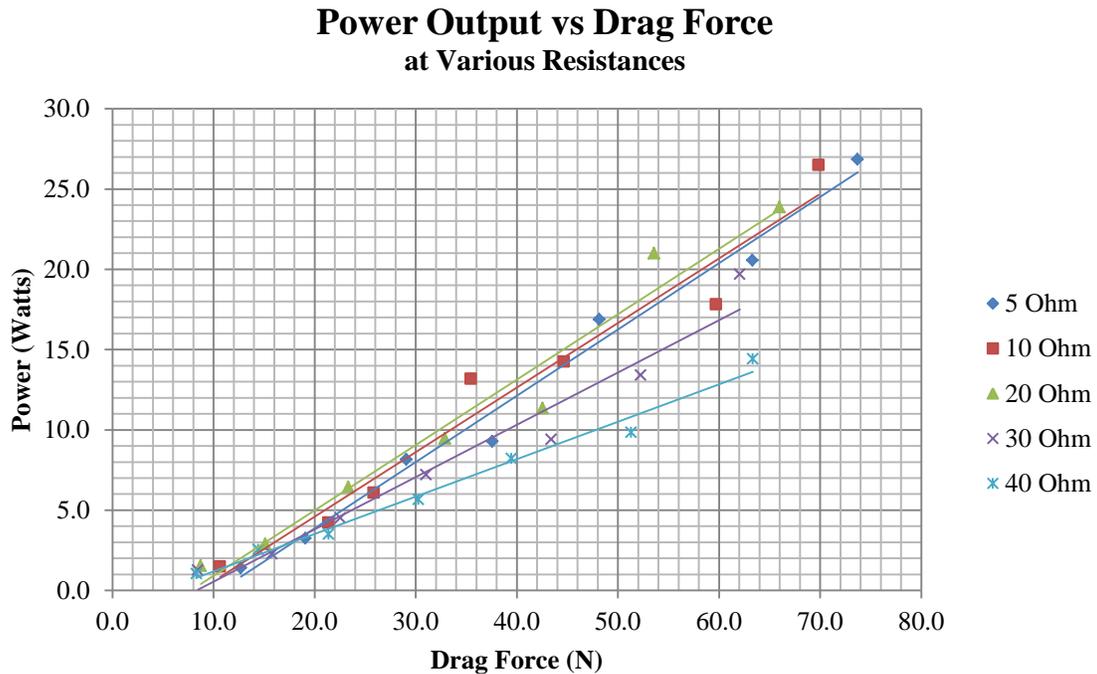


Figure 46.    Power output vs. drag force for full turbine configuration
with linear trendlines displayed.

Another way to look at the relationship between the drag force and power output is by comparing the rotational speed as a function of both electric loading and speed through the water (shown in Figure 46). One can see that for a given speed

through the water, depending on the electric loading, the experienced drag force is proportional to both the power output (as seen in Figure 46) as well as the rotational speed of the turbine (Figure 47). In other words, a vessel might lose speed either due to an increase in power production, or a decrease in electrical resistance in the circuit (both cases would accompany a decrease in rotational speed of the turbine as well).
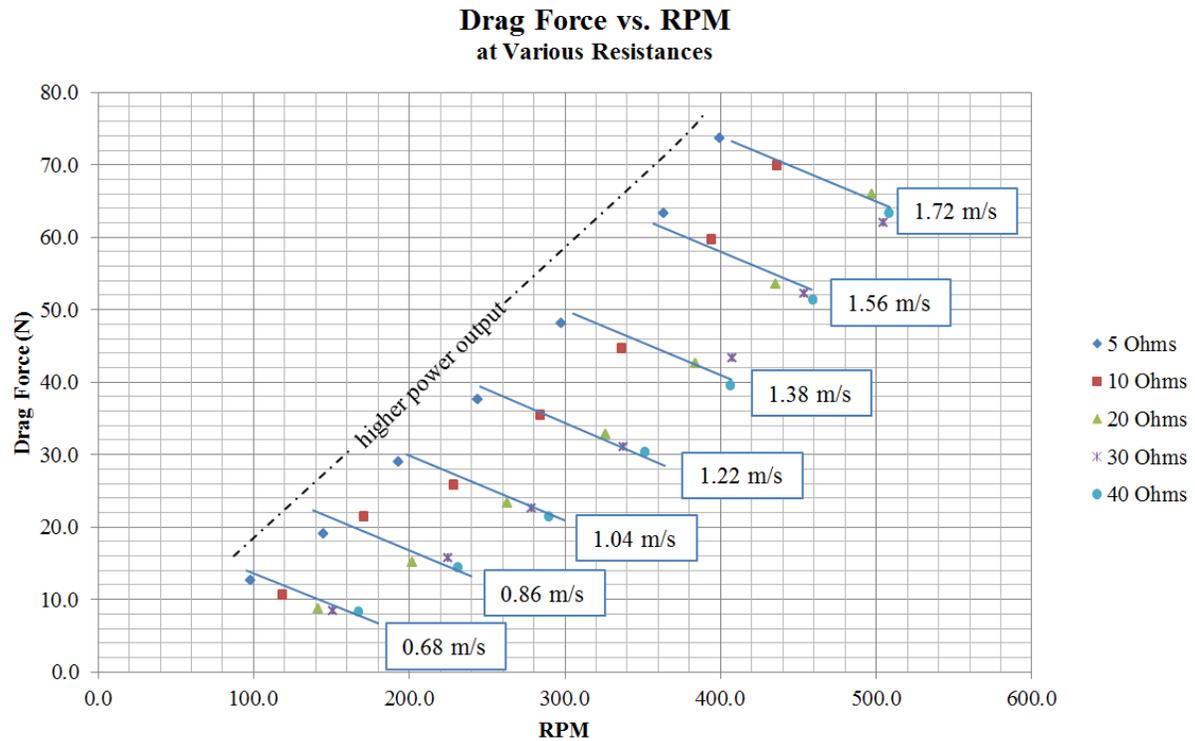


Figure 47.    Relationship between fluid velocity, drag force and rotational speed at various resistances.

### c.    *Comparison with Published Data*

To further validate our results, the experimental data was compared with the data provided by the manufacturer of the AFHT. In order to analyze the data we received from the manufacturer, we first identified major differences in mounting configuration and system assembly. The manufacturer provided detailed configuration preferences for the depth and mounting of their turbine [12]. However, due to the limited depth of the tow tank, the 1-meter-long mounting pole designed to support the turbine

below a vessel's hull was cut in half.  Additionally, we did not use the generator voltage output to charge a battery; rather we connected the generator output to resistors and a voltage measuring device.

(1)      Mounting Pole Discussion

The 4.5 cm-diameter aluminum pole used to mount the AFHT to the tow tank carriage had a wetted sting area of approximately 20 cm for our experiment (shorter than the recommended depth of approximately 50 - 60 cm).  Figure 48 was provided by hydroturbine's manufacturer.
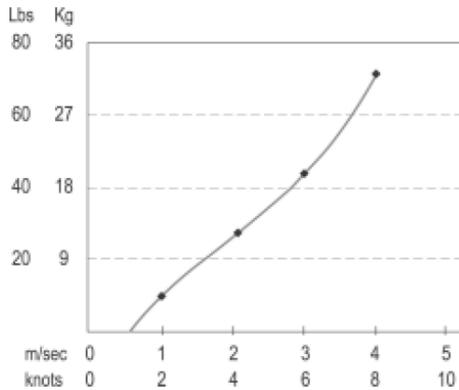


Figure 48.    Published mounting force data for AFHT. From [12].

The use of "Lbs." and "Kg" on the y-axis was assumed to be lbs-force (lbf) and Kg-force (kgf), so a conversion factor of 9.81 N/kgf was used to convert this axis to units of Newton.  Furthermore, of note, the provided data would suggest drag forces of 0 N for speeds less than 0.5 m/s.  The manual for this turbine assumes that the user will not place the turbine in the water until such speeds are reached that are more suitable for power production (greater than 1.0 m/s).

In order to determine the drag forces experienced by the sting at a depth of approximately 0.6 meters, we first had to determine the best approximation for the sting's drag coefficient.  Essentially, we reverse engineered their data (which included the drag forces due to both the turbine and the mounting pole) to ultimately compare those data points with our experimentally determined values.

64

In Figure 5.3 from [11], Frank White shows the boundary layer transition for an infinitely long cylinder occurring between a Re of $10^5$ and $10^6$, with a constant $C_D$ value of approximately 1.2 between $10^4$ and $10^5$ prior to that transition. Considering the effects of Reynolds number on our previous models through this transitional boundary layer, we first determined the range of Re for our pole from 0.508 m/s to 1.716 m/s and found that our values were just entering the transitional region.

| $U_\infty$ (m/s) | Re |
|---|---|
| 0.508 | 2.28E+04 |
| 0.693 | 3.10E+04 |
| 0.869 | 3.89E+04 |
| 1.042 | 4.67E+04 |
| 1.210 | 5.42E+04 |
| 1.372 | 6.15E+04 |
| 1.550 | 6.95E+04 |
| 1.716 | 7.69E+04 |
| $D = 0.045$ m | |
| $\nu = 1.004 \times 10^{-6}$ | |

Table 20.    Reynolds number approximations for mounting pole of infinite length.

Outside of the transitional boundary layer region, we could use Table 7.3 from [11] to estimate the $C_D$ value for the mounting pole in a 3-D fluid flow. With a length of 0.6 meters and diameter of 0.045 m, a $C_D$ value of 0.85 was interpolated. The estimated drag forces due to the mounting pole depth of 0.4 meters (the difference between the manufacturer's 0.6 meters and our actual experimental sting length of 0.2 meters) could then be used as a better comparison to our data. The results are graphed below in Figure 49.

**Drag Force Comparison with Experimental Data and Published Data**
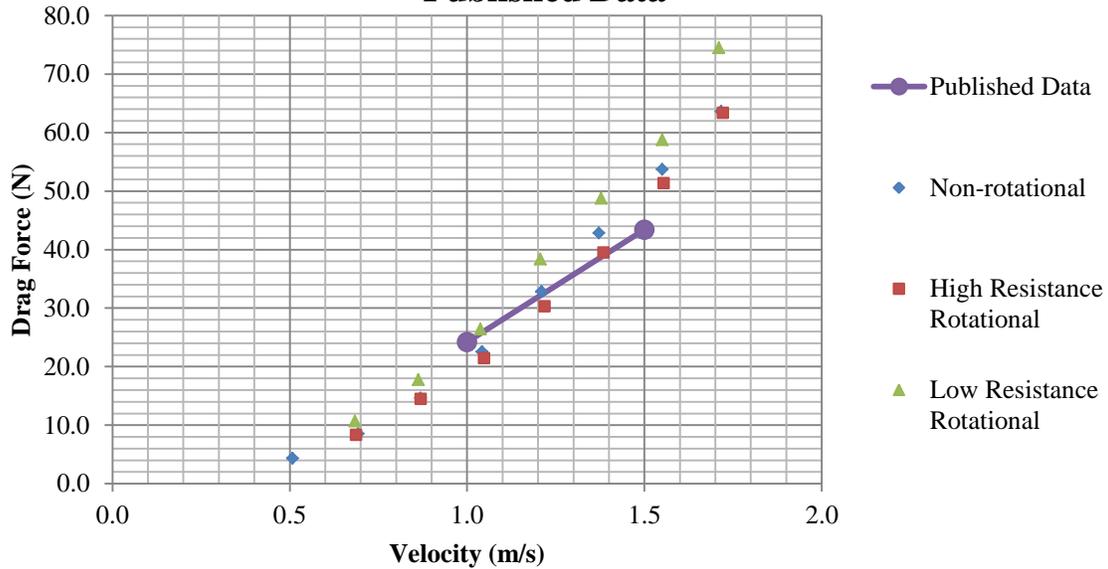


Figure 49.    Comparison between experimental and published data
for drag force vs. velocity.

### (2)    Power Production Discussion

The data provided by the manufacturer also mentions that at speeds less than 1 m/s, little output is obtained.  This immediately places nearly one third of our experimental data into their published region of uncertainty with regards to power output.  Additionally, there is a degree of unknown resistance in the manufacturer's wiring scheme from the generator to the batteries.  Since electric resistance was accounted for in our power measurements, and the manufacturer does not discuss the electric resistance associated with charging their batteries, we assumed negligible resistance in their model and subsequently expected slightly higher values for their reported power outputs as compared to our system (recall from Figure 40, as electric resistance increased in our circuit, overall power output decreased).  Figure 50 shows a comparison between our experimental data and the data provided by the manufacturer.

## Comparison of Experimental and CFD Results for Power Output
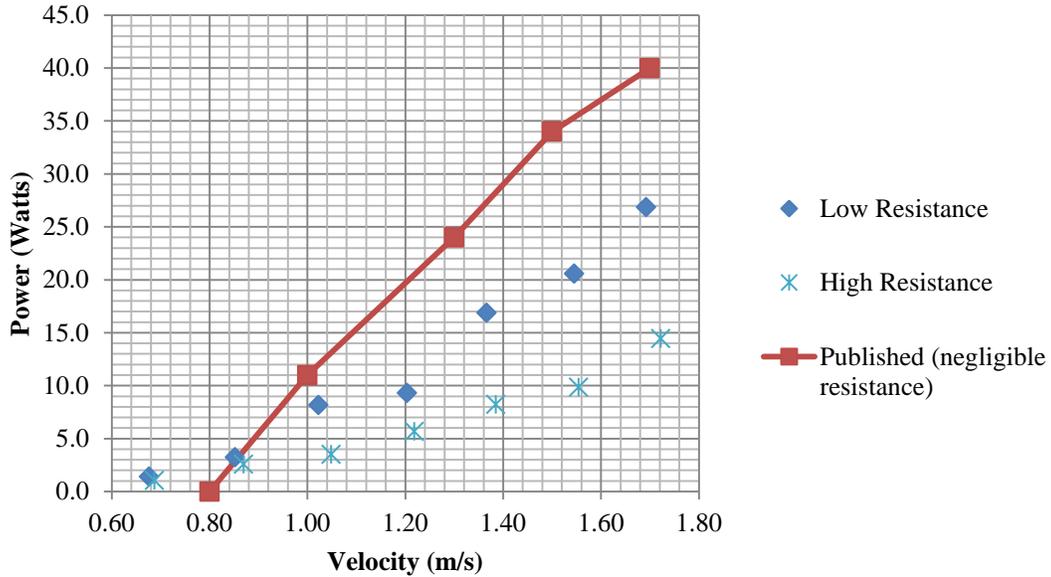


Figure 50.    Comparison between experimental and published data
for power output vs. velocity.

Several sources of error come to mind when looking at this graphical comparison.  As previously discussed, the power output expectations for the power turbine at low speeds is erratic at best.  The generator did in fact produce power at low rotational speeds, but the output peak values fluctuated a great deal.  It was from this data that we found our power averages for analysis.  Additionally, the difference in circuit resistance cannot be ignored.  Without plugging our turbine into a power- charging grid as described by the manufacturer, we can only come close to the full power production capabilities of a turbine with negligible resistance.  Finally, the region of experimental uncertainty grew for our data at higher speeds as our steady state data collection region contracted as velocity increased.  Ultimately, the turbine's full power production capability was only briefly explored during this research as our chief concern was the turbine's drag characteristics.

THIS PAGE INTENTIONALLY LEFT BLANK

# III. COMPUTATIONAL FLUID DYNAMIC APPROACH

The main objective of this thesis was to investigate the drag forces experienced by an AFHT inside a known control volume. Limited by the carriage speeds available for experimentation (2.0 m/s was determined to be the maximum operating velocity for safe operations in the tow tank) as well by our ability to accurately simulate open-water conditions, our concept would ultimately involve both experimental as well as computational methods for validation. If the CFD method validates our experimental, and vice versa, then the control volume could be redesigned to model an open-ocean environment. Higher speed simulations could also be conducted with CFD as a way to estimate drag at speeds above those available in a tow tank.

## A. THE CONTROL VOLUME (TOW TANK)

Though it would be important to eventually simulate open-water conditions for the AFHT, initial validation of our experimental results would require a computationally-modeled control volume (CV) as close to our laboratory model as possible, meaning that our modeled CV would have the same dimensions and fluid properties as our laboratory tow tank. Additionally, the placement of our computational models within the cross section of the tank would need to be in approximately the same location as our actual models in order to best capture any hydrodynamic activities that occur at or near our CV's boundaries.

Considering only the steady state portion of our tank trials for analysis, the movement of our model through the central section of our tank would ultimately be the area of focus for our simulation. A three-meter-long tank was built in SolidWorks with an opening on top and an inlet and outlet on either end. Through this CV, a constant fluid flow velocity would be modeled, ultimately neglecting any acceleration and deceleration zones present in the actual tank trials.

### 1. Boundary Conditions

Once the SolidWork's CV model was imported into AnsysWorkbench 14.0, fluid

properties for fresh water at 25°C were inputted into the system with the following fluid model parameters:

### a.     Fluid Parameters

Table 21.     Fluid model parameters for tow tank in CFD analysis.

| Tab | Setting | Value |
|---|---|---|
| Basic Settings | Location and Type > Location | B10927 |
| | Fluid and Particle Definitions | Fluid 1 |
| | Fluid and Particle Definitions > Fluid 1 > Material | Water |
| | Domain Models > Pressure > Reference Pressure | 1 [atm] |
| Fluid Models | Heat Transfer > Option | Isothermal |
| | Heat Transfer > Fluid Temperature | 25 [C] |
| | Turbulence > Option | Shear Stress Transport |

### b.     Inlet Boundary

Because fluid flow across the leading edge of the flat plate and the rotor blades experienced significant boundary layer separation, modeling turbulence in the inlet flow regime was unimportant, as it ultimately would not change the results significantly regardless what turbulence regime was selected (low, medium, or high intensity, or k and Eddy Viscosity Ratio) [19].

Table 22 represents the inlet boundary conditions for a computational trial on the non-rotational, full turbine configuration at 1.7 m/s using the k and Eddy Viscosity Ratio turbulence model.

Table 22.    Example for Inlet boundary conditions for non-rotational, full turbine configuration, 1.7 m/s, k and Eddy Viscosity Ratio turbulence model.

| Tab | Setting | Value |
|---|---|---|
| Basic Settings | Boundary Type | Inlet |
| | Location | Inlet |
| Boundary Details | Flow Regime > Option | Subsonic |
| | Mass and Momentum > Option | Cart. Vel. Components |
| | U | -1.7 [m s^-1] |
| | V | 0 [m s^-1] |
| | W | 0 [m s^-1] |
| | Turbulence > Option | k and Eddy Viscosity Ratio |
| | Turbulence > Kinetic Energy | 0.1 [m^2 s^-2] |
| | Turbulence > Eddy Viscosity Ratio | 10. |

### c.    Outlet Boundary

Table 23.    Outlet boundary conditions for CV.

| Tab | Setting | Value |
|---|---|---|
| Basic Settings | Boundary Type | Outlet |
| | Location | Outlet |
| Boundary Details | Mass and Momentum > Option | Static Pressure |
| | Mass and Momentum > Relative Pressure | 0 [Pa] |

### d.    Opening/Top Boundary

Table 24.    Opening/Top boundary conditions for CV as recommended by [19].

| Tab | Setting | Value |
|---|---|---|
| Basic Settings | Boundary Type | Opening |
| | Location | Top |
| Boundary Details | Flow Regime > Option | Subsonic |
| | Mass and Momentum > Option | Entrainment |
| | Relative Pressure | 0 [Pa] |
| | Turbulence > Option | Zero Gradient [19] |

### e.    Tank Walls Boundary

Table 25.    Tank wall boundary conditions for CV.

| Tab | Setting | Value |
|---|---|---|
| Basic Settings | Boundary Type | Wall |
| | Location | Wall1,Wall2,Bottom |
| Boundary Details | Mass And Momentum > Option | No Slip Wall |
| | Wall Roughness > Option | Smooth Wall |

Figure 51 shows a screen shot from CFX-Pre within the Ansys program for the boundary conditions described above.
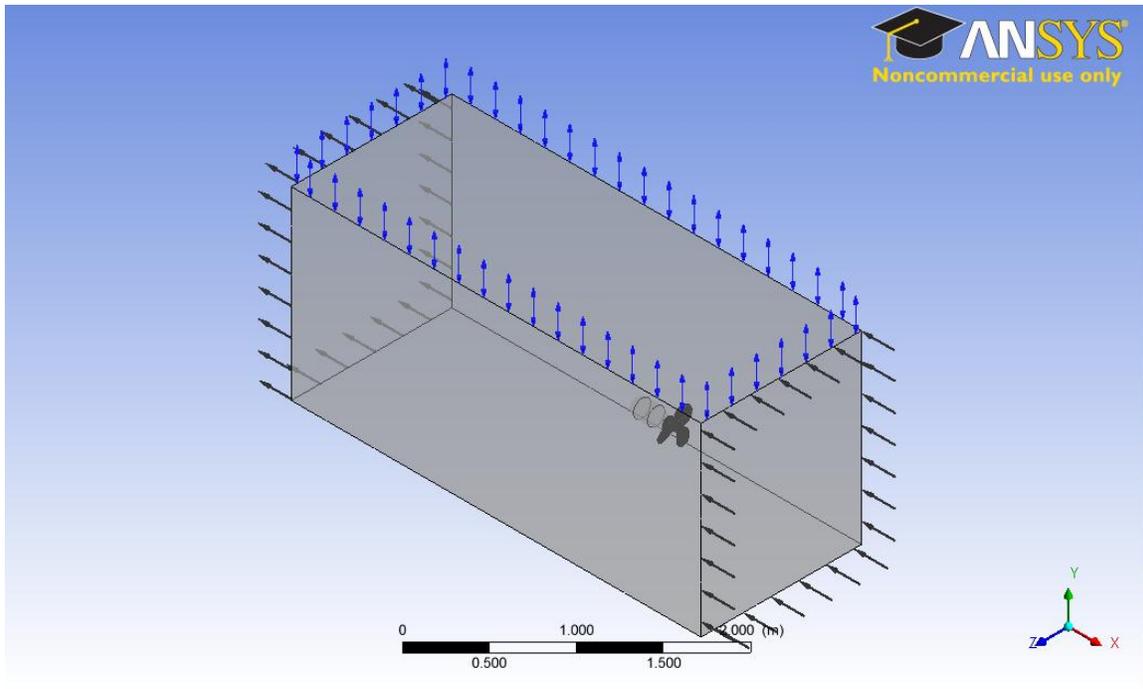


Figure 51.    CFX-Pre display of boundary conditions for control volume.

## B.    FLAT PLATE MODEL

For the CFD analysis on the flat plate model, all boundary conditions were maintained to the specifications described above for the tow tank CV.  Turbulence modeling was selected with the assumption that the boundary layer separation observed at the leading edge of the plates would negate any computed changes to the drag force in

our analytical trials. Any differences in drag force computation would likely fall within our region of uncertainty for our experimental trial.

The dimensions for Plate A were used to model our plate within SolidWorks. Once imported into our CFD CV in Ansys, the boundary conditions for our flat plate were designated as follows:

Table 26.    Turbine wall boundary conditions.

| Tab | Setting | Value |
|---|---|---|
| Basic Settings | Boundary Type | Wall |
| | Location | FullTurbine |
| Boundary Details | Mass And Momentum > Option | No Slip Wall |
| | Wall Roughness > Option | Smooth Wall |

The fluid flow regime was then set up to model the flat plate encountering a fluid flow similar to the flow implemented in our tow tank (0.5 to 1.7 m/s). A screenshot from CFX-Post is provided in Figure 52 for a fluid flow of 1.7 m/s with resultant velocity vectors shown around the flat plate.
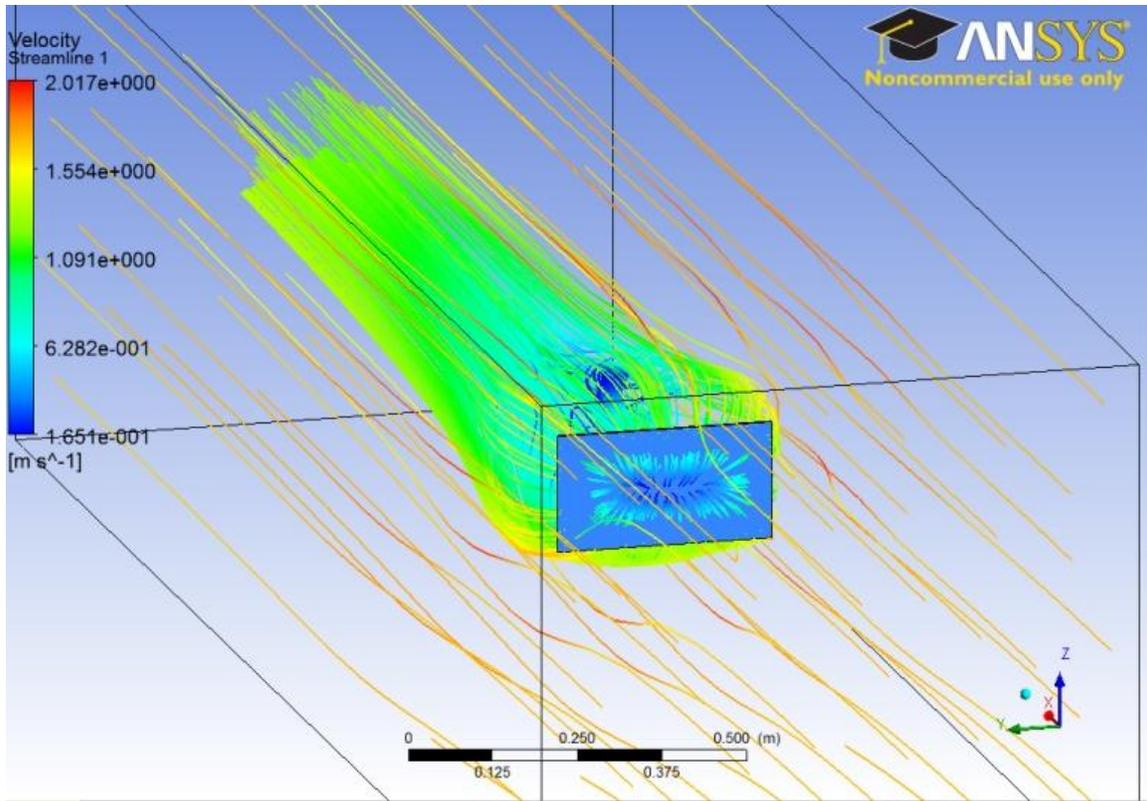
Figure 52.    CFX-Post results for flat plate A in 1.7 m/s fluid flow within Ansys.

Across the range of velocities, the CFD model resulted in data points similar to those acquired in the actual tow tank.  With an average deviation from the experimental values of less than 14.6%, the computational model proved to be relatively close to the experimental model.

Table 27.    Drag coefficient data from CFD analysis and exp. Flat Plate A data.

| $U_\infty$ (m/s) | CFD $C_D$ | Exp. $C_D$ |
|---|---|---|
| 0.50 | 1.198 | 0.472 |
| 0.68 | 1.203 | 0.753 |
| 0.85 | 1.199 | 0.974 |
| 1.01 | 1.199 | 1.154 |
| 1.18 | 1.201 | 1.239 |
| 1.34 | 1.215 | 1.260 |
| 1.49 | 1.228 | 1.317 |
| 1.63 | 1.220 | 1.287 |
| Average $C_D$ | 1.208 | 1.057 |
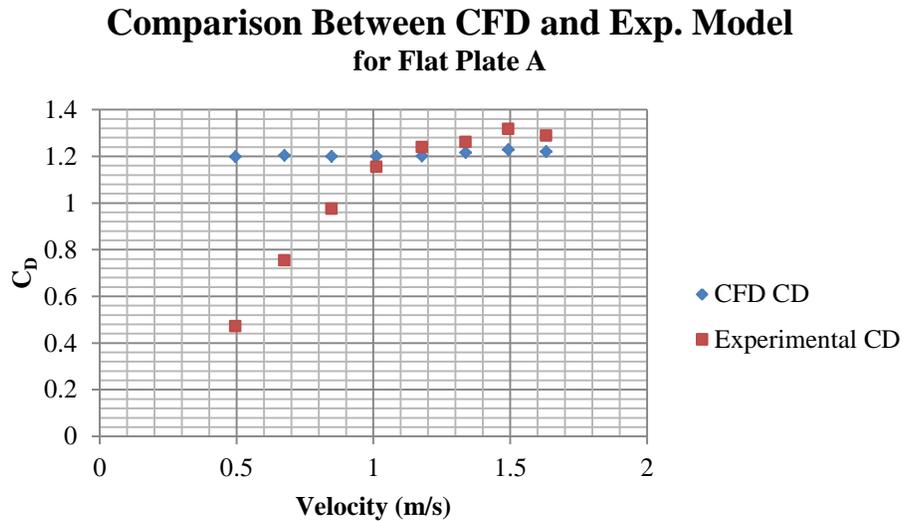


Figure 53.    Comparison between CFD and experimental drag coefficients
or flat plate A.

A correlation can be seen yet again in Figure 53 with the experimental data's consistency between the ranges of 1.0 m/s and 1.5 m/s, which falls within the region of reduced uncertainty.   Within this range, the CFD and experimental results appear to match up more precisely.

With a computationally calculated drag coefficient of approximately 1.208 compared to the literature value of 1.17, we felt confident to proceed with our turbine modeling within the same CFD scheme.

## C.  FULL TURBINE MODEL

### 1.  3-D Scan of 3-Bladed Rotor

Rather than drawing up a CAD design for the rotor, we decided to use a 3-D scanner to capture our actual rotor design in an attempt to best approximate our computational model.  To do this, a NextEngine 3-D Scanner was used with software integration into ScanStudio's HD PRO and RapidWorks 3.5.  Eventually, the scan was exported our part into SolidWorks 2012 and AnsysWorkbench 14.0 for CFD analysis.

Prior to scanning the 3-bladed rotor, a thin coat of white paint was used to minimize laser reflection during the scans.  The original face of the rotor was a smooth black powder-coated surface, which was nearly impossible to scan.  The NextEngine software was able to scan the rotor from 16 different angles at high definition.  Once these scans were completed, RapidWorks 3.5 was used to mesh the individual scans into a single part file.  This final part required a significant amount of computational resources to mesh the individual scans and smooth the data (a CPU with 4 quad-core, 2.6 GHz processors with 96 GB of RAM was used to complete the scan and mesh prior to exporting the data into SolidWorks).
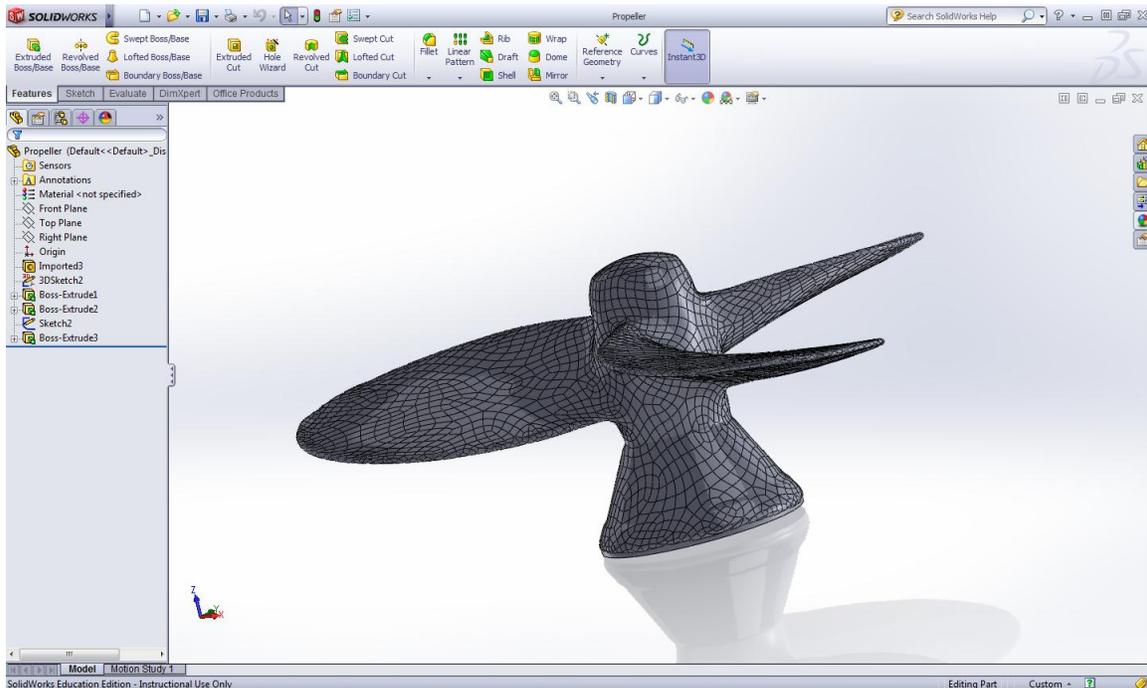
Figure 54.    Screen capture of imported rotor from 3-D scanner into SolidWorks.

## 2.    Processing the 3-D Scan

Once the part was imported into SolidWorks, the rotor contained over 8,000 individual surfaces.    Rather than utilizing SolidWork's feature recognition, those individual surfaces were kept in their original position to maintain the rotor's true dimensions and imperfections once imported into Ansys.  The generator was then drawn within SolidWorks and assembled to the rotor as a single part which was then exported as a parasolid part file (*.x_t) for use in Ansys.
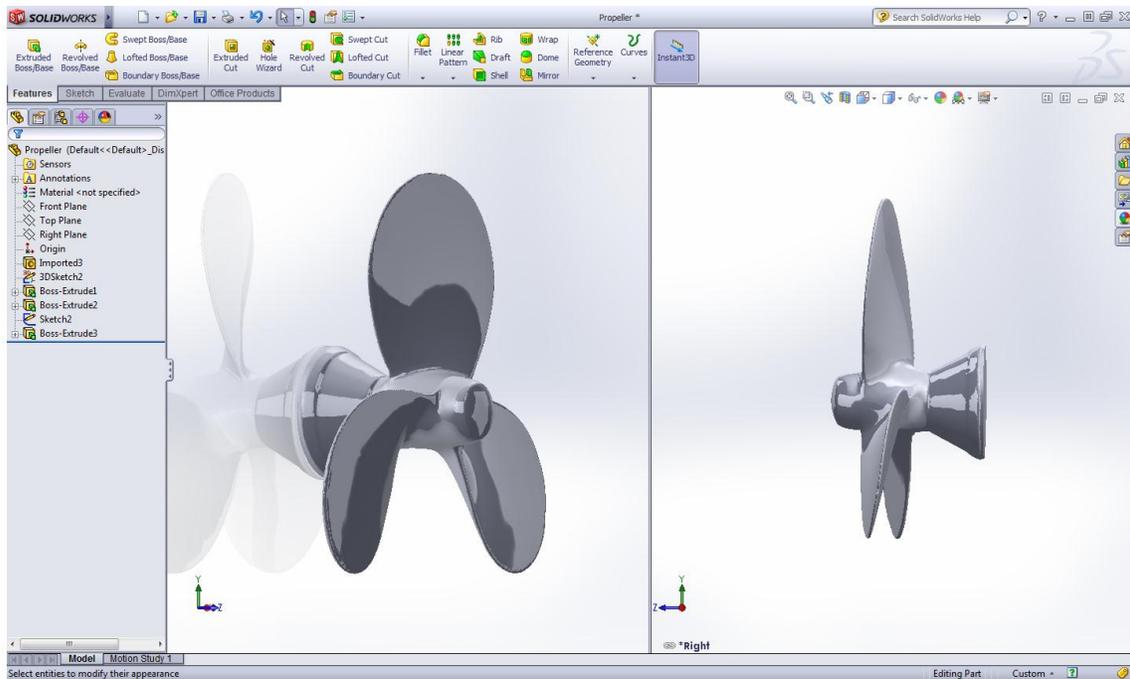


Figure 55.    Final rotor design prior to assembly to generator part in SolidWorks.
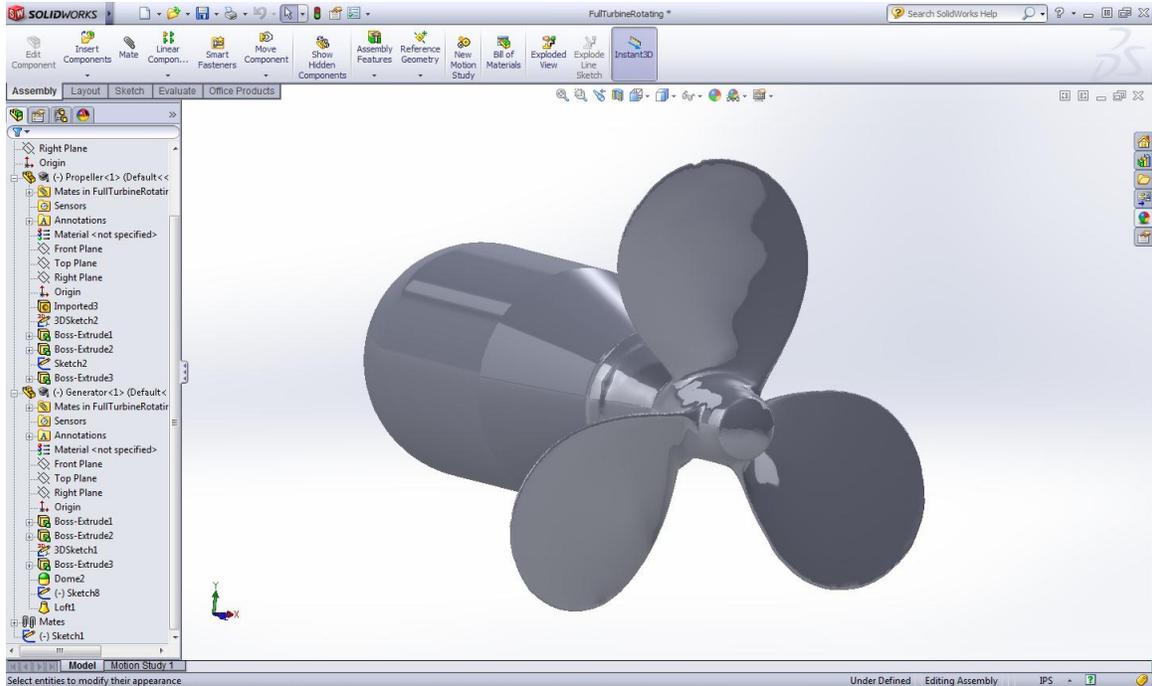
Figure 56.     Screen capture of assembled design prior to importing into Ansys.

The same tow tank structural design was pulled in from the CFD analysis of the flat plate with the full turbine parasolid imported into that geometry as a material cut-out.

### 3.     CFX Solver Parameters

#### a.     *Meshing Parameters*

In order to generate a highly detailed mesh for the full turbine geometry, the parameters outlined in Appendix A were used (note the use of a small angle for "Curvature Normal Angle" of $5^o$ as well as the use of a fine mesh for the "Relevance Center" of the mesh sizing).  The generated a mesh for the full turbine model with nearly one million nodes (995,266) with over five million elements (5,445,481).  Figures 57 and 58 show a visual of the mesh.
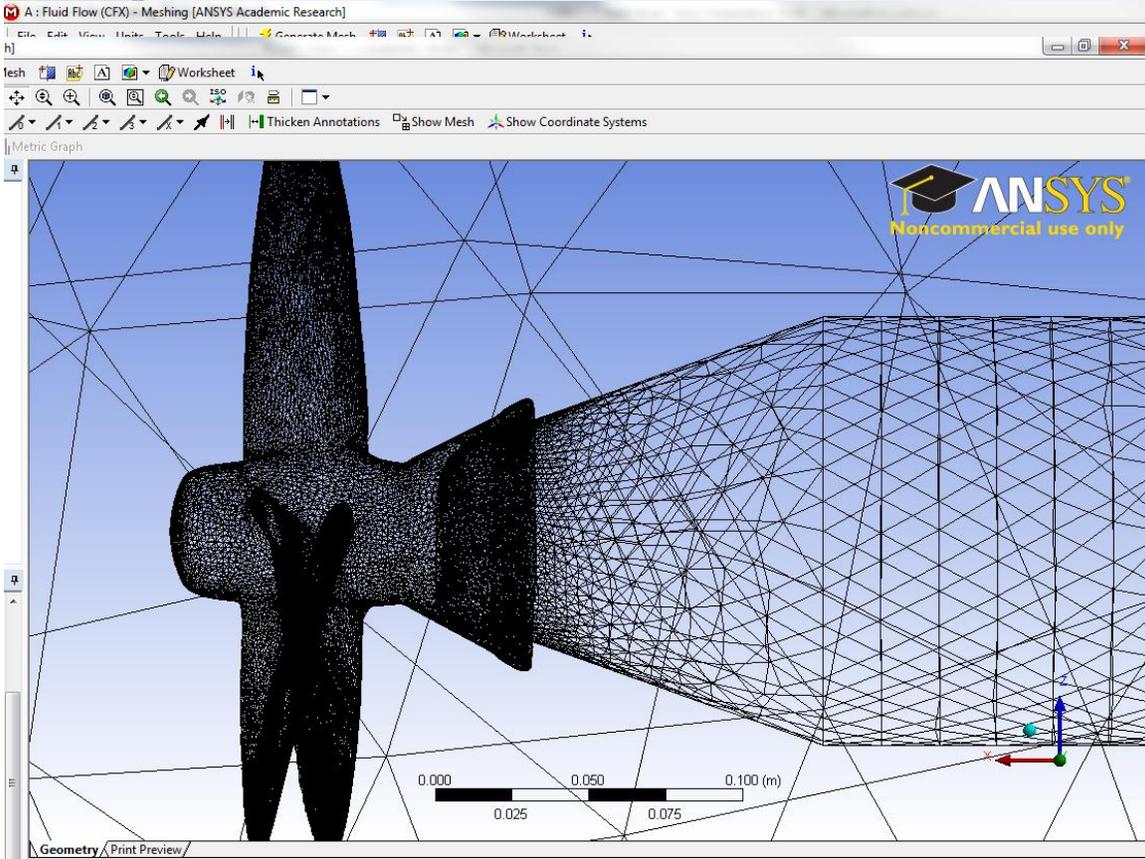
Figure 57.    Screen capture of generated mesh for full turbine (side profile).
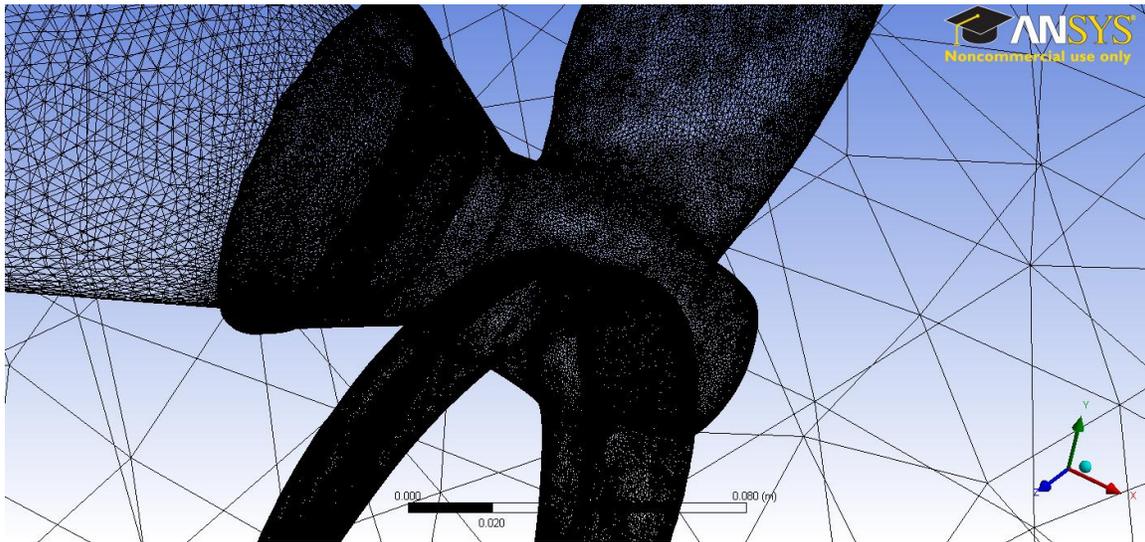


Figure 58.    Screen capture of full turbine (ISO profile) with generated mesh.

### b.      *Turbulence Modeling*

Three-dimensional CFD simulations typically employ Reynolds-averaged Navier-Stokes (RANS) turbulence models for marine propellers, which assume a fully-turbulent flow around the propeller.  Though turbulence transition has been recognized as a key factor directly associated with viscous effects of propeller flows, such as boundary layer development, scale effects, and tip and hub vortices [20], for the purposes of this CFD analysis the k-epsilon and Eddy Viscosity Ratio turbulence models were selected. We were able to simplify our turbulence computations in this way because the CFX Solver was ultimately analyzing a non-rotational model with assumed boundary layer separation at the blade tips.  Prior to the selection of this turbulence model, several other models were used within the CFX Solver that included low (1%), medium (5%) and high (10%) turbulence modeling as well as zero gradient, k epsilon, and k & eddy viscosity ratio turbulence models.  A summary of the results are listed in Appendix B.  For all CFD analyses, the fluid was modeled using SST (Shear Stress Transport) turbulence modeling as shown in Table 21.  This type of turbulence modeling for the CV has been recognized as the best model for approximations within boundary layers that are not quite fully turbulent [20].

The obvious outliers to this data are the models that used the k-epsilon model with values above 0.1 $\mathrm{m}^2/\mathrm{s}^2$ for $k$ and 0.1 $\mathrm{m}^2/\mathrm{s}^3$ for $\varepsilon$.  All of the other turbulence models produced nearly the same results for the drag force (with 7.8% standard deviation).  Those values are compared to the experimentally obtained values in the next section.

## D.      CFD RESULTS FOR NON-ROTATIONAL TURBINE

Though a significant amount of information can be obtained by a single CFD trial, the most sought-after data points were those of the model's total resultant force computed in the x-direction (the axis of rotation for the turbine and direction of carriages advance), and the visual confirmation of boundary layer separation at the leading edge of the rotor's blades (with subsequent vortices and pressure gradients behind the blades).

Data comparing the non-rotational turbine CFD model with experimental results are shown below.

## Comparison of Experimental and CFD Results
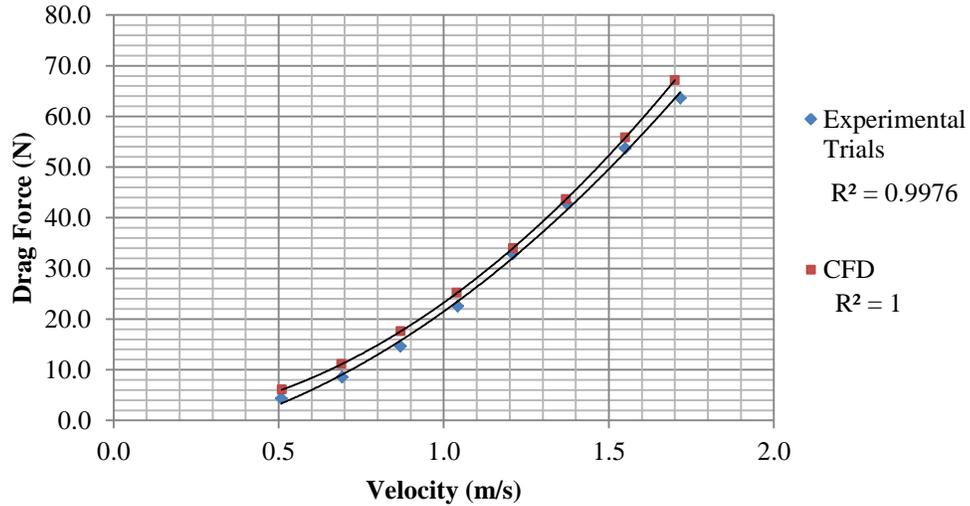


Figure 59.    Comparison of experimental and CFD drag force results for non-rotational turbine configuration.

Of note, the difference in drag force values appear small (Figure 59), but the degree of difference is enough to result in a greater separation between experimental and CFD results (tabulated below and shown in Figure 60).

Table 28.    Comparison between experimental and CFD drag force results.

| Experimental Drag Force (N) | CFD Drag Force (N) | % difference |
|---|---|---|
| 4.32 | 6.06 | 28.7 |
| 8.55 | 11.09 | 22.9 |
| 14.60 | 17.59 | 17.0 |
| 22.53 | 25.16 | 10.4 |
| 32.83 | 33.99 | 3.4 |
| 42.85 | 43.62 | 1.8 |
| 53.68 | 55.81 | 3.8 |
| 63.59 | 67.13 | 5.3 |

Since we subtracted the drag force values of the carriage alone from the total measured drag forces across all measured speeds, any measuring error present at lower speeds will be significantly magnified, hence higher percent difference between experimental and computational results in that range.

**Comparison of Experimental and CFD Drag Coefficients**
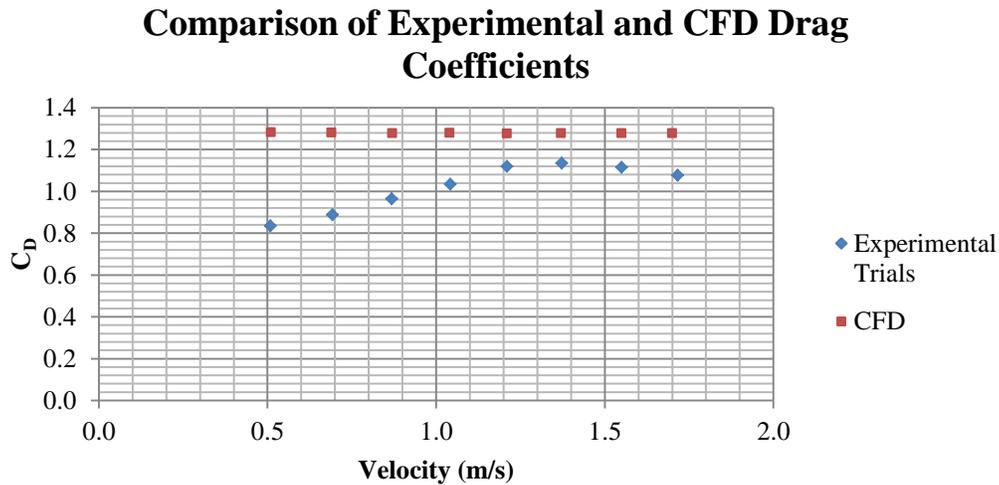


Figure 60.    Comparison of experimental and CFD drag coefficient results for non-rotational turbine configuration.

A correlation can be seen yet again with the experimental data's consistency within the region of reduced uncertainty.  For the upper range velocity values, the CFD and experimental results are more closely related.

As far as visual evidence of boundary layer separation and formation of vortices at the leading edge of the rotor blades, the following image was produced with velocity vectors initiated from the full surface of the turbine (rotor and generator).  These vectors show the vortices behind the blades as well as fluid flow swirl aft of the generator (shown in Figure 61).
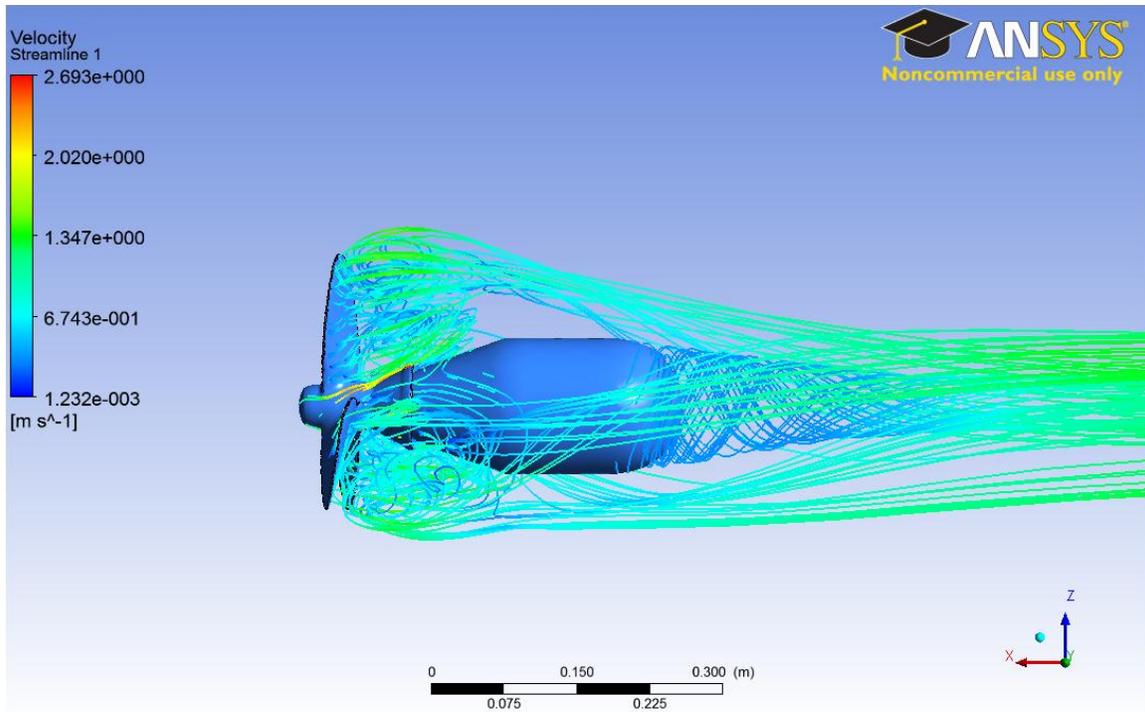
Figure 61.    Screen capture of CFD computation of full turbine at 1.7 m/s.

THIS PAGE INTENTIONALLY LEFT BLANK

# IV. DISCUSSION OF EXPERIMENTAL AND COMPUTATIONAL RESULTS

## A. SUMMARY OF DRAG FORCE RESULTS

The experimental results shown in Figure 62 indicate a reasonable trend in drag force data for all of tow tank models.
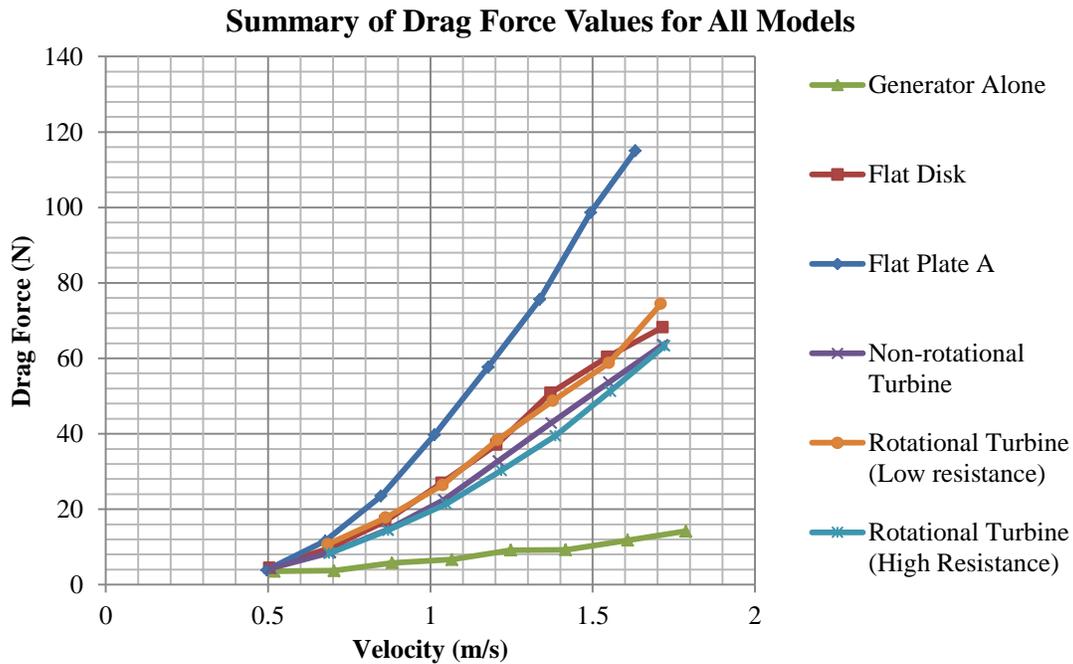


Figure 62.    Summary of drag force values.

$R^2$ values for all drag force data shown in Figure 62 exceeded expectations when fit to a quadratic trendline, with the lowest $R^2$ value of 0.9706 for the sled alone data. Since the relationship between fluid velocity and drag force is quadratic as per Eqn. 1.

The results of fluid flow separation behind the blades as it interacts with the generator are shown in Figure 63.  This effect is not observable visually with experimentation.  However, with CFD, a component force computation for our full turbine (with non-rotating blades) shows the resultant force at its greatest value against the direction of the turbine (negative values) on the aft, curved surface of the generator

casing. Negative values in the x-direction indicate drag forces. The positive direction along the x-axis (to the right in Figure 63) indicates the direction that the turbine would be moving if the fluid were stationary. The inputted velocities for these computations were negative in the x-direction at the inlet.
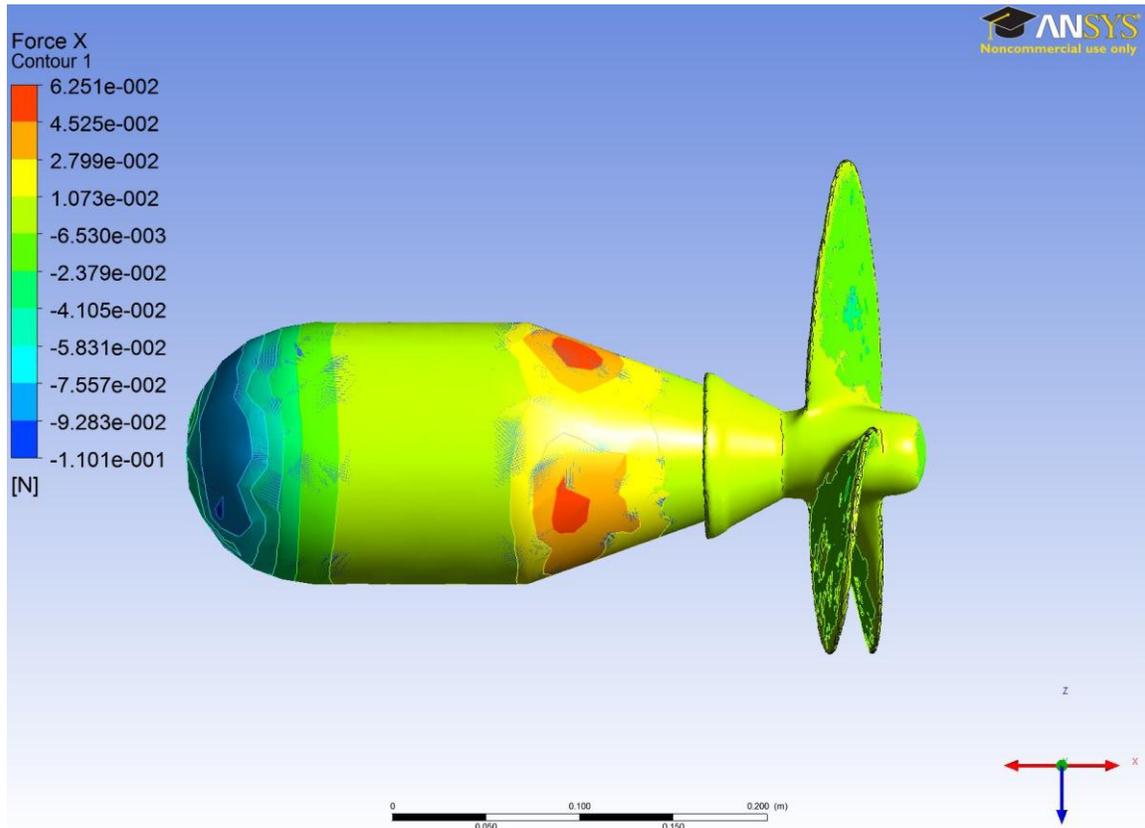


Figure 63.    Visual representation of force contour lines on full turbine.

## B.    SUMMARY OF DRAG COEFFICIENT CALCULATIONS

Literature values for drag coefficients were not readily available for 3-bladed, axial flow rotors, so our ability to compare our experimentally determined values with known values was not possible. Increased confidence in our procedures using various known experimental models, combined with basic level CFD analysis, allowed us to report a range of calculated drag coefficients that may prove useful for future work in tow tank research. Ultimately, the AFHT analyzed in this thesis could prove to be the best starting point for the Energy Ship Concept, either as a good representative sample for

axial-flow hydroturbines, or as a comparison with other turbine types. Knowing the power output available for this specific turbine, with the $C_P$ and $C_D$ values for different loading conditions, will allow us to assess the feasibility of utilization on a greater scale in the future, especially when more hydroturbines are examined. In summary, the $C_D$ value for this particular turbine, when operational, can reliably be reported at values between 0.4 and 0.8 as shown below in Figure 64.

**Summary of Experimental Drag Coefficient Data**
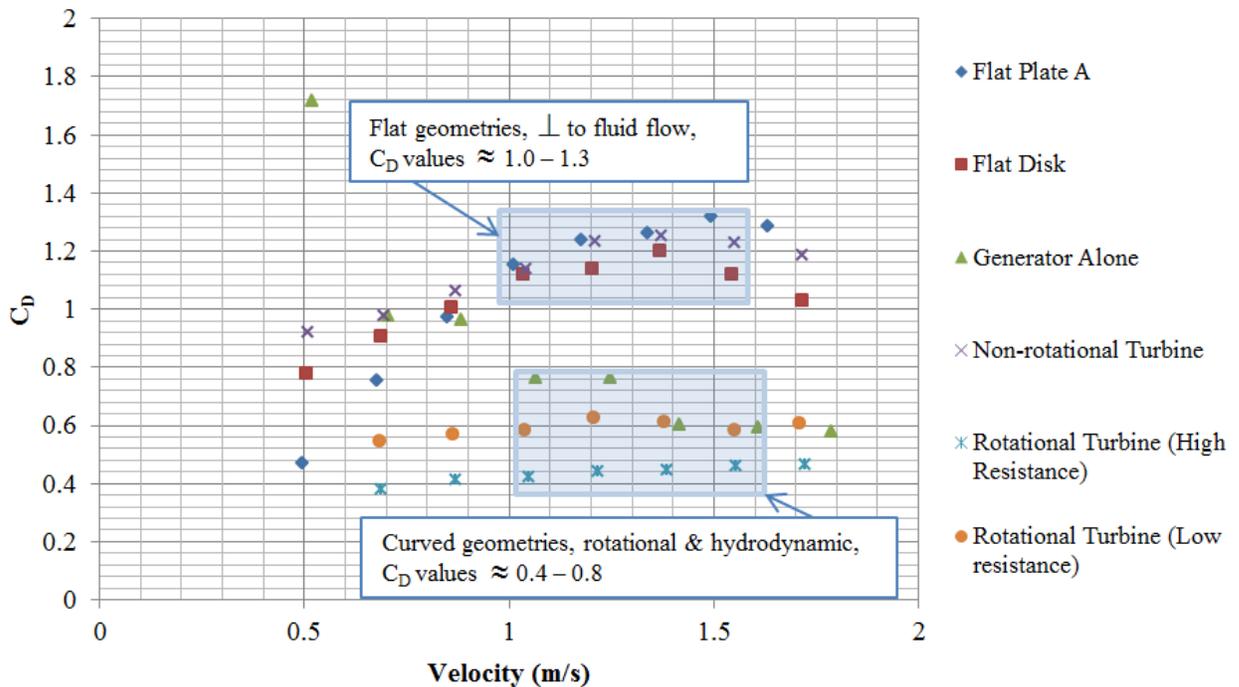


Figure 64.   Summary of experimental drag coefficient calculations.

Additionally, $C_P$ values (or turbine efficiencies) for this specific experimental setup between 0.068 and 0.2 resulted whilst providing nominal power output in the range of $7-27$ watts at speeds between 0.5 and 1.8 m/s respectively. Turbine efficiency can be expected to increase when electrical resistance is minimized, thus making battery charging and low-current operations entirely feasible, even at low speeds ($1.0-1.8$ m/s).

## C.    SOURCES OF ERROR

Below are a few discussed sources of error identified in our experiment:

### 1.    Inconsistent Carriage Drag Due to Rail Lubrication

The rail system of the NPS tow tank was lubricated at irregular intervals throughout the experimentation phase to ensure minimal drag forces were experienced as a result of rail-to-ball bearing friction.  The effects of not maintaining the lubrication of the system are shown below.
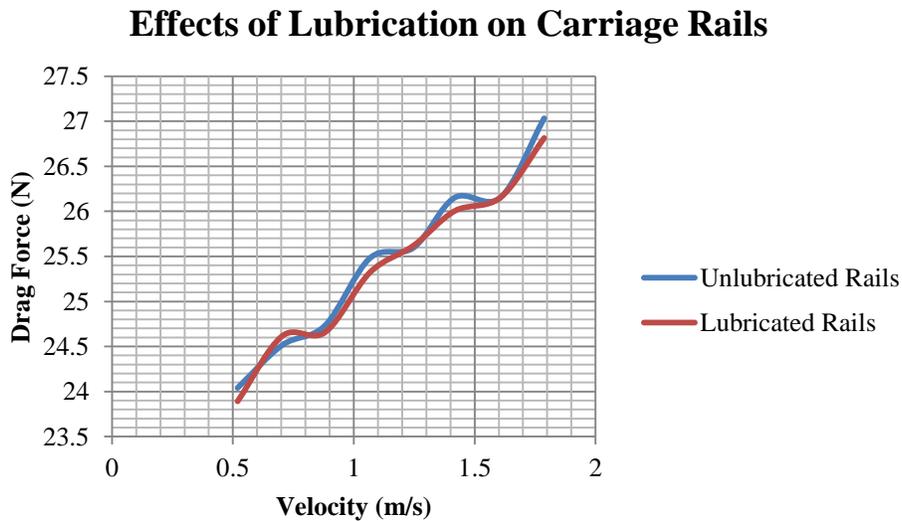


Figure 65.    Effects of rail lubrication.

Regular lubrication for any bearing system is highly recommended.  Though tedious at times, errors may have crept into the system along the way by not lubricating the rail system on a regular basis (or at least prior to commencing each trial).

### 2.    Inconsistent Motor Speeds Due to Minor Slippage of Belt and Pulley System

The graph below shows the fluctuation of velocity measurements with their respective motor controller command.  A consistent input command of 10 Hz did not always produce sled speeds at a consistent 1.7 m/s.  Depending on what was attached to

the carriage, the velocity values varied anywhere from 1.68 to 1.83 m/s. On several occasions, even with the exact same carriage loading, a 10 Hz motor speed resulted in different time periods for acceleration as a result of observed slippage of either the pulley chord or the motor belt attached to the pulley system.

**Carriage & Motor Speed Relationship**
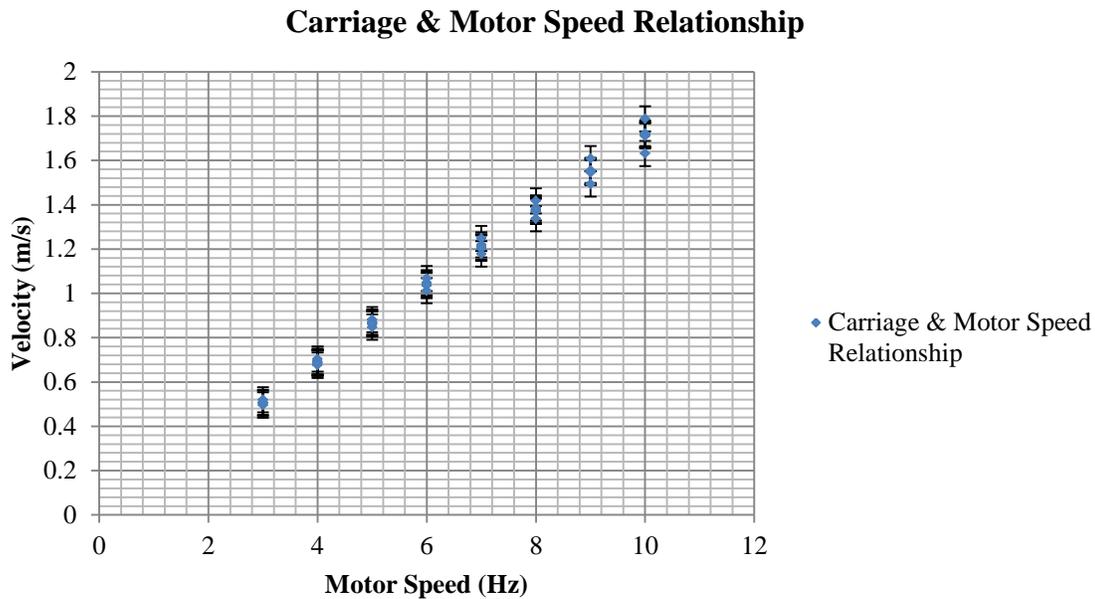


Figure 66.    Carriage speed and motor controller input relationship.

Though the velocity expectations were not important in the actual determination of the carriage speed (as this was measured with the high speed camera) the mere differences in velocities at similar motor frequencies shows a certain level of inconsistency with the speed of the carriage in general. The assumption has been made that the speed of the carriage was exactly that of the measured velocity for the entire duration of the steady state. This may not have been the case, however, if the carriage ultimately surged or lagged due to the inconsistency of the motor/pulley system even through the steady state.

**3.      Visual (Non-Arithmetic) Reduction of Load Cell Results**

As discussed in the Data Acquisition section of Chapter II (see Figure 7), the

means for determining steady state for any given set of load cell data was not perfectly reproducible. Without the use of computational software, the starting point and stopping point of the steady state portion of our load cell data was determined entirely using visual approximations. Though the inaccuracy associated with this type of data reduction is hard to quantify, it is in fact a source of error worth noting.

### 4.    Trial Velocities of AFHT Below Manufacturer's Recommendations

For normal operations, AmpAir recommends operating their turbine at speed above 1.0 m/s. Minimal, or inconsistent, power output is expected at speeds lower than this speed. With that in mind, any comparison of our data with the data provided by the manufacturer is informational at best (refer to Figures 48 through 50).

### 5.    Computational Turbulence Modeling

Literature review suggests that transition-sensitive turbulence models, as compared to fully turbulent flow simulations, are better able to resolve the strength of the tip vortices in turbine and rotor simulations and will likely benefit the prediction of blade-surface flows and corresponding force and moment calculations [20]. Transition-sensitive turbulence models, such as $k$-$\omega$ eddy-viscosity models, produce better results for computations of models within a transitional boundary layer for propellers and rotors.

### 6.    High Speed Camera Accuracy

Even at frame rates as high as 500 fps, the high speed camera was not able to capture the movement of a model's designated reference point perfectly. At higher speeds, this reference point would travel as far as 0.992 millimeters between two individual frames, thus introducing a very small degree of error in the calculations of the experimental velocities. When this uncertainty in the measured velocity is squared, the total error represented a deviation of less than 0.2 % to the calculated drag coefficients.

90

# V.    CONCLUSIONS AND RECOMMENDATIONS

## A.    CONCLUSION

There is an urgent need for innovative and efficient renewable energy technologies to offset dependence on fossil fuels and to mitigate global warming.  One possible way to do this is to bring ocean wind power back to land through Platzer's Energy Ship Concept.  Axial-flow hydrokinetic turbines are a great starting point for renewable energy solutions across a wide range of applications, including possible use onboard future energy ship designs.  An important requirement for the feasibility of this concept is the determination of the sail area required to overcome the total drag, consisting of the ship and the hydropower generator drag.  With the experimental and computational information presented in this paper, the determination of drag characteristics of at least one towed hydropower generator is now part of the discussion, as well as the methods and experimental procedures developed that can be used in future hydroturbine analyses.

The results for the drag forces experienced by the thin flat plates and the non-rotational turbine configuration showed predictable trends when viewed as functions of velocity, but as soon as the turbine was allowed to rotate, we confirmed that the drag forces measured were no longer merely a function of the fluid velocity, but also the rotational speed of the rotors and the magnitude of electric current produced as a result of that rotation.  The maximum power output recorded during all of our trials was 27.1 watts, which was recorded while traveling at 1.72 m/s through the water.  The electrical output of the generator, connected to a 10 Ohm resistor, allowed for a rotational speed of 439.89 RPMs.  In contrast, the highest rotational speed recorded during all of our trials was 508.57 RPMs, which occurred at a speed of 1.72 m/s.  Yet with 40 Ohms of resistance connected to the generator output, this run resulted in a power output of only 14.43 watts.

Between these two trials, the higher drag force recorded coincided with the higher recorded power output, yet with lower rotational speed.  The values for the drag and

power coefficients for the higher-power trials were consistently higher than those of the faster RPM trials. Hence, optimum efficiency occurs at a specific tip speed ratio for each loading condition.

## B. RECOMMENDATIONS FOR FUTURE RESEARCH

### 1. Open-Water Testing

Tow tank experiments are a good way to determine model characteristics that can later be used for open-water estimates through extrapolation; however, open-water testing is always the best way to acquire real-world data. In any open-water trials, the power production and drag measurements could be assessed at higher speeds (more agreeable speeds for the AFHT we investigated are between 2 and 10 m/s) as well as any impacts on a vessel's stability characteristics.

### 2. Evaluations of Additional Types of Turbines

There are numerous different types of hydropower turbine designs available for use both on sailing vessels as well as rivers and tidal basins. Each power turbine comes with its design characteristics that maximize structural durability, efficiency, cost, or net power production; however, very few manufacturers tout minimizing drag characteristics as a selling point. Several hydroturbine designs have been used in rivers and tidal estuaries where the effects of drag and turbulence matter as they pertain to sediment deposits and impact on marine environments, however, many of those designs have never been evaluated in tow (underneath or behind a sailing vessel).

Future research in this field should include analyses of multiple types of hydroturbines (trans-axial, or crossflow turbines, Darius wheels, Gorlov helical turbines, etc.) to determine which category of turbine is best at minimizing power efficiency whilst minimizing drag forces. An example of an entirely new approach to hydrodynamic power generation was Platzer and Sarigul-Klijn's analysis of an oscillating-foil power generator in [2], which drew attention to this type of power generator hoping to find advantages over hydro-turbines. The oscillating-foil power generator was based on the reciprocating rather than the rotary motion principle.

### 3. Variable Pitch Rotors or Composite-Transitional Blades

With the development of new composite materials, it may be possible to find a solution to undesirable pitch limitations experienced across a wide range of fluid velocities. Variable pitch propellers can be designed to optimize power extraction from different fluid velocities, but maintenance and part requirements are extensive for these types of propellers/rotors. A flexible or bendable rotor could potentially be designed with similar adaptability as a variable pitch rotor without the mechanical requirements. If the rotors could be reshaped into more hydrodynamic designs that are more optimally suited for higher-speed fluid flows, then it would be possible to reach higher RPMs without rotor replacement or reconfiguration requirements.

### 4. CFD for Rotating Blades

Finally, further work is required to best determine if CFD analysis is an accurate and reliable means of determining turbine drag characteristics. Ultimately, a rotating mesh would be a great starting point for future research as torsional effects on rotation and boundary layer separation may be key to better predicting performance characteristics of our turbine.

THIS PAGE INTENTIONALLY LEFT BLANK

# VI.   APPENDIX A

## A.   CORRELATION BETWEEN $C_P$ AND $C_D$

**Drag and Power Coefficient Correlations**
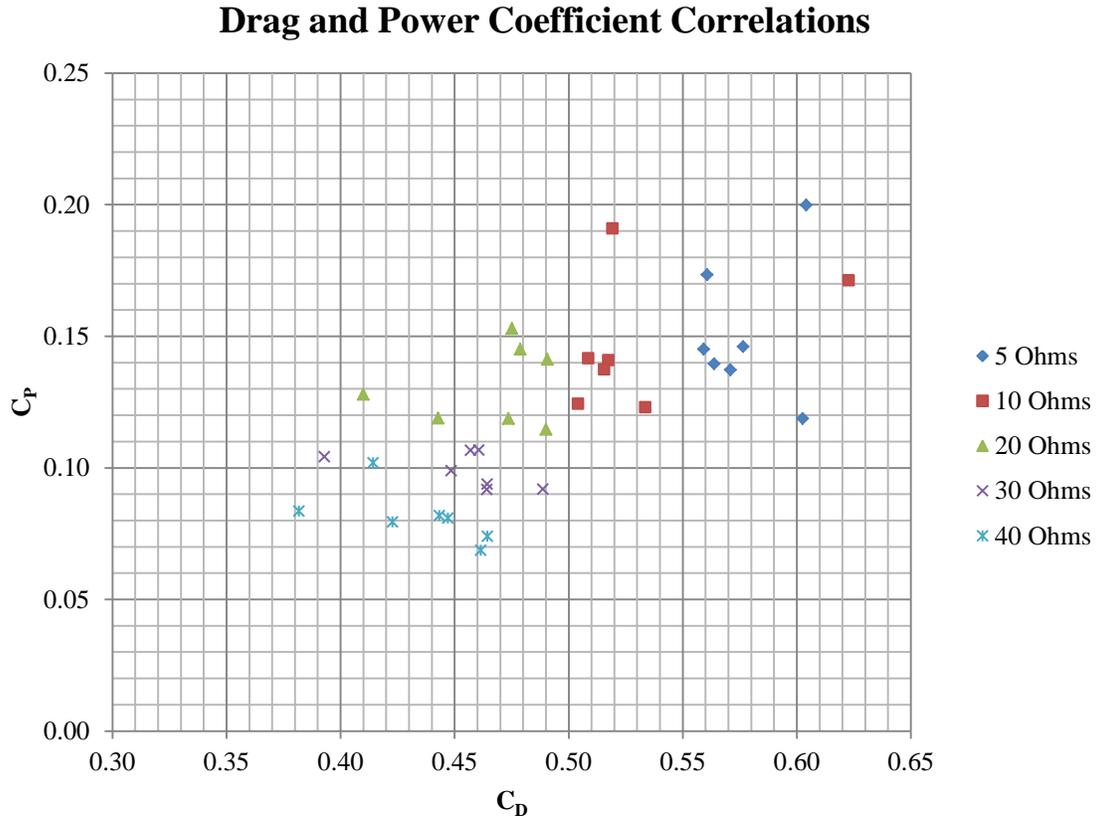


Figure 67.   Drag and power coefficient correlation at various resistances.

The graph in Figure 67 shows further non-dimensional analysis for the calculated drag coefficients and power coefficients.  Of note, the power coefficient, or turbine power efficiency, increases as the drag coefficient increases.  Subsequently, the highest values for the power coefficients occur at the lowest electric resistances.

## B. MESHING SUMMARY

Table 29.    Mesh data summary for full turbine in towing tank control volume.

| Details of "Mesh" | | |
|---|---|---|
| **Defaults** | | |
| Physics Preference | CFD | |
| Solver Preference | CFX | |
| ☐ Relevance | 0 | |
| **Sizing** | | |
| Use Advanced Size Function | On: Curvature | |
| Relevance Center | Fine | |
| Initial Size Seed | Active Assembly | |
| Smoothing | Medium | |
| Transition | Slow | |
| Span Angle Center | Fine | |
| ☐ Curvature Normal Angle | 5.0 ° | |
| ☐ Min Size | Default (5.6452e-004 m) | |
| ☐ Max Face Size | Default (5.6452e-002 m) | |
| ☐ Max Size | Default (0.11290 m) | |
| ☐ Growth Rate | Default (1.20 ) | |
| Minimum Edge Length | 1.2714e-004 m | |
| **Inflation** | | |
| Use Automatic Inflation | None | |
| Inflation Option | Smooth Transition | |
| ☐ Transition Ratio | 0.77 | |
| ☐ Maximum Layers | 5 | |
| ☐ Growth Rate | 1.2 | |
| Inflation Algorithm | Pre | |
| View Advanced Options | No | |
| **Patch Conforming Options** | | |
| Triangle Surface Mesher | Program Controlled | |
| **Advanced** | | |
| Shape Checking | CFD | |
| Element Midside Nodes | Dropped | |
| Straight Sided Elements | | |
| Number of Retries | 0 | |
| Extra Retries For Assembly | Yes | |
| Rigid Body Behavior | Dimensionally Reduced | |
| Mesh Morphing | Disabled | |
| **Defeaturing** | | |
| Pinch Tolerance | Default (5.0807e-004 m) | |
| Generate Pinch on Refresh | No | |
| Automatic Mesh Based Defeaturing | On | |
| ☐ Defeaturing Tolerance | Default (2.8226e-004 m) | |
| **Statistics** | | |
| ☐ Nodes | 995266 | |
| ☐ Elements | 5445481 | |
| Mesh Metric | None | |

## C. CFD TURBULENCE SUMMARY

Table 30.     Summary of turbulence model examination for CFD of non-rotating turbine configuration.

| Velocity (m/s) | Turbulence at Inlet | Turbulence on Top | Drag Force (N) | Area (m²) | $C_D$ |
|---|---|---|---|---|---|
| 1.7 | Low (Intensity = 1%) | Entrainment, Rel Pres 0 Pa, Zero Gradient, | 66.8962 | 0.03645 | 1.27264 |
| 1.7 | High (Intensity = 10%) | Entrainment, Rel Pres 0 Pa, Zero Gradient, | 67.2018 | 0.03645 | 1.278454 |
| 1.7 | Zero Gradient | Entrainment, Rel Pres 0 Pa, Zero Gradient, | 67.4 | 0.03645 | 1.282224 |
| 1.7 | Zero Gradient | Entrainment, Rel Pres 0 Pa, Zero Gradient, | 67.5007 | 0.03645 | 1.28414 |
| 1.7 | High (Intensity = 10%) | Opening Pres. And Dirn, Rel Pres 0 Pa, Zero Gradient | 67.2019 | 0.03645 | 1.278456 |
| 1.7 | k epsilon (k = 1 m^2 s^-2 , e = 1 m^2 s^-3) | Entrainment, Rel Pres 0 Pa, Zero Gradient | 111.374 | 0.03645 | 2.11879 |
| 1.7 | k epsilon (k = 0.1 m^2 s^-2 , e = 0.1 m^2 s^-3) | Entrainment, Rel Pres 0 Pa, Zero Gradient | 72.8307 | 0.03645 | 1.385538 |
| 1.7 | Default Intensity and Auto compute Length Scale | Entrainment, Rel Pres 0 Pa, Zero Gradient | 67.1324 | 0.03645 | 1.277133 |
| 1.7 | k and Eddy Viscosity Ratio, Turb. Kinetic Energy: 0.1 m^2 s^-2, Eddy Viscosity Ratio: 10 | k and Eddy Viscosity Ratio, Turb. Kinetic Energy: 0.1 m^2 s^-2, Eddy Viscosity Ratio: 10 | 67.13 | 0.03645 | 1.277088 |

Table 31.    Summary of turbulence models used for CFD of non-rotating turbine configuration.

| Velocity (m/s) | Turbulence at Inlet | Turbulence on Top | Drag Force (N) | Area (m$^2$) | $C_D$ |
|---|---|---|---|---|---|
| 1.7 | k and Eddy Viscosity Ratio, Turb. Kinetic Energy: 0.1 m^2 s^-2, Eddy Viscosity Ratio: 10 | Entrainment, Rel Pres 0 Pa, Zero Gradient | 67.13 | 0.03645 | 1.277088 |
| 1.55 | k and Eddy Viscosity Ratio, Turb. Kinetic Energy: 0.1 m^2 s^-2, Eddy Viscosity Ratio: 10 | Entrainment, Rel Pres 0 Pa, Zero Gradient | 55.8173 | 0.03645 | 1.277342 |
| 1.37 | k and Eddy Viscosity Ratio, Turb. Kinetic Energy: 0.1 m^2 s^-2, Eddy Viscosity Ratio: 10 | Entrainment, Rel Pres 0 Pa, Zero Gradient | 43.619 | 0.03645 | 1.277722 |
| 1.21 | k and Eddy Viscosity Ratio, Turb. Kinetic Energy: 0.1 m^2 s^-2, Eddy Viscosity Ratio: 10 | Entrainment, Rel Pres 0 Pa, Zero Gradient | 33.9855 | 0.03645 | 1.276218 |
| 1.04 | k and Eddy Viscosity Ratio, Turb. Kinetic Energy: 0.1 m^2 s^-2, Eddy Viscosity Ratio: 10 | Entrainment, Rel Pres 0 Pa, Zero Gradient | 25.156 | 0.03645 | 1.278724 |
| 0.87 | k and Eddy Viscosity Ratio, Turb. Kinetic Energy: 0.1 m^2 s^-2, Eddy Viscosity Ratio: 10 | Entrainment, Rel Pres 0 Pa, Zero Gradient | 17.5863 | 0.03645 | 1.277432 |
| 0.69 | k and Eddy Viscosity Ratio, Turb. Kinetic Energy: 0.1 m^2 s^-2, Eddy Viscosity Ratio: 10 | Entrainment, Rel Pres 0 Pa, Zero Gradient | 11.0875 | 0.03645 | 1.280376 |
| 0.51 | k and Eddy Viscosity Ratio, Turb. Kinetic Energy: 0.1 m^2 s^-2, Eddy Viscosity Ratio: 10 | Entrainment, Rel Pres 0 Pa, Zero Gradient | 6.06311 | 0.03645 | 1.281613 |

# LIST OF REFERENCES

[1]     Max F. Platzer and Nesrin Sarigul-Klijn, "A Novel Approach To Extract Power From Free-Flowing Water and High Altitude Jet Streams," in *Proceedings of ES2009 Energy Sustainability 2009*, San Francisco, 2009, p 2.

[2]     Max F. Platzer and Nesrin Sarigul-Klijn, "A New Oscillating-Foil Power Generator for Sailingship-Based Renewable Energy Generation," in *ASME Energy Sustainability*, 2010, p 3.

[3]     Max F. Platzer and Nesrin Sarigul-Klijn, "Renewable Hydrogen Production Using Sailing Ships," in *ASME International Mechanical Engineering Congress & Exposition*, , 2011, p 2.

[4]     Max F. Platzer and Matthew Lennie, Department Lecture: "The Energy Ship: A New Concept to Harness Ocean Wind Power," Naval Post Graduate School; Royal Institute of Technology, Monterey, CA, 2012.

[5]     M. J. Khan, G. Bhuyan, M. T. Iqbal, and J. E. Quaicoe, "Hydrokinetic Energy Conversion Systems and Assessment of Horizontal and Vertical Axis Turbines for River and Tidal Applications: A Technology Status Review," *Applied Energy*, vol. 86, pp. 1823-1835, April 2009.

[6]     Thomas Christian, "Tow Tank Software Integration and Programming for NPS Tow Tank," Naval Postgraduate School, Monterey, CA, Thesis Laboratory Setup Guide, 2012.

[7]     Mike Fusner, "Honeywell Certificate of Calibration for Model 41 Load Cell," Sensotec Sensors at Lebow Products, Calibration 060-0571-04-01 Serial No. 1309877, 2012.

[8]     Omni Instruments, "MiniWater6 Probe Anemometer Configuration Guide," Omni Instruments, United Kingdom, Product Information Sheet 2008.

[9]     Olympus Corporation.  Olympus Product Description. January 2013 [Online]. http://www.olympus-ims.com/en/ispeed-3/

[10]    The McGraw-Hill Companies. (2001) About the Author. [Online]. Available: http://www.mhhe.com/engcs/mech/white/biography.mhtml

[11]    Frank M. White, *Fluid Mechanics*, 7th ed., New York: McGraw-Hill Science/Engineering/Math, 2010.

[12]  Ampair Energy Ltd., *UW 100 Hydro Turbine Technical Manual*, Ampair Energy Ltd, 2009.

[13]  Clements Marine, *Prop Report*, Performance Check 14052012_12L_6_3 Blade, Clements Engineering Ltd, 2012.

[14]  Robert Sani, Sping Lecture Series: "Drag Force and Drag Coefficients," Sping Lecture Series, Fluid Mechanics at Colorado University, Boulder, Colo, 2007.

[15]  A. Filippone. (2004) Advanced Topics in Aerodynamics. [Online]. Available: http://web.archive.org/web/20070715171817/http://aerodyn.org/Drag/tables.html

[16]  R. G. D. Steel and J. H. Torrie, *Principles and Procedures of Statistics*, 1st ed., New York: McGraw-Hill, 1960.

[17]  John Ward Smith Bernard Stanford Massey, *Mechanics of Fluids*, 7th ed., Nelson Thornes, Ed. Cheltenham, United Kingdom: Stanley Thornes Ltd, 1998.

[18]  REUK. (2013, January) Renewable Enerby UK. [Online]. Available: http://www.reuk.co.uk/Wind-Turbine-Tip-Speed-Ratio.htm

[19]  Ansys 14.0 Help. (2012) Flow Around a Blunt Body Tutorial 7. Ansys 14.0. Program Tutorials Archive.

[20]  Xiao, Keith Walters Wang, "Computational Analysis of Marine-Propeller Performance Using Transitional-Sensitive Turbulence Modeling," *Journal of Fluids Engineering*, vol. 134, no. 7, July 2012."

[21]  International Towing Tank Conference, "Recommended Procedures, Testing and Extrapolation Methods," in *ITTC Revision 01*, 2001, p. 8.

[22]  Barnes R. McCormick, *Aerodynamics, Aeronautics, and Flight Mechanics*, 1st ed. New York: John Wiley & Sons, Inc, 1979.

[23]  FLUENT. (2013, January) Near Wall Treatments for Wall Bounded Turbulent Flows. ANSYS FLUENT 14.0 Theory Guide.

[24]  James O. Wilkes, *Fluid Mechanics for Chemical Engineers, Second Edition, with Microfluidics and CFD*, 2nd ed., Upper Saddle River, NJ: Prentice Hall, 1996.

[25]  "Wind Turbine Aerodynamics" in *Wikipedia*, [Online], 2013, January. Available: http://en.wikipedia.org/wiki/Wind_turbine_aerodynamics

# INITIAL DISTRIBUTION LIST

1.    Defense Technical Information Center
      Ft. Belvoir, Virginia

2.    Dudley Knox Library
      Naval Postgraduate School
      Monterey, California

3.    Young W. Kwon
      Naval Postgraduate School
      Monterey, California

4.    Maximilian F. Platzer
      Naval Postgraduate School
      Monterey, California

5.    Garth V. Hobson
      Naval Postgraduate School
      Monterey, California

6.    Thomas M. Ravens
      University of Alaska
      Anchorage, Alaska

7.    Jonathan W. Naughton
      University of Wyoming
      Laramie, Wyoming